

## Sp<sup>2</sup>-carbon dominant carbonaceous materials for energy conversion and storage



Debin Kong<sup>a</sup>, Zhichang Xiao<sup>a,b</sup>, Yang Gao<sup>a</sup>, Xinghao Zhang<sup>a</sup>, Ruiying Guo<sup>a</sup>, Xiaoxiong Huang<sup>a</sup>, Xianglong Li<sup>a,\*</sup>, Linjie Zhi<sup>a,\*</sup>

<sup>a</sup> CAS Key Laboratory of Nanosystem and Hierarchical Fabrication, CAS Center for Excellence in Nanoscience, National Center for Nanoscience and Technology, Beijing 100190, PR China

<sup>b</sup> College of Sciences, Agricultural University of Hebei, Baoding 071001, PR China

### ARTICLE INFO

**Keywords:**

Sp<sup>2</sup>-carbon dominant carbonaceous materials  
Bottom-up strategy  
Top-down strategy  
Energy storage and conversion

### ABSTRACT

Sp<sup>2</sup>-carbon (Sp<sup>2</sup>-C) based carbonaceous materials, featured by its inherent unit structural characteristics of chemical tunability, conjugated network, as well as the topological structure of the carbon-carbon double bond, have been considered as a dazzling star in both scientific research and industrial applications. Compared with defect-free Sp<sup>2</sup>-carbon bonded carbon materials, Sp<sup>2</sup>-C dominant carbonaceous materials with abundant functionalities and tunable pore structures are more attractive as a candidate for energy storage and conversion systems due to their synergistic effects of the conjugated Sp<sup>2</sup> carbon network and the introduced extra functions induced by defects, heteroatoms, many other structure characters, thereby resulting in the combination of the firm and flexible skeleton network, improved electron/ion transport, as well as the rich and exposed active sites. In this Review, we try to give a comprehensive overview of the latest development of Sp<sup>2</sup>-C dominant carbonaceous materials for energy conversion and storage. First, we provide a brief summary of the structural features of Sp<sup>2</sup>-C dominant carbonaceous materials. Second, the controllable synthesis of these Sp<sup>2</sup>-C dominant carbonaceous materials are extensively discussed according to two representative approaches: the “bottom-up” approach via monomer-controlled synthesis, biopolymer transformation, and chemical vapor deposition, and “top-down” approach involving the chemical exfoliation, electrochemical exfoliation and unzipping. Particularly, after a thorough discussion of their applications as electrode materials for energy storage and conversion applications, the mechanism and the targeted structure-property relationships of the Sp<sup>2</sup>-C dominant carbon materials for specific energy storage and conversion are highlighted. Finally, we draw conclusions on the rational construction and engineering of the Sp<sup>2</sup>-C dominant carbon materials for energy-related systems and their opportunities in the future.

### 1. Introduction

In consequence of growing concerns on the energy crisis and environmental degradation brought by fossil fuels, high efficiency conversion and storage devices (e.g., intermittent solar power energy, lithium-ion batteries (LIBs), supercapacitors) of new renewable energy are in spurred demand [1–10]. Although significant progress for energy conversion and storage devices has been made in the last few decades, the energy density, power density, the conversion efficiency and lifespan still hardly meet the requirements. As the advancement of these energy storage and conversion systems highly depends on the development of active materials used in respective electrodes, a bunch of porous inorganic and organic materials have been extensively

investigated [11–19]. However, the deployment of novel materials (e.g., high capacity materials for lithium-ion batteries, pseudocapacitive materials for supercapacitors, electrocatalysts for oxygen reduction reaction) still faces great challenges involving inferior dynamic behaviors against large charging current, poor stability under long-term cycling, the imbalance between selectivity and efficiency, and so on. In this context, it has been generally recognized that electrical conductivity, specific surface area (SSA), chemical functionalities and pore structures of these electrode materials systems are fundamentally important in governing the device performance.

Benefiting from the inherent characteristics of chemical tunability, conjugated network as well as the topological structure of carbon-carbon double bonds, sp<sup>2</sup>-carbon (sp<sup>2</sup>-C) based carbonaceous materials

\* Corresponding authors.

E-mail addresses: [lixl@nanoctr.cn](mailto:lixl@nanoctr.cn) (X. Li), [zhilj@nanoctr.cn](mailto:zhilj@nanoctr.cn) (L. Zhi).

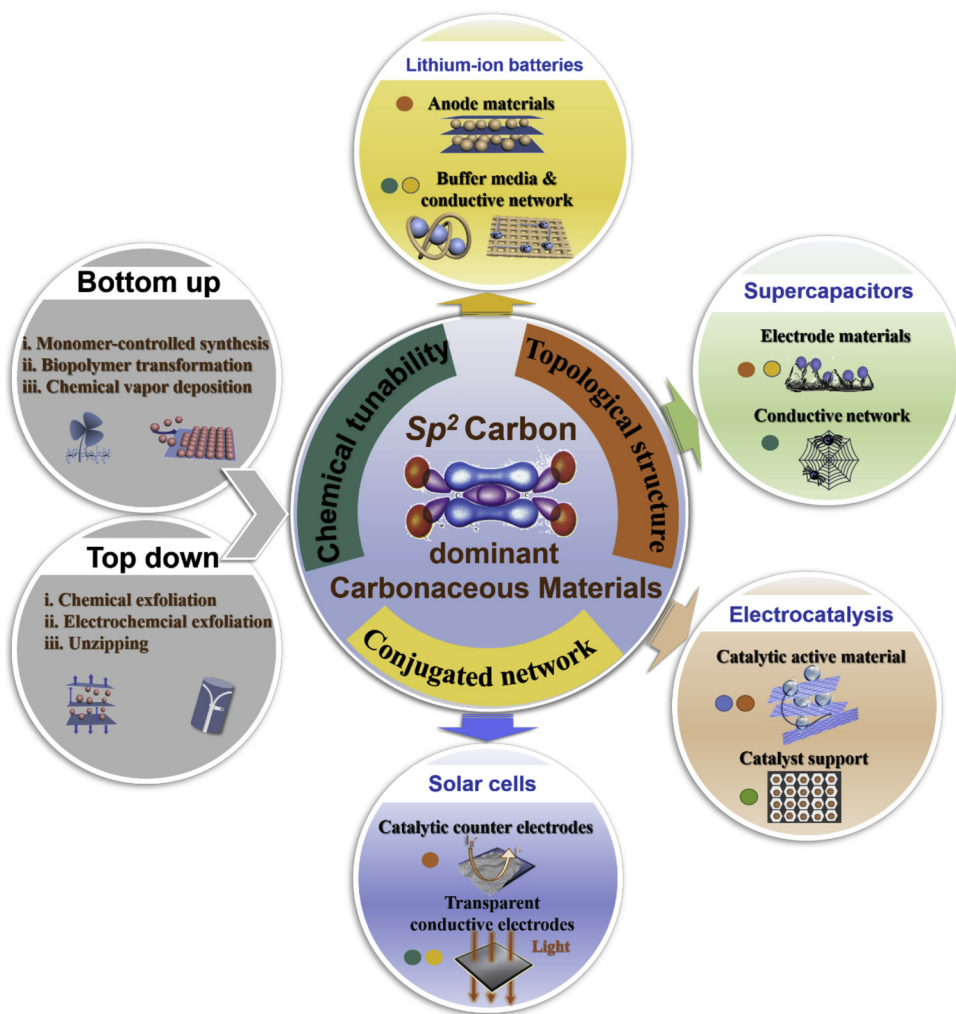


**Fig. 1.** Overview of  $sp^2$ -C dominant carbonaceous materials for energy conversion and energy storage.

have been considered as a dazzling star for energy storage and conversion applications (Fig. 1) [20–24]. Particularly, as electrode materials, material hosts or electrocatalysts, carbonaceous materials with tunable active sites, superior conductivity, high surface area, and/or abundant porosity offer either rich electrochemical active sites, or superior conductive network, or large electrolyte-electrode contact area for fast diffusion and reaction, or some of them [25–29]. In addition, the intrinsic characteristics of outstanding chemical stability and mechanical strength render hybrids to accommodate the pronounced volume variation accompanied with repeated charging/discharging processes [30,31]. Interestingly, compared with graphene and carbon nanotube, which represent defect-free and functionality-free  $sp^2$ -bonded carbon atoms,  $sp^2$ -C dominant carbonaceous structures with rational introduction of functional groups are endowed with new functionalities, being of great significance for many current and emerging technologies. For instance, heteroatom doped or chemically functionalized carbon materials recently show great potential as electrodes in pseudocapacitive energy storage [32]. Meanwhile, the integration of carbonaceous materials with secondary subunits with high-energy facets confers enhanced electrocatalytic activity due to synergistic effects of different components [33]. These distinct features of  $sp^2$ -C dominant carbonaceous materials has therefore stimulated extensive investigations on their energy-related applications. In this regard, this review is not intended to illustrate defect-free  $sp^2$ -bonded carbon materials, but rather, it focuses on fundamental principles and emerging strategies of  $sp^2$ -C dominant carbonaceous materials for various energy storage and conversion applications, which hold the

greatest potential for a major impact in addressing the challenges of energy related technologies.

In this review, we give a comprehensive overview of the latest advances of  $sp^2$ -C dominant carbonaceous materials for energy conversion and storage. First, the controllable synthesis of these  $sp^2$ -C dominant carbonaceous materials will be extensively discussed according to two representative approaches as shown in Fig. 1. Specifically, the strategy shown at the top obtains the  $sp^2$ -C dominant carbonaceous materials through a 'top-down' approach involving the chemical exfoliation, electrochemical exfoliation and unzipping whilst the strategy at the bottom presents a 'bottom-up' epitaxial growth method via monomer-controlled synthesis, biopolymer transformation, and chemical vapor deposition (CVD). After that, their applications as electrode materials for LIBs and hybrid supercapacitors (HSCs), solar cells, and electrocatalysts for oxygen- and hydrogen-involving energy conversion reactions are discussed thoroughly, highlighting the mechanisms and the targeted structure-property relationships of the  $sp^2$ -C dominant carbon structure materials in respective energy storage and conversion reaction systems. Finally, we provide conclusions on the rational construction and engineering of the  $sp^2$ -C dominant carbon materials for energy-related systems and their opportunities in the future.

## 2. Synthesis of $sp^2$ -C dominant carbon materials

### 2.1. Bottom up strategy

The bottom-up synthesis approaches, based on monomer-controlled

synthesis, biopolymer transformation and chemical vapor deposition are considered to be an ideal and indispensable tool to create structurally well-defined  $sp^2$ -C dominant carbon materials. On the one hand, those  $sp^2$ -C dominant carbon material precursors are built up from small molecules, and thus their intrinsic structures can be adjusted within the capabilities of solution-mediated synthetic chemistry. On the other hand, chemical tunability, topological structure and conjugated network on the molecular level can be easily established during the fabrication process, including introducing heteroatoms, engineering pore structures and designing new synthesis formula on functionalized precursors, which grants the products delicate and desirable functions.

### 2.1.1. Monomer-controlled synthesis

The monomer-controlled bottom-up synthesis approach is considered to be an efficient methodology to produce structure well-defined  $sp^2$ -C dominant carbon materials. Particularly, polycyclic aromatic hydrocarbons (PAHs) are considered as typical building blocks for these objects, concerning the resultant structure can be predictable and large-scale production is possible [34–36].

Generally speaking, two chemical monomer-controlled bottom-up strategy can be adapted to synthesize  $sp^2$ -C dominant carbon materials. One is through a controllable chemical reaction under mild conditions in solution. To fabricate carbon materials dominant by  $sp^2$ -C, a precursor containing all-benzene subunits would be a desirable choice. In this context, dendritic polyphenylenes (DPPs), as a typical reservoir of benzene rings, are occupied with mono-dispersed dendrimers and poly-dispersed hyperbranched polyphenylenes, which are believed to be ideal candidates as precursors for  $sp^2$ -C dominant carbon materials. Two methods are available to access such kind of mono-dispersed DPPs. Firstly, through the cyclotrimerization of diphenylacetylenes, a dendritic all-benzene molecule, namely, hexaphenylbenzenes can be obtained [37]. In this way, not only can other functional groups such as thiophene be introduced into the dendritic structure, but also large DPPs of a higher generation can be achieved [38]. As an alternative, highly versatile Diels-Alder cycloaddition of phenyl-substituted alkynes could also be adopted to prepare DPPs with tetraphenyl-substituted cyclopentadienones (CPs) [39]. Notably, different CPs and alkyne derivatives can be integrated through this reaction, leading to a variety of substitution types and molecular topologies. In addition, DPPs with versatile geometries and large sizes can be achieved by employing different alkyne structures as building blocks (Fig. 2a) [40]. Surprisingly, repetitive Diels-Alder reactions of CPs with an alkyne core can grow the DPPs to third, fourth, fifth, and higher generations with a molecular weight of even up to 271 000 g mol<sup>-1</sup>.

Poly-dispersed hyperbranched polyphenylenes are promising to grow even larger  $sp^2$ -C dominant carbon materials by utilizing AB<sub>2</sub> functionalized building blocks. For example, Kim et al. reported a kind of metal-catalyzed intramolecular coupling of 3,5-dibromophenyl-bionic acid or 3,5-dihalophenyl Grignard reagents. Afterwards, the Diels-Alder cycloaddition of a CP and a di-alkyne compound is demonstrated to be a more favorable alternative approach. The AB<sub>2</sub> functionalized CP is one of the interesting building blocks containing cyclopentadienone and alkyne dienophile units. This precursor can easily undergo intra-molecular Diels-Alder cycloaddition to form hyperbranched polyphenylene [41] with highly condensed phenyl rings and unlimited extension of  $sp^2$ -C dominant structure.

DPPs with all-benzene unit are rigid 3D molecules. By effective oxidative cyclodehydrogenation reaction, the phenyl rings can be fused into 2D  $sp^2$ -C dominant structure. During this process, predissolved iron (III) chloride in nitromethane is used as both Lewis acid and oxidizing reagent. As a typical example, hexabenzocoronene (HBC), a molecular graphene, can be obtained in high yield by dehydrogenation of hexaphenylbenzene (Fig. 2b) [42,43].

Furthermore, mono-dispersed molecular  $sp^2$ -C dominant carbon materials of various geometries and sizes can be synthesized through cyclodehydrogenation reactions (Fig. 2c) [44,45], in which the

corresponding DPPs are chosen as starting compounds. The insoluble product was characterized by isotope-resolved matrix-assisted laser desorption ionization time-of-flight (MALDI-t OF) mass spectroscopy as well as solid-state NMR spectroscopy.

Bi et al. synthesized a series of conjugated porous polymers with substantial cyano-substituted fully  $sp^2$ -carbon frameworks by using electron-deficient tricyanomethylene as a key building block to promote an organic base-catalyzed Knoevenagel condensation with various aldehyde-substituted arenes (Fig. 2d) [46]. The resulting  $sp^2$ -C dominant materials feature donor-acceptor structures with  $\pi$ -extended conjugation, rendering them with distinct semiconducting properties. Such  $sp^2$ -C dominant materials possess hierarchically porous structures, nanoscale morphologies, and intriguing wettability. These promising physical characters, finely tailororable by varying the arene units, are essentially relevant to the abundant cyano substituents over the whole frameworks.

Graphene nanoribbons (GNRs) as one kind of  $sp^2$ -carbon material, are attracting more and more attention for their potential in next-generation semiconductor field [47–49]. However, the traditional ‘top-down’ methods, such as the lithographical patterning of graphene [50] and the unzipping of carbon nanotubes [51], always result in mixtures of different GNRs. In contrast, the ‘bottom-up’ chemical synthetic approach based on solution-mediated or surface-assisted cyclodehydrogenation represents a promising strategy for fabricating GNRs with precise structure [52–54]. Consequently, Akimitsu et al. developed an efficient bottom-up solution synthesis of longitudinally well-extended (200 nm) GNRs (Fig. 3) with excellent liquid-phase processability based on the cyclodehydrogenation of semirigid polyphenylene precursors of high molecular weight [55]. Scanning probe microscopy (SPM) analysis of GNRs demonstrates an exquisitely ordered self-assembled monolayer of GNRs, which further corroborates their well-defined structure.

Besides the controllable chemical reaction under mild conditions in solution such as the above-discussed cyclodehydrogenation, a more efficient strategy for integrating graphene subunits into  $sp^2$ -C dominant carbon materials is to combine bottom-up synthesis processes and thermolysis. Although the mass distribution of the products is not homogeneous, the second protocol is extremely versatile for growing desirable  $sp^2$ -C dominant carbon materials with large ratio of graphene fragments. For example, Zhi et al. constructed one dimensional (1D) fibers and tubes through the oriented carbon-carbon cross-linking reactions towards rigid conjugated polymer networks (Fig. 4a–c) [56]. During the fabrication process, molecules 1 and 2 with different substitution positions of functional iodo groups were used as the polymerization directing monomers, and 3 and 4 as cross-linkers in the synthesis of four different conjugated polymers (CPN1–CPN4). Furthermore, 1D carbon nanofibers and nanotubes (Py-CPNs) were synthesized in a template-free manner after carbonization. Microporous CNTs and CNFs with a surface area up to 900 m<sup>2</sup> g<sup>-1</sup> were obtained, together with high-resolution transmission electron microscopy (HR-TEM) characterizations indicating the formation of intrinsic microporous structure in these rigid carbon-rich networks. Based on a template-assisted thermolysis process, 1D  $sp^2$ -C dominant carbon materials can also be synthesized with other precursors (Fig. 4d and e) [57,58]. Via Diels-Alder cycloaddition of tetraphenyl cyclopentadienone (CPD) monomers, alkyl-substituted hyperbranched polyphenylene was synthesized, which was further thermolysed in nanoscale channels of AAO membranes, resulting in 1D mesoporous nanocarbons (MPNCs).

2D porous  $sp^2$ -C dominant carbon materials, for example, nanoporous graphene (NPG) has attracted great attention owing to its advantage in field-effect transistors (FET) and selective nanosieve for sequencing, ion transport, gas separation, and water purification. However, the nanopores can not be precisely controlled and the pore size is too large via top-down method at this stage. Meanwhile, the obtained graphene

exhibits no semiconductive properties. Surprisingly, César Moreno et al. reported a bottom-up method to synthesize nanoporous graphene

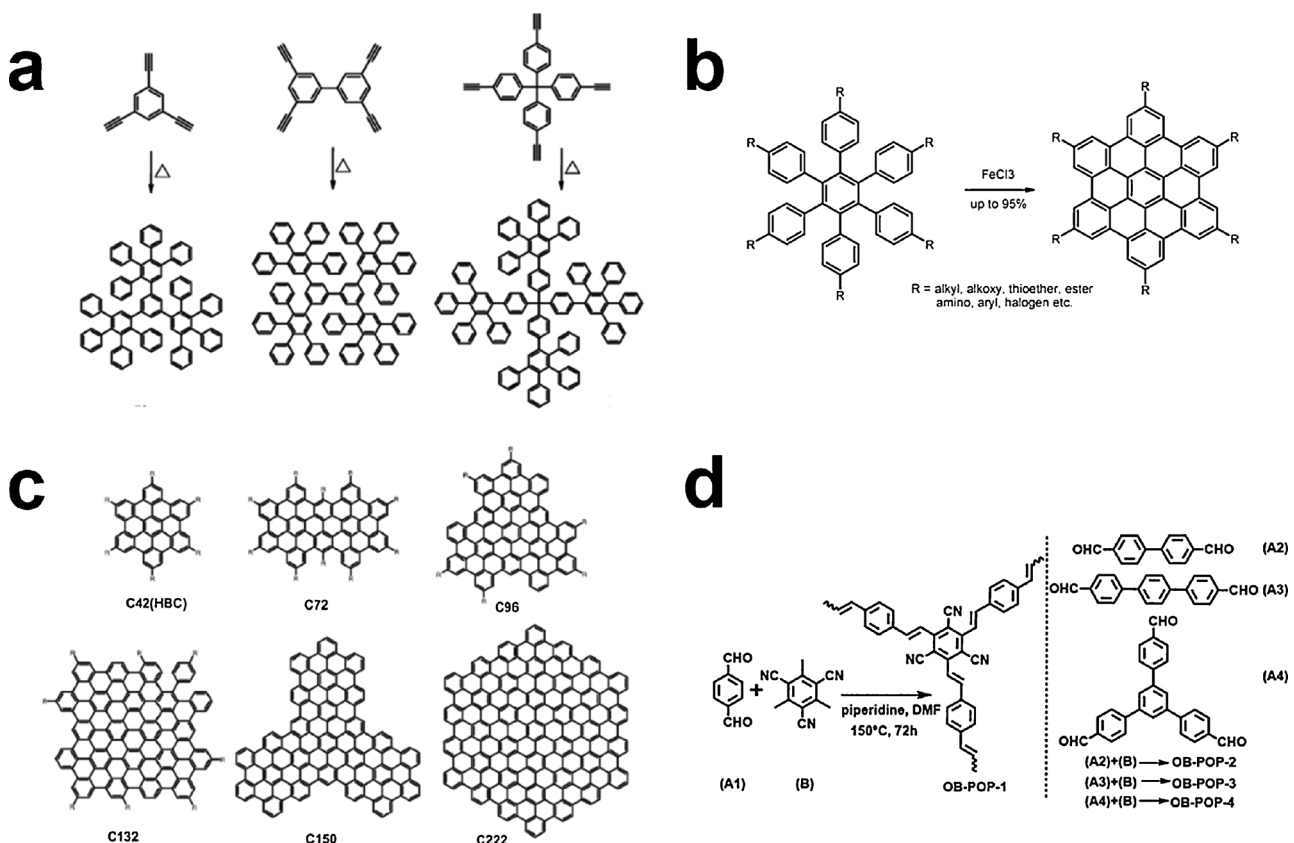


**Fig. 2.** (a) Various DPPs those are prepared from different alkynes via Diels-Alder cycloaddition. Reproduced from [40] Copyright 2004, Wiley-VCH. (b) Cyclo-dehydrogenation of DPPs towards molecular graphenes. Reproduced from [42] Copyright 2000, Royal Society of Chemistry. (c) Tool box of mono-dispersed molecular graphene prepared from cyclodehydrogenation of DPPs. Reproduced from [45] Copyright 2002, Wiley-VCH. (d) Synthetic process of olefin-bridged porous organic polymers (OB-POPs). Reproduced from [46] Copyright 2017, Wiley-VCH.

comprising an ordered array of pores separated by ribbons, which could be tuned down to the 1-nanometer range [59]. In this work, DP-DBBA (diphenyl-10,10'-dibromo-9,9'-bianthracene) was utilized as the building block, which undergoes Au surface-assisted Ullmann coupling into polymeric chains (step T1). The resulting polymeric chains exhibited the characteristic protrusion pairs with aperiodicity of 0.84 nm and an apparent height of 0.31 nm, which arises from probing the high ends of the staggered bis-anthracene units of the monomer with scanning tunneling microscopy (STM) (Fig. 5a and d). Annealing to  $T = 400\text{ }^{\circ}\text{C}$  triggers the intramolecular cyclodehydrogenation (step T2), giving rise to the aromatization of the chain and the corresponding reduction of the apparent height to 0.18 nm, which is characteristic of graphene nanoribbons (GNRs) (Fig. 5 b and e). The final step (T3) interconnects GNRs laterally in a reproducible manner by means of a highly selective dehydrogenative cross-coupling by further annealing to  $T = 450\text{ }^{\circ}\text{C}$

(Fig. 5c and f). The pore size of the NPG can be controlled at about 1 nm, and the pore size and shape can be adjusted on molecular level.

In-situ chemical functionalization is a popular way to construct novel  $\text{sp}^2\text{-C}$  dominant carbon materials towards advanced electrode materials and systems. For example, our group recently pioneered the great potential of triazine monomer-derived nitrogen-rich networks [60] a kind of porous polymer networks (PPNs), by using a modified polymerization protocol at higher temperatures which significantly improved the electrical conductivity of such networks (Fig. 6a). The covalent triazine-based framework-1 (CTF-1) could be synthesized usually under  $400\text{ }^{\circ}\text{C}$ , yet with poor electrical conductivity. In contrast, higher synthesis temperature leads to the formation of a new class of porous, conductive and nitrogen-rich networks (namely, thermalized triazine-based networks, TNNs). The synthesized TNNs comprise a large quantity of  $\text{sp}^2\text{-C}$  subunits that were interconnected by the remnant

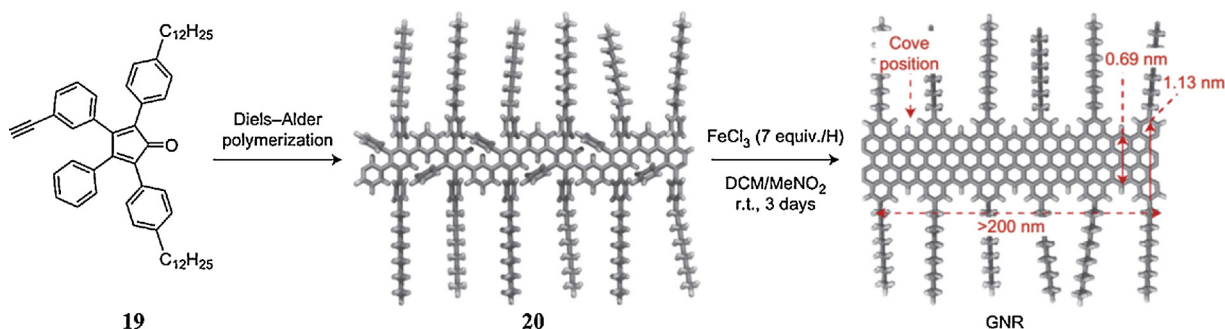


**Fig. 3.** Schematic synthetic route to longitudinally extended GNR via AB-type Diels-Alder polymerization of monomer 19. Precursor 20 was graphitized into GNR by intramolecular oxidative cyclodehydrogenation. Reproduced from [55] Copyright 2014, Nature Publishing Group.

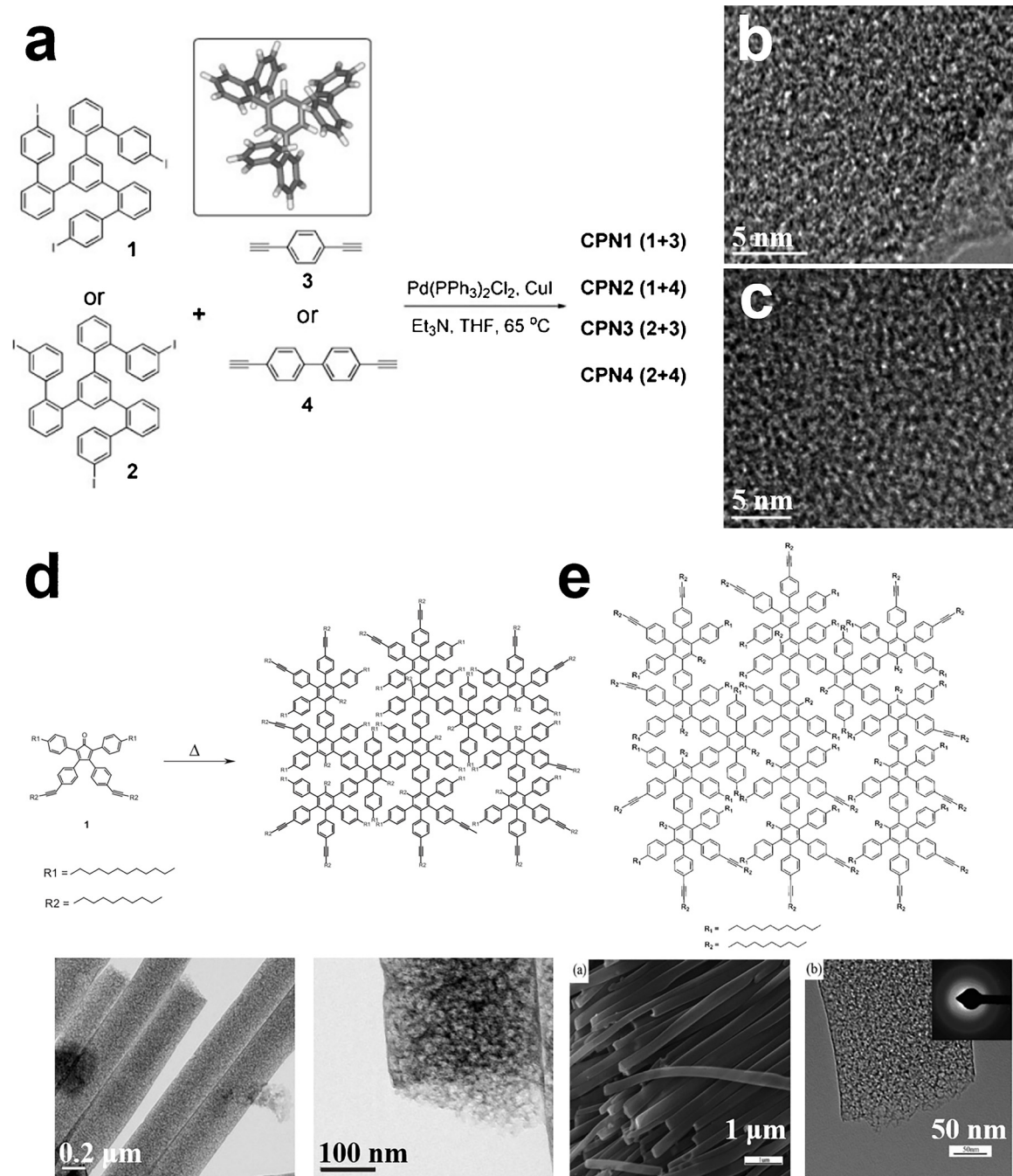


**Fig. 4.** (a) Synthesis of cross-linked conjugated polymers CPN1–CPN4. Inset shows the 3D view on the structure of 1,3,5-tri-2'-biphenylbenzene unit. HR-TEM images of (b) CPN1 and (c) CPN2. Reproduced from [56] Copyright 2009, Wiley-VCH. (d) Molecular structure of CPD monomers and the hyperbranched polyphenylenes, as well as TEM images of the hyperbranched polyphenylenes after stepwise heat treatment. Reproduced from [57] Copyright 2005, Wiley-VCH. (e) The precursor structure, scanning electron microscopy (SEM) and TEM images of MPNCs. Reproduced from [58] Copyright 2009, Royal Society of Chemistry.

polymeric and even conjugated organic fractions in a random manner (Fig. 6b). In addition, the scanning transmission electron microscopy image showed the homogeneous distribution of nitrogen in the skeleton of the TNNs, indicating the preservation of nitrogen functionalities in the network. This is further confirmed by the X-ray photoemission spectroscopy (XPS) analyses which show the presence of four distinct nitrogen configurations in the skeletons of the TNNs (Fig. 6c). What's more, the modulation of the bottom-up synthetic protocol for PPNs as exemplified provides an efficient way to produce functional  $sp^2$ -C dominant carbon materials for energy storage, specifically by tuning the electrical conductivity of such networks while preserving most of the chemical structures and functionalities of PPNs at the same time.

Benzene, as a typical  $sp^2$ -carbon molecule, can be knitted into porous organic polymers under mild conditions through knitting based bottom-up method. Such kind of polymers can be easily transformed into  $sp^2$ -carbon dominant carbon materials after delicate thermolysis process. Recently, a kind of benzene-based porous carbon material with tunable pore structure and morphology was successfully built up through this methodology (Fig. 6d) [61]. This  $sp^2$ -carbon dominant carbon material features abundant porosity and remarkably high-efficiency restrain for the pore collapse after the pyrolysis process, namely, a specific surface area retention (SSRA) high up to 45% in the absence of pore forming agent.

Keep the controllable bottom-up fabrication strategy in mind, a

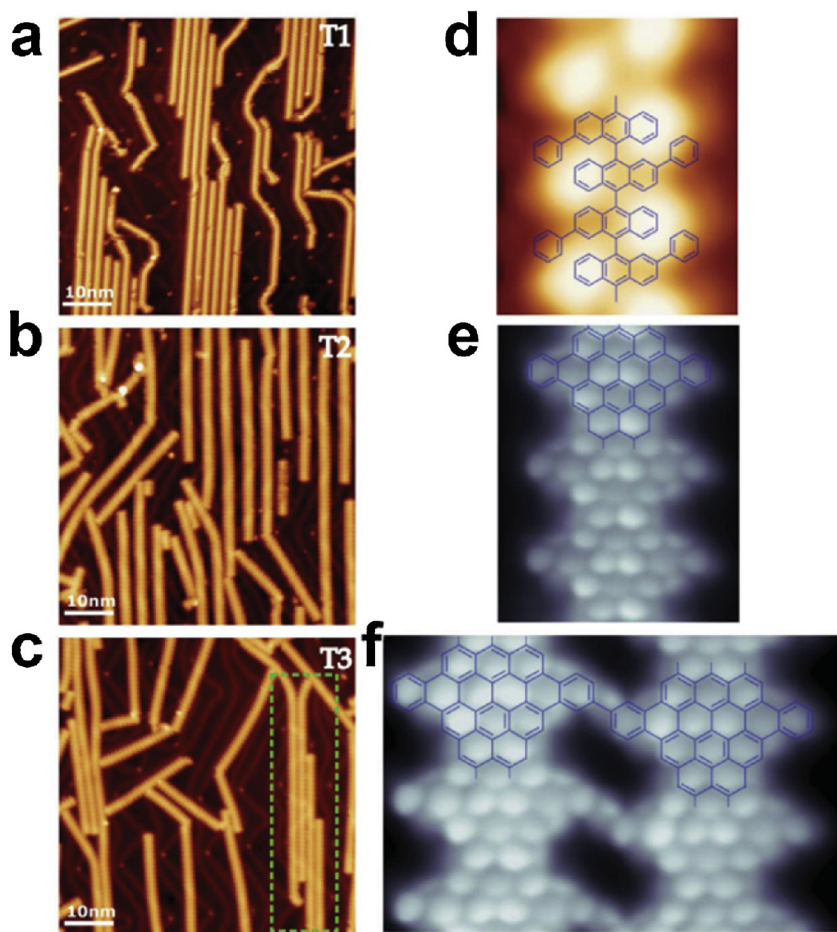


**Fig. 5.** Hierarchical synthesis of NPG. (a to c) Constant-current STM images showing the distribution and morphology of the different covalent structures obtained for a low coverage of precursors after each thermal annealing step T1, T2, and T3. At this coverage, NPG stripes form locally indicated with a green rectangle in (c). (d to f) Magnified images revealing the internal structure for each case, (a) to (c). Reproduced from [59] Copyright 2018, American Association for the Advancement of Science (For interpretation of the references to colour in this figure legend, the reader is referred to the web version of this article).

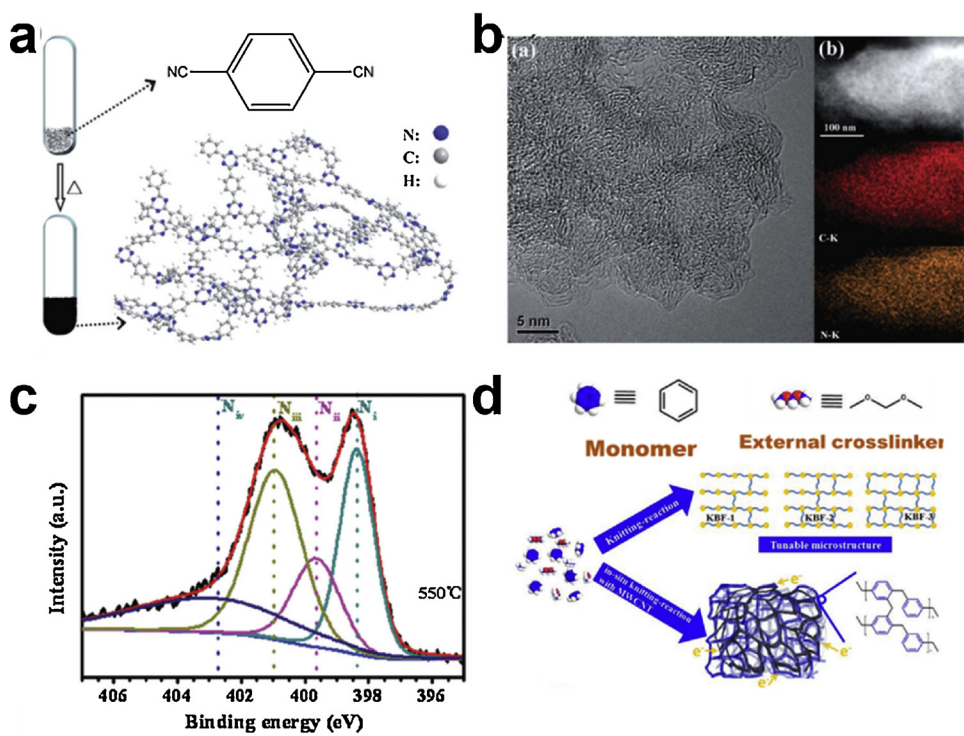


**Fig. 6.** (a) Illustration of the synthesis procedure of TNNs. (b) TEM and STEM images of TNNs. (c) Typical N1s XPS spectrum of TNNs. Reproduced from [60] Copyright 2015, American Chemical Society. (d) Schematic illustration of the fabrication of KBF-x and MWCNT@KBF-3. Reproduced from [61] Copyright 2017, Elsevier.

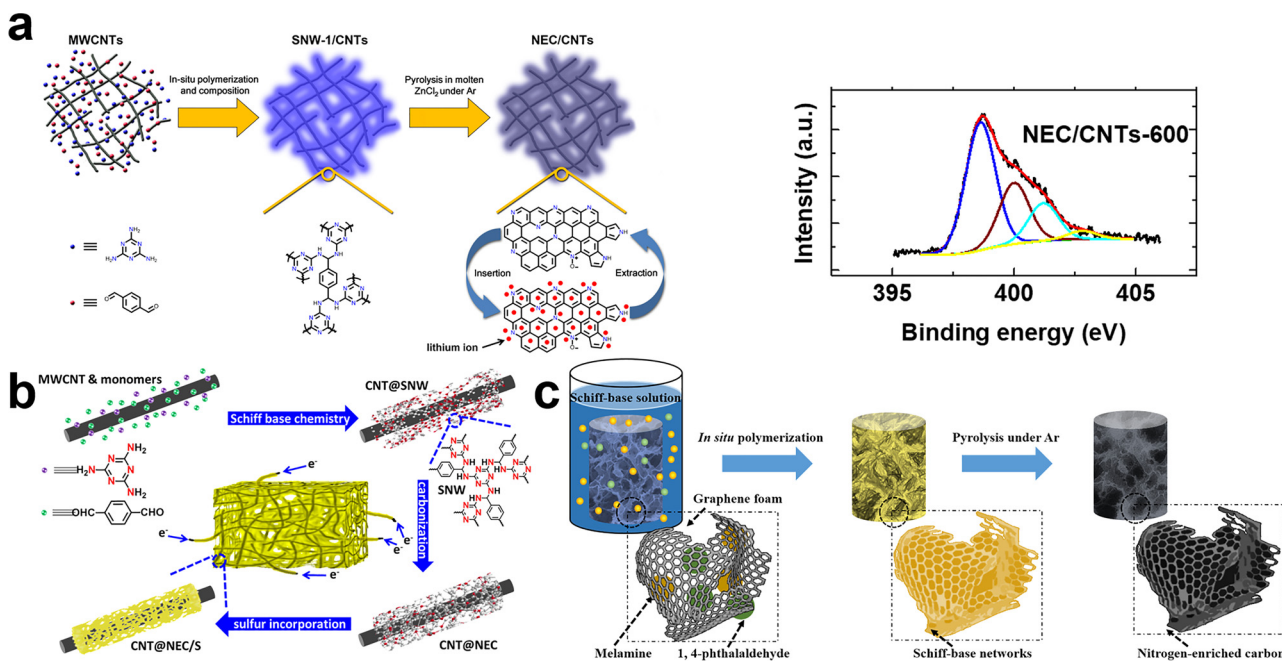


**Fig. 7.** Schematic illustration of (a) the synthesis procedure of NEC/CNTs. Reproduced from [62] Copyright 2018, Wiley-VCH. (b) the fabrication procedure of CNT@NEC/S composite by: (i) fabricating an interwoven coaxial cable network (CNT@SNW) through a Schiff-base chemical reaction; (ii) a controllable thermalized process yields nitrogen-enriched (CNT@NEC) coaxial nanocable carbon network; (iii) the incorporation of sulfur into the carbon network through a melting method. Reproduced from [63] Copyright 2018, Elsevier. (c) The synthesis of NEC/Gf and different architectures of SNW/Gf. Reproduced from [64] Copyright 2018, Royal Society of Chemistry.

novel nitrogen-doped sp<sup>2</sup>-carbon material (NEC/CNT) through a chemically induced precursor-controlled pyrolysis approach is successfully achieved (Fig. 7a) [62]. Instead of conventional N-containing sources or precursors, Schiff-base network (SNW-1) enables the desirable combination of a 3D polymer with intrinsic microporosity and ultrahigh N-content, which can significantly promote the fast transport of both Li<sup>+</sup> and electron. Remarkably, the strong interaction between carbon skeleton and nitrogen atoms enables the retention of ultrahigh N-content up to 21 wt% in the resultant NEC/CNT. On the basis of this fabrication technique, an interwoven coaxial cable sp<sup>2</sup>-C dominant carbon materials with ultrahigh nitrogen content of 9.56 wt% is successfully fabricated through engineering a rationally designed Schiff-base Chemistry. (Fig. 7b) [63]. This in-situ bottom-up strategy enables the targeted heteroatom doping throughout the entire networks on molecular scale. Thus, a homogenous interface between nitrogen and carbon matrix can be achieved even at such a high doping level, which is demonstrated to play the key role in facilitating the chemical absorption of sulfur.

Furthermore, an efficient contact-induced mode, that is, the in-situ concentrated-solution induced polymerization strategy [64], is successfully developed to integrate the Schiff-base polymer into sheet-like structure, resulting in POPs/graphene foam with arbitrary architectures on a large-scale (Fig. 7c). This exquisite design process not only allows the tunable shape and moldable properties, but also maintains the intrinsic chemical structure characteristics of POPs. Typically, the nitrogen-rich Schiff-base networks are employed as the POPs to prepare the Schiff-base networks/ graphene foam (SNW/Gf), demonstrating the impressive nitrogen content up to 37 at%. Interestingly, the yielding composite still holds 9.6 at% nitrogen content accompanied with abundant porosity even after thermal treatment at 500 °C with sp<sup>2</sup>-carbon dominant structure. The highly effective and homogeneous interface endows the NEC/Gf composites with superior lithium storage performance to the physical mixture of nitrogen-enriched carbon/graphene powder (NEC/Gp).

#### 2.1.2. Biopolymer transformation

Low cost biomass, as potential precursors to construct sp<sup>2</sup>-C

dominant carbonaceous materials, possesses diverse microstructures, which the resulting carbonaceous materials can inherit through carbonization. For the biomass derived sp<sup>2</sup>-C dominant carbonaceous materials (with a sp<sup>2</sup>-C content of more than 50%, depending on the detailed modalities), such structural criterion always confers the material with tunable active sites, superior conductivity, high surface area, and/or abundant porosity providing either rich electrochemical active sites, or superior conductive network, or large electrolyte-electrode contact area for fast diffusion and reaction. A class of biomass, including eggshell membranes [65], seaweeds [66], raw blood protein [67], amaranthus waste [68], silk [69], etc [70–76] have been investigated. Notably, most of the yielding carbonaceous materials possess high SSA and exhibit excellent electrochemical performance, although they have distinct morphologies. As the inherent structure of the biomass precursors plays important role in the microstructure and porosity of carbonized products, the morphological and pore structure of the biomass derived carbonaceous materials can be well designed through intentionally selecting the precursor [77]. This biomass-carbonization strategy is also much easier compared with above-mentioned complicated synthesis procedure and no chemical agent is required.

Eggplant is a sheet like structure on microscale. Upon freeze drying followed by one-step carbonization, it was demonstrated that the sheet-like porous carbon (namely, SPC) can be obtained [78]. Carbonization of eggplant converts the thick corrugated layers of the eggplants into loose carbon sheets with thickness ranging from 100 to 200 nm. The TEM image reveals interlinked pore structure with average size of 40–60 nm on the carbon lamellar, which the short ion diffusion paths is critical for high rate performance. The effect of temperature on the microstructure is further investigated. With the increase of temperature, the (002) peaks of X-ray diffraction patterns indicate higher graphitic degree and the graphite layer fringes turn clearer and longer. Additionally, the SSA of the carbon sheets raises from 606 to 627 and 950 m<sup>2</sup> g<sup>-1</sup> on elevating the carbonization temperature from 700 to 900 and 1000 °C. However, the SSA drops dramatically to 133 m<sup>2</sup> g<sup>-1</sup> while further increasing temperature to 1100 °C. Interestingly, the high

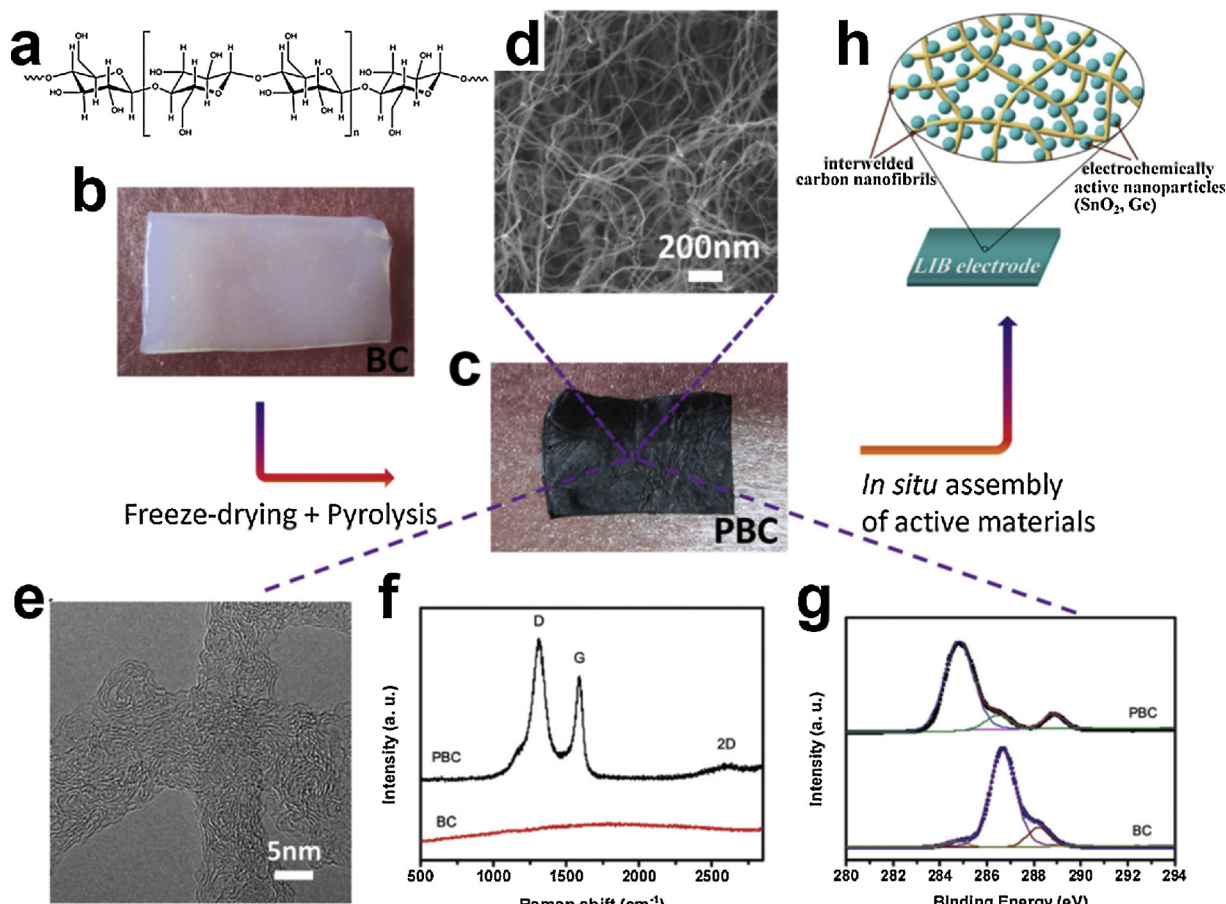


**Fig. 8.** The synthesis process of PBC and its hybrids, accompanying HRTEM image of PBC, Raman spectra of PBC and BC, and C1s XPS profiles. Reproduced from [80]. Copyright 2013, Wiley-VCH.

protein content in the original eggplant contribute to N-doped carbon with 0.88 at%.

Alternatively, by employment of the pyrolysis treatment of the nanofibrillated biopolymer bacterial cellulose (BC), Liang et al. reported the preparation of the resultant BC (denoted as PBC), consisting of interconnected 1D nanofibers, showing outstanding conductivity and mechanical properties [79]. The partial graphenization of the BC is suggested to bear responsibility for the observed properties. Such a structural transformation was recently in detail studied by our group, as shown in Fig. 8 [80]. As revealed in the HRTEM image, the PBC nanofiber are mainly composed of randomly orientated graphenic sheets, most of which seem to be linked by amorphous junctions. Raman spectra further verified the presence of graphenic sheets in the PBC nanofibers. There are two typical peaks at 1590 and 2640  $\text{cm}^{-1}$ , corresponding to G band and 2D band, respectively, which are signatures of graphene-like materials while no obvious peaks are observed in the spectrum of BC. Moreover, the relatively prominent disordered band (D band) indicates the existence of defects and significantly disordered structure of graphenic sheets, accompanied with the amorphous carbonaceous fractions involved in the PBC nanofibers. The chemical bonding structure of PBC was further disclosed via the high-resolution XPS C1s spectra of BC and PBC, as shown in Fig. 8. The C1s deconvolution spectra of BC yielded three typical peaks: a main peak at 286.6 eV assignable to carbon in the C–O moiety, and two shoulder peaks at ca. 284.7 and 288.3 eV attributed to  $\text{sp}^3$  C/C–H and O–C–O moieties of BC, respectively. In comparison, one dominant peak at ca. 284.7 eV is observed for PBC, corresponding to  $\text{sp}^2$  C in the PBC nanofibers, which further proves the presence of graphitic sheets as indicated by TEM and Raman results. Additionally, two relatively weak

peaks at 286.6 and 289 eV can be attributed to the carbon atoms in C–O and O–C=O moieties, respectively, suggesting the presence of a small portion of oxygen-containing functional groups in the resultant PBC nanofibers.

In addition to dimension control, the microstructure and porosity of the pyrolyzed carbonaceous materials can be regulated by differentiating biomass organs with different physiologic functions. Very recently, using lotus as precursor, Zhang et al. emphasized the importance of physiologic function of plant in the porosity and microstructure of yielding carbonaceous materials [67]. By means of thermogravimetric analysis (TGA) and  $\text{N}_2$  adsorption-desorption isotherms analysis, the evolution of pore in the biomass carbon is clarified. The pore generation can be largely attributed to the process of carbonaceous matter densification and leaving of loose-bonded carbon atoms and heteroatoms rather than biomass decomposition. More importantly, in comparison with lotus stems and leaves that intrinsically possess different amounts of embedded salts, and intentionally remove these salts in the organs before their carbonization, the high porogen efficiency of the embedded salts at relatively low contents are explained. It is also demonstrated that the organ-dependent porosity in biomass carbon can be extended to other plants with wide disparity in the stems and leaves, including celery and asparagus lettuce. Accordingly, optimizing the biomass pyrolyzing condition, the SSA of prepared carbon products can reach as high as  $2200 \text{ m}^2 \text{ g}^{-1}$ .

#### 2.1.3. Chemical vapor deposition (CVD)

CVD method is another typical approach towards versatile  $\text{sp}^2$  carbon materials including graphene and carbon nanotubes [81–83]. The chemical composition and physical state of catalytic substrates

often play a very important role [84–88]. By influencing the basic elements such as adsorption, decomposition, diffusion, surface reaction, nucleation and growth, the procedure parameters determine the pyrolysis efficiency of the precursor, the deposition rate of the material and the quality of the final product [89,90]. Traditionally, two-dimensional materials or single crystals are fabricated on rigid solid substrates [91,92]. Li et al. demonstrated that growth of graphene on copper substrate occurs predominantly by surface nucleation followed by a two-dimensional growth process [93]. Optimizing the growth condition, specifically, methane flow rates of  $1.3 \text{ ml min}^{-1}$  and the hydrogen flow rate at  $2 \text{ ml min}^{-1}$ , large size graphene at millimeter scale was successfully prepared, as verified by SEM image. Additionally, the domains tended to possess high “edge roughness”. The shape of the graphene nuclei in the initial stages of growth exhibited a hexagonal symmetry, which eventually developed to large graphene domains with growing edges resembling dendrites.

Wang et al., for the first time, reported high quality homogeneous single layer graphene on liquid metal gallium (Ga) [94]. The low vapor pressure on the Ga surface enables the surface of the liquid Ga smooth, which is beneficial to the reduction of the nucleation density of graphene and the growth of high quality graphene. The nucleation density of graphene on liquid Ga surface is as low as  $1/1000 \mu\text{m}^{-2}$ , which is  $1/10$  of solid state Ga. The results demonstrate that graphene is very uniform on the surface of liquid Ga, and the migration rate of single crystal can reach  $7400 \text{ cm}^2 \text{ V}^{-1} \text{s}^{-1}$ . In addition to Ga, Fu et al. also systematically studied the growth behavior of other molten metal (liquid Cu [95], liquid In [96]) surface graphene, and obtained a strictly monolayer of graphene thin film. The results show that a homogeneous single graphene with 100% coverage on the surface of liquid metal can be obtained on the surface of the liquid metal when the carbon source, the growth time, the growth temperature and the cooling rate have been greatly changed. This indicates that when liquid metal is used to grow graphene, it has strong fault tolerance for growth parameter changes. This unique self-limiting growth behavior was analyzed and illustrated with Cu as an example.

Three dimensional (3D) continuous  $\text{sp}^2$  carbon network is highly desirable and possess huge potential in energy related applications [97]. Chen et al. for the first time reported the direct synthesis of 3D foam-like graphene foams via template-directed CVD method, which consisted of an interconnected graphene flexible network [98]. Very recently, Wei group adopted a mesoporous metal oxide that derived from the calcination of layered double hydroxide nanoflakes as the CVD template, resulting in the controllable 3D nanostructure and conductive scaffolds, as well as robust frameworks formed by  $\text{sp}^2$  carbon-carbon bonding [99].

On the contrary, our group has recently focused on the defect or imperfection-involved  $\text{sp}^2$ -C dominant carbonaceous materials via CVD technology [100,101]. For instance, such  $\text{sp}^2$ -C dominant carbonaceous sheaths (e.g., overlapped graphene sheaths, namely, G) were grown on the silicon nanowires at a relatively high temperature (typically,  $1050^\circ\text{C}$ ) under argon/hydrogen ( $\text{Ar}/\text{H}_2 = 2:1$ ) atmosphere via using methane ( $\text{CH}_4$ ) as the carbon source. The HRTEM images of the resultant SiNW@G nanocables samples in Fig. 9 reveal that the introduced G sheaths are mainly comprised irregularly void vesicle-like graphene sheets and overlapped graphene sheets. While these introduced graphene sheets bear different modalities and undulating features, it is also demonstrated that turbostatic carbon exists sparsely between these graphene sheets, corporately forming the observed G sheath. Notably, such G sheaths could act as adaptable but sealed sheaths to synergistically accommodate the volume change during cycling.

## 2.2. Top-down strategy

$\text{Sp}^2$ -C dominant carbonaceous material with functional groups can also be fabricated through top-down strategy [82,102–113]. Typically,

as one of the important  $\text{sp}^2$ -C dominant carbonaceous material, graphene oxide featured by rich oxygen containing functional groups and unique physical properties, can be controllably synthesized through top-down strategy via Hummer's oxidation methods of natural graphite. Different from bottom-up, top-down method is generally proceeded from raw materials like graphite and carbon nanotubes that need to overcome interlayer's Van der Waals force by either chemical oxidation or electrochemical exfoliation, and eventually achieve the introduction of functional groups or the scalable control of functionalization (e.g., graphene quantum dots [114]). There are three main advantages of the Top-down method: (1) Resource-richness. The resource's quantity is large and easy to get, such as normal carbon source graphite and carbon nanotubes, etc.; (2) Diversification of preparation process, including chemical exfoliation, electrochemical exfoliation, unzipping, etc.; (3) Operability in large-scale preparation of functionalized graphene.

As viewed from raw materials,  $\text{sp}^2$ -C dominant carbonaceous material with different functional groups or functional dimensions that prepared by Top-down method can be categorized into two main types: graphite type functionalized graphene, which is synthesized from graphite raw material such as graphite, expanded graphite and intercalated graphite, and non-graphite type functionalized graphene, which is composited from the non-graphite raw materials including carbon nanotubes and organic carbon sources.

$\text{Sp}^2$ -C dominant carbonaceous materials can be subdivided into covalently and non-covalently functionalized graphene according to the difference in functional groups. In covalently functionalized graphene, the edge or interior area of graphene sheets are derived from covalent bonds of functional groups, including the first generation covalently functionalized graphene derived directly from graphite, and the second and above generation that derived from the first generation covalent-bond functionalized graphene. Non-covalently functionalized graphene refers to graphene that functionalized by non-covalent bonds like hydrogen bond,  $\pi$ - $\pi$  bond, ionic bond, or host-guest form.

There are also some other non-graphite type functionalized graphene that can be utilized in synthesis of functionalized graphene, including carbon nanotubes, carbon black, normal carbon fibers, etc. Since carbon nanotubes are found, researchers have paid great attention to their remarkable electronic properties. Recently, their specific potential in functionalized graphene preparation which is called unzipping has been discovered. Thereafter their excellent prospects have been disclosed in this field.

On account of choosing the best strategy for graphene preparation from different types of raw materials, several proper synthesis methods have been endeavored, which can grant the properties each raw material possesses.

### 2.2.1. Chemical exfoliation

Graphite oxide (GO), first found in 19th century, is a kind of material that obtained through an oxidation process under the existence of graphite, strong acid and strong oxidant. So far, there are three main approaches for its preparation: Brodie method [115], Staudenmaier method, and Hummers method [116]. Compared with the other two approaches, Hummers method provide a more rapid, safe, efficient and simple process and has been labeled as the basic preparation method of graphite oxide. The diversification of oxidation degree can be controlled through adjusting the type of raw material graphite (size or species) or changing different oxidation systems. Graphite oxide has a similar layer structure as the graphite possesses, however, after oxidation, multiple oxygen-containing functional group such us hydroxyl, carboxyl, epoxy group would be covalently linked onto the graphite layers [117–120]. These groups are well hydrophilic, leading to a remarkable water or other polar solution dispersion ability of graphite oxide. Under the exfoliation effect of water or other polar solution, graphite oxide can be exfoliated into single layer ultimately which refer to graphene oxide (GO), as shown in Fig. 10.

The most widespread Hummers system for preparation of GO is a

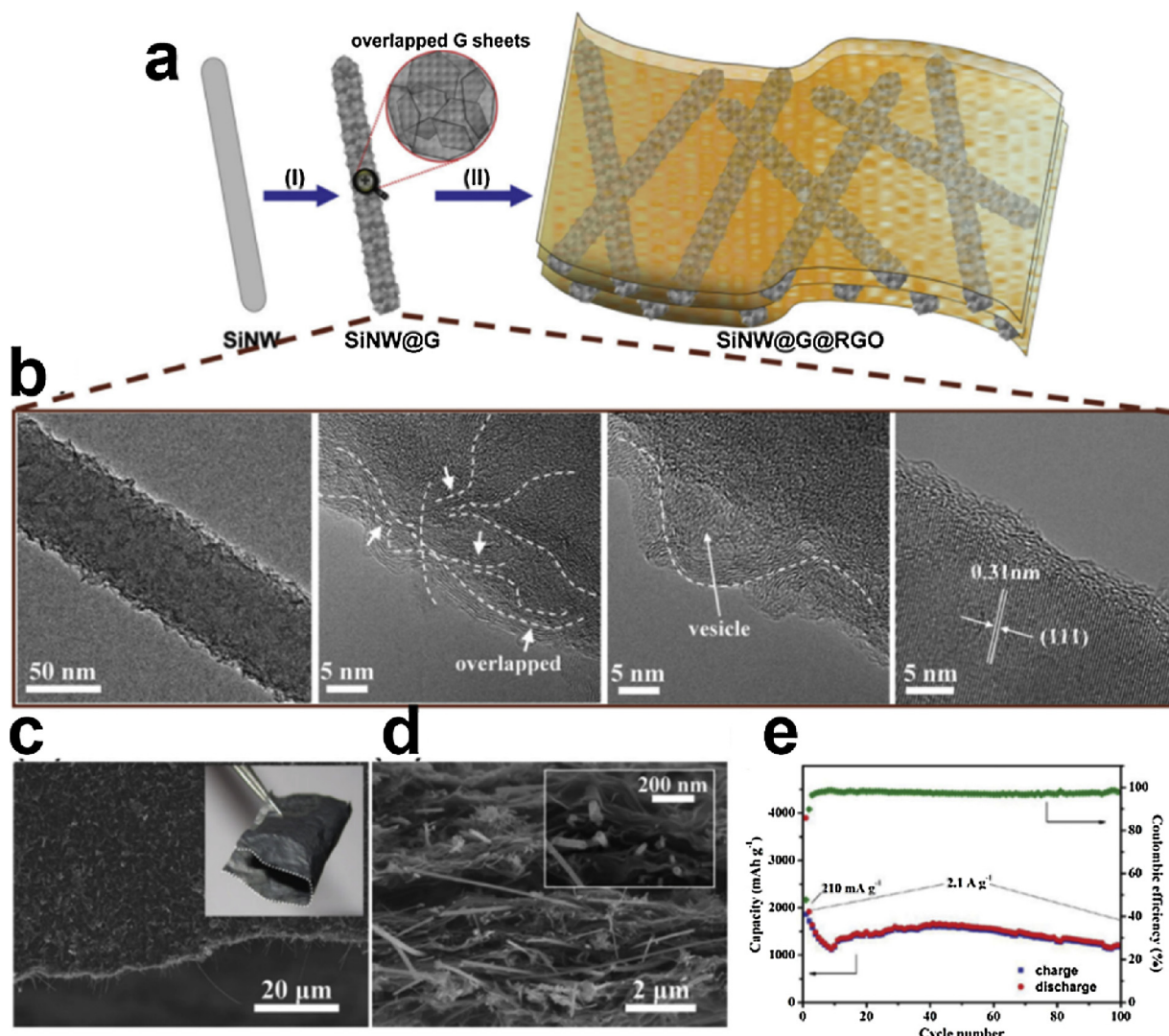


**Fig. 9.** (a) The fabrication process of SiNW@G@rGO. (b) HRTEM images of SiNW@G nanocables. (c,d) SEM images of SiNW@G@rGO. (e) Cycling performance of the SiNW@G@rGO. Reproduced from [100] Copyright 2013, American Chemical Society.

combination of concentrated sulfuric acid, potassium permanganate and sodium nitrate. With the rising demand for different functionalized graphene, researchers have paid great efforts to improve existing preparation technology. Marcano [121] group changed the ratio of  $\text{H}_2\text{SO}_4/\text{H}_3\text{PO}_4$  solvent system into 9:1, and increase the amount of potassium permanganate instead of the addition of sodium nitrate into the reaction on the basis of Hummers approach (Fig. 11). This improvement can eventually increase the yield of GO in a more environment-friendly way that avoids generation of poisonous nitric oxides. Also, controllable temperature during reaction process gives this approach a prospect in mass preparation of GO.

The structure and properties of GO are generally considered to be

influenced by the type of graphite and oxidant system, but practically, the quenching and purification process are suggested to play a key role. Dimiev [122] group adopted a non-aqueous system for the quenching and purification of GO (Fig. 12). The pristine graphene oxide (pGO) by this method contains plenty of ketone functional groups as the termination of defects, and the aromatic structural unit size is no larger than 5–6 benzene ring structure. The main  $\text{sp}^3$  component in pGO is epoxy group, and some covalent binding sulfur atoms and hydroxyl groups. Interestingly, new prepared GO powder by this method has a pale yellow color or just colorless, but after water cleaning several times, the color would return to normal brown due to the increasing systematic  $\pi$ - $\pi$  effect along with the reaction.

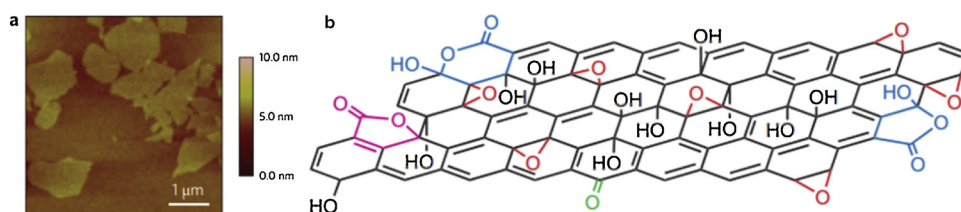


**Fig. 10.** (a) Atomic force microscopy (AFM) image of GO sheets on a silicon substrate. (b) New structural model of GO, taking into account the five- and six-membered lactol rings (blue), ester of a tertiary alcohol (purple), hydroxyl (black), epoxy (red) and ketone (green) functionalities. Reproduced from [118] Copyright 2009, Nature Publishing Group (For interpretation of the references to colour in this figure legend, the reader is referred to the web version of this article).

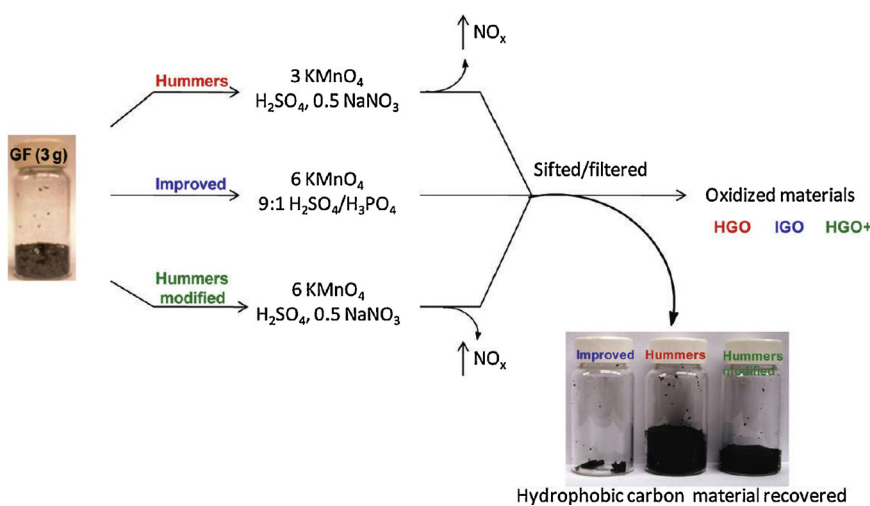


**Fig. 11.** Representation of the procedures followed starting with graphite flakes (GF). Under-oxidized hydrophobic carbon material recovered during the purification of IGO, HGO, and HGO+. The increased efficiency of the IGO method is indicated by the very small amount of under-oxidized material produced. Reproduced from [121] Copyright 2010, American Chemical Society.

Eigler [123] et al. revealed that hole defects on GO are mostly formed by  $\text{CO}_2$  elimination and the metastability of GO around elevated temperature of  $50^\circ\text{C}$  can be attributed to the formation of  $\text{CO}_2$  during oxidative synthetic protocol. Traditional preparation contains several reaction condition parameters, for example, the time, temperature, acid system, oxidative system, graphite resources, etc. Variation of these parameters can eventually achieve the goal of controlling the content of defective area, including the size and amount (Fig. 13).

To further strengthen oxidation degree of GO, Wang et al. proceeded Hummers oxidation after an oxidation pretreatment of  $\text{K}_2\text{SO}_8$  and  $\text{P}_2\text{O}_5$  to graphite. Chen group studied the synthesis of single layer and few-layers GO, which demonstrated that with the increase of reaction time and oxidant consumption, the average layer area of single layer GO would diminish (shrinking from  $59,000 \text{ nm}^2$  to  $550 \text{ nm}^2$ ), and the grain size showed a Gaussian distribution [124]. By controlling oxidative exfoliation process, 3 to 4 layers few-layers GO can be achieved with a similar water dispersibility as traditional GO. Under the same condition, few-layers reduced GO possessed a higher conductivity

than reduced single layer GO.

Optimizing synthetic procedure and reducing reaction time are also significant steps for improved preparation of GO. Liu's group focus on hydrothermal approach, through which a rapid preparation of GO and GO quantum dots can be obtained in 2 h with a ultrahigh 93% yield of GO and 10% yield of GO quantum dots [125]. This method implemented a controllable GO production via a simple adjustment in reaction temperature and ratio of different reactants, and this hydrothermal approach can execute the gram-level preparation of GO.

#### 2.2.2. Electrochemical exfoliation

Electrochemical exfoliation of graphite is a popular preparation approach for graphene in these years [126–129]. The cornerstone of this method is the electrolytic process of graphite electrode. A proper electrolyte and electrolytic conditions can exfoliate graphite thoroughly into few-layers graphene or even single layer graphene. Furthermore, similar to LIBs, electrolyte can be charged and discharged for several times, which would reduce contamination to environment. There are

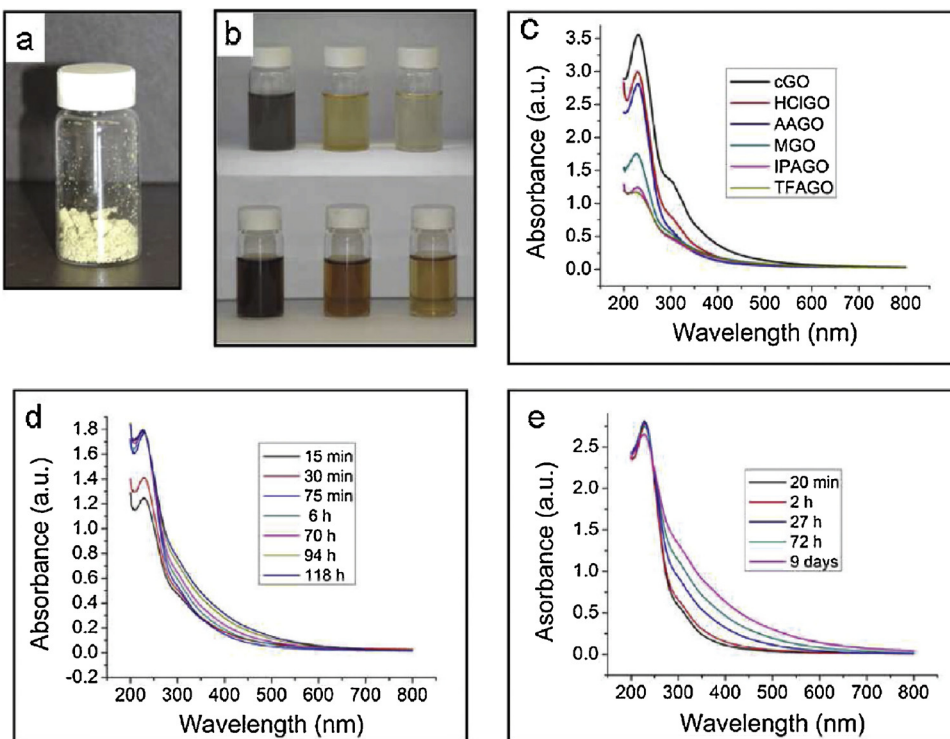


**Fig. 12.** (a) Photograph of dry TFAGO. (b) Photograph of the as-prepared aqueous solutions (top) of the following GO samples (left to right): cGO, MGO, and TFAGO. On the bottom: The same solutions after 24 h. The concentration of the solutions was  $0.5 \text{ mg mL}^{-1}$ . (c) The UV-vis spectra of the aqueous solutions of different GO samples; (d) the change in the UV-vis spectrum of the aqueous IPAGO solution with time. (e) the change in the UV-vis spectrum of the aqueous AAGO solution with time. Reproduced from [122] Copyright 2012, American Chemical Society.

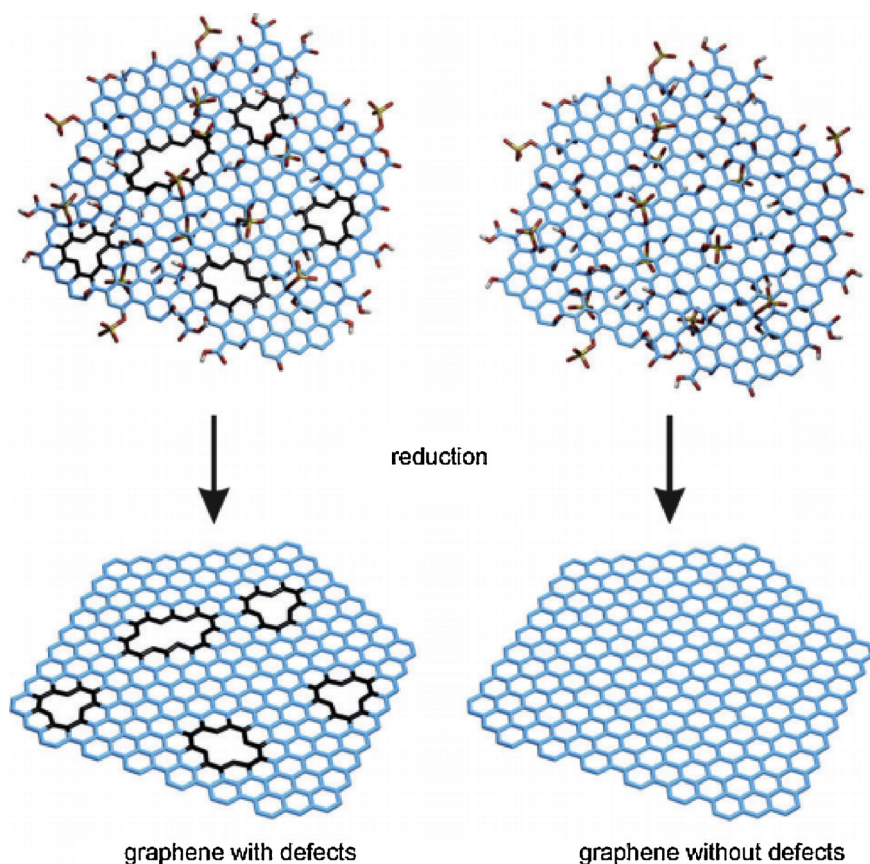


**Fig. 13.** Schematic representation of high defect reduced GO and low defect reduced GO. Reproduced from [123] Copyright 2013, Wiley-VCH.

several advantages that electrochemical exfoliation have: (a) mild preparation conditions: normal pressure and temperature are enough for preparing, without extreme conditions; (b) low manufacture cost: recyclable electrolyte can save integral cost of preparation; (c) less usage of poisonous chemical reagents leads to an environmental-friendly process; (d) a wide utilization range of graphite raw materials, from amorphous graphite to high grade graphite flakes; (e) prepared graphene possesses a high quality with no requirement for further treatment such us reduction or calcination; (f) controllability of graphene layer numbers and sheet size; (g) remarkable machinability and dispersibility make it a potential candidate in electromagnetic shielding, heat and electrical conducting functional coating; (h) the ability of in situ functionalization.

Compared with chemical exfoliation, non-oxidative process of electrochemical exfoliation enables less defects, besides, well crystalline in graphene sheets. Additionally, removal of high concentrated sulfuric acid eliminates the danger of critical thermal effect and the post-treatment of sulfuric acid waste, which makes all the process greener. Moreover, graphene prepared via this method can get thinner thickness and larger two dimensional sheets than mechanical exfoliation, and easier to get single layer graphene without ball-milling step.

This method can even be used to generate graphene directly on amorphous graphite from raw ore in only one step, which not only provides a feasibility for refinement of amorphous graphite but also simplify graphene preparation procedure. Natural graphite which endures a relative long and complexing extraction procedure in proto phase is the main stock for graphene's scalable manufacture, such an extraction procedure is a hardship because of the poor floatability excludes graphite from flotation technique and makes it harder for refining. In consideration of the abundant and cheap graphite source in China, electrochemical exfoliation enable graphite to be exfoliated into graphene from the raw ore in an easier way which curtails complicating

technological process and cuts down the cost. Above all, electrochemical exfoliation is a potential approach of functionalized graphene's mass preparation. The produced functionalized graphene has a relative low defect concentration,  $I_D/I_G$  is less than 0.4. Parvez's group has prepared 1–3 layers functionalized graphene with a 80% yield and a 12.3 C/O ratio, which point to a superb structure preservation [130].

The main mechanism of electrochemical exfoliation is the insertion of different ions, including  $\text{SO}_4^{2-}$ ,  $\text{OH}^-$ ,  $\text{HSO}_4^-$ , etc. Diameters of these ions are around 0.64 nm, which is slightly larger than the interlayer distance of graphite (0.34 nm), and ensures the efficiency of insertion to expand graphite's lamellar structure and achieves the ultimate exfoliation.

There are two types of electrochemical exfoliation: (a) anodic intercalation and (b) cathodic intercalation. In anodic intercalation, low voltage electrolyzes water into  $\text{OH}^-$  and  $\text{O}^{2-}$  that can expand the edges of graphite layer in the first step. Second,  $\text{SO}_4^{2-}$  intercalated into graphite layers under high voltage and achieved expansion and exfoliation of graphene. In contrast, cathodic reaction intercalates cations into graphite layers, such as  $\text{Li}^+$  and  $\text{Et}_3\text{NH}^+$ .

In anodic intercalation method, pH value of the electrolyte and voltage play an important role in the intercalation performance. Researchers have proved that anions including  $\text{OH}^-$ ,  $\text{O}^{2-}$ ,  $\text{SO}_4^{2-}$  intercalate rapidly in strong acidic electrolyte and generate lots of organic functional groups during oxidizing on graphene sheet (Fig. 14). Similarly, intense voltage can get a rapid intercalation compared with low voltage, but it would causes a higher oxidation degree. Although cathodic intercalation method will not create such oxidation on graphene, the overlong reaction time (over 10 h) eliminates its potential in scalable preparation of graphene. Therefore, searching for a proper electrochemical approach to meet both the conditions of low oxidation degree and high efficiency is a significant orientation in the future development of graphene electrochemical exfoliation.

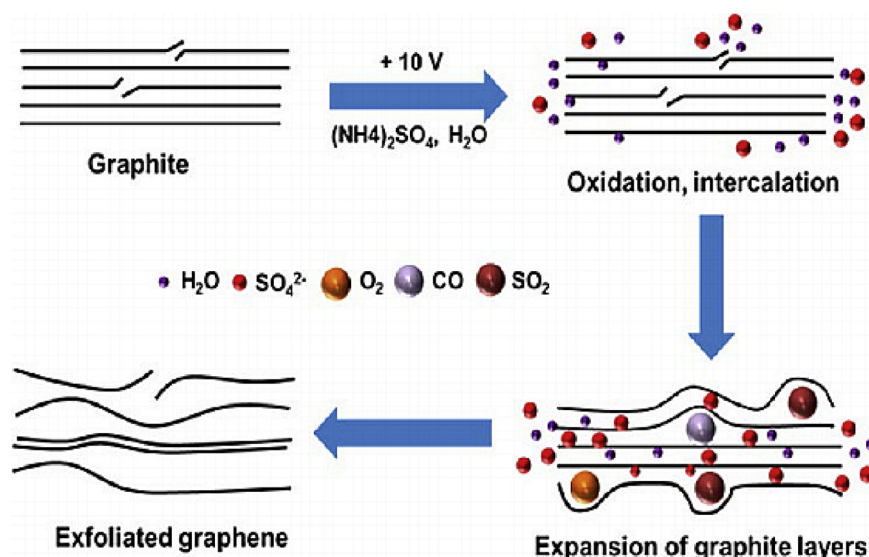


**Fig. 14.** Schematic diagram of the low oxidation degree graphene preparation process by electrochemical exfoliation. Reproduced from [130] Copyright 2013, American Chemical Society.

Introduction of diazonium salt sometimes has a vital influence on electrochemical exfoliation process. Dryfe's group proposed a one-step electrochemical exfoliation and modified preparation approach for the first time [131]. With the help of diazonium salt, they realized functionalization and exfoliation simultaneously under same voltage during electrochemical process.

Simultaneity of exfoliation and functionalization ensures that single layer and few layers graphene can be stabilized by in situ functionalization before aggregation happens, and get a stable dispersion eventually. In an aqueous dispersion system, dispersibility performance of graphene functionalized by diazonium salt is two orders of magnitude greater than traditional electrochemical exfoliation production without functionalization. There are several outstanding advantages for diazonium salt. First, attributed to diazonium salt N<sub>2</sub> generated during reduction contribute a lot to dispersion process of graphene sheet. Second, functionalization degree can be controlled by the concentration of diazonium salt. This work also utilized the controllably prepared graphene-supercapacitor with higher charge storage capacity. Moreover, the author has demonstrated that specific electrical-capacity is influenced by functionalization degree to some extent. This one-step electrochemical exfoliation and functionalization graphene preparing method is promising in application among various fields. Cao's group reported a two-step approach including electrochemical intercalation and oxidation for the preparation of graphene oxide recently [132]. The first step was achieving intercalation in concentrated sulfuric acid, and second, implementing the oxidation and exfoliation in 0.1 M ammonium sulfate, eventually obtain graphene oxide with a 70% yield (single layer ratio about 90%, oxygen content about 17.7%).

This work enlightened a lot of attention in electrochemical exfoliation in graphene chemistry field. Very recently, Ren et al. raised a novel water electrolysis oxidation idea, broke traditional way of graphite oxidation with strong oxidant, ultimately

achieved a ultrafast, green and safe preparation process (Fig. 15) [133]. The authors demonstrated that firstly dip graphite paper into concentrated sulfuric acid to be intercalated, and then the oxidation process occurred on intercalated graphite in diluted sulfuric acid. Isotopic tracing of oxygen element and free radical experiment exhibited that the oxygen element in GO is mainly from the water in electrolyte. Plentiful high reactive free radicals generated by water electrolysis react with graphite and finally form graphene oxide. Sulfuric acid in the reaction has hardly any loss or produce other compounds, which means it can be recycled for electrochemical reaction. This effective approach

solved the problem that graphene oxide's preparation always faces explosion risk, environmental pollution and relative long reaction period for a long time, which give a hopeful prospect of graphene oxide's industrialized application.

#### 2.2.3. Unzipping

Carbon nanotube is a kind of 1D nanomaterial composited of carbon. It is an axial nanotube that built up by hexagonal carbon with several or even dozens of layers which possess a constant interlayer distance about 0.34 nm and a diameter ranges from 2 to 20 nm. Furthermore, it is also a potential raw material for non-graphite type functionalized graphene, mainly for graphene nanoribbons.

Since Kosynkin [51] et al. invented a graphene nanoribbons' preparation method proceeded from carbon nanotubes, researchers started to focus on the functionalized graphene nanoribbons and relative derivatives. This method using a combination of H<sub>2</sub>SO<sub>4</sub>/KMnO<sub>4</sub>, unzipping nanotubes along axes and gets graphene nanoribbons (Fig. 16). Width of the graphene nanoribbons ranges from 100 to 500 nm and length are about 4 μm, with 1 to 30 layers per nanoribbon. The nanoribbon synthesized by this method is still crude, as it has more defect areas and oxygen-containing functional groups, reducing its electroconductivity eventually.

According to previous researches on oxidation of carbon nanotubes, Higginbotham [134] et al. demonstrated an innovative improvement: to introduce a second weaker acid (C<sub>2</sub>H<sub>3</sub>F<sub>3</sub>O<sub>2</sub> or H<sub>3</sub>PO<sub>4</sub>) into conventional H<sub>2</sub>SO<sub>4</sub>/KMnO<sub>4</sub> system to restrain in generation of defects that caused by O-diol group. This method improves graphene nanoribbons' conductivity and give a more regular edges.

Dai's group used the experience of etching technique from semiconductor industry to section carbon nanotubes, then adhered it on a polymer thin film for the first time. After an etching process under argon plasma, a graphene nanoribbon with a 10–20 nm width can be achieved (Fig. 17) [135].

Based on these previous experiments, Dai's group proposed a more facile and effective preparation method for graphene nanoribbons (Fig. 18) [136]. The optimization includes two steps, i.e., gas phase oxidation and liquid phase ultrasonication. Under a mild gas phase oxidation process, oxygen reacts with defects on the side wall and forms corrodible holes. In the following liquid phase ultrasonication step, both integrated ultrasonic chemistry effect and the hot air bubbles act on the corrodible holes and amplify it until achieving the section. Graphene nanoribbons based on this method possess advantages such

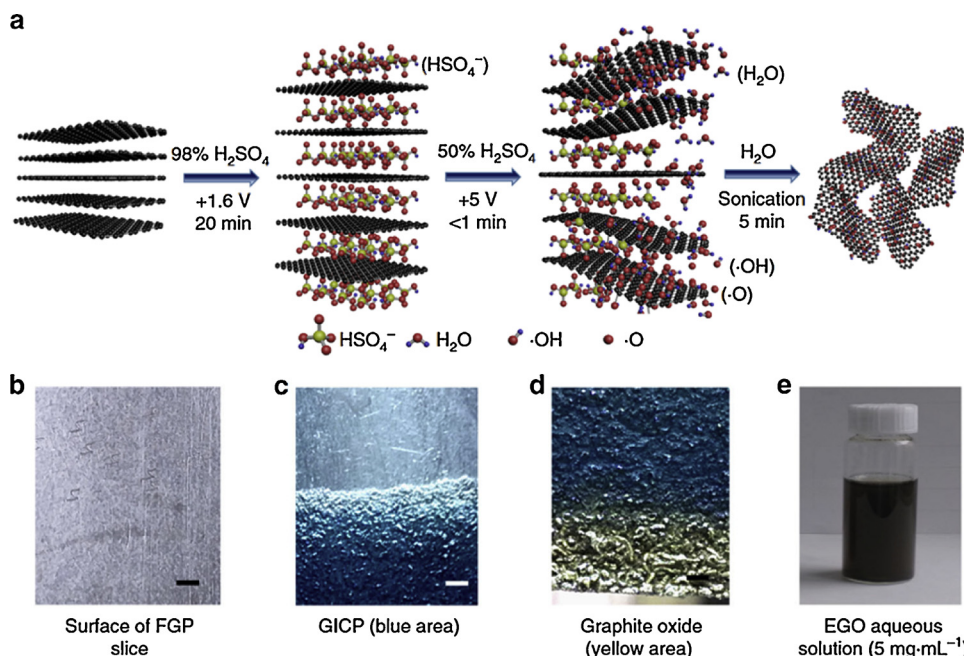


**Fig. 15.** (a) Schematic illustration of the synthesis process of EGO by water electrolytic oxidation. (b–e) Photos of the raw material and the products obtained at each step. (b) FGP, (c) GICP (blue area) obtained after EC intercalation of FGP in 98 wt% H<sub>2</sub>SO<sub>4</sub> at 1.6 V for 20 min. (d) Graphite oxide (yellow area) obtained by water electrolytic oxidation of the GICP in 50 wt% H<sub>2</sub>SO<sub>4</sub> at 5 V for 30 s. (e) Well-dispersed EGO aqueous solution (5 mg mL<sup>-1</sup>) obtained by sonication of the graphite oxide in water for 5 min. Reproduced from [133] Copyright 2018, Nature Publishing Group (For interpretation of the references to colour in this figure legend, the reader is referred to the web version of this article).

as smooth edge, less defects and high conductivity.

Meanwhile, our group is working on the top-down approach for graphene exfoliation as well. Focusing on the application of flexible transparent conductive film (FTCFs), selection of graphene preparation method becomes significant considering the performance. Compared with other graphene preparation method like CVD, top-down strategy possesses a low-cost and transfer-free route for the mass production of large area graphene oxide, and chemical reduction seems to be the most suitable approach for FTCFs with its milder and easier reaction conditions.

Liang et al. considered about the influence of molecule diameter on the GO reduction atomic efficiency, and presented a green and highly

efficient reduction way in solid state instead of in solution [137]. Under catalysis of Pd, hydrogen can be utilized as a feasible reductant of GO and give a good result on conductivity in both thin (400 nm) and thick (2.9 μm) rGO films (greater than 40,000 S m<sup>-1</sup>). Ning et al. demonstrated an ultrafast Sn<sup>+</sup>/EtOH solution-based reduction process of GO for application in FTCFs, got a rGO based FTCFs with a 82.9%–91.9% transmittance and a resistance of 800–3840 Ω sq<sup>-1</sup> in only 5 min (Fig. 19) [138].

**Table 1** summarizes the methodologies for sp<sup>2</sup>-C dominant carbonaceous materials that were synthesized from the bottom-up strategy and top-down strategy mentioned above.

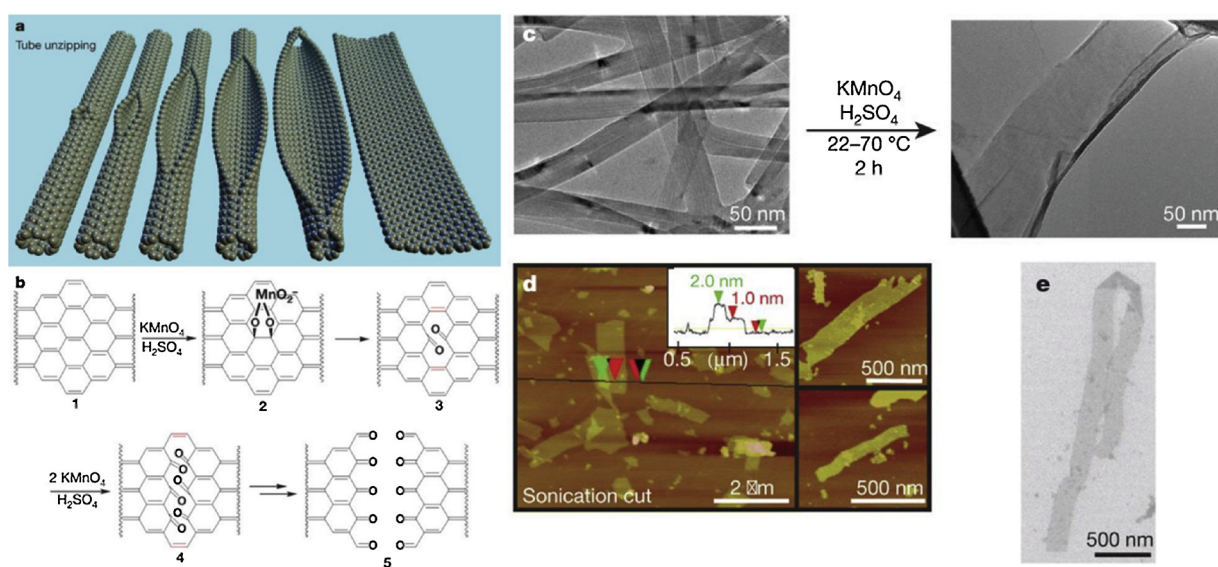


**Fig. 16.** (a) Representation of the gradual unzipping of one wall of a carbon nanotube to form a nanoribbon. Oxygenated sites are not shown. (b) The proposed chemical mechanism of nanotube unzipping. The manganese ester in 2 could also be protonated. (c) TEM images depicting the transformation of MWCNTs (left) into oxidized nanoribbons (right). The right-hand side of the ribbon is partly folded onto itself. The dark structures are part of the carbon imaging grid. (d) AFM images of partially stacked multiple short fragments of nanoribbons that were horizontally cut by tip-ultrasonic treatment of the original oxidation product to facilitate spin-casting onto the mica surface. The height data (inset) indicates that the ribbons are generally single layered. The two small images on the right show some other characteristic nanoribbons. (e) SEM image of a folded, 4-μm-long single-layer nanoribbon on a silicon surface. Reproduced from [51] Copyright 2009, Nature Publishing Group.

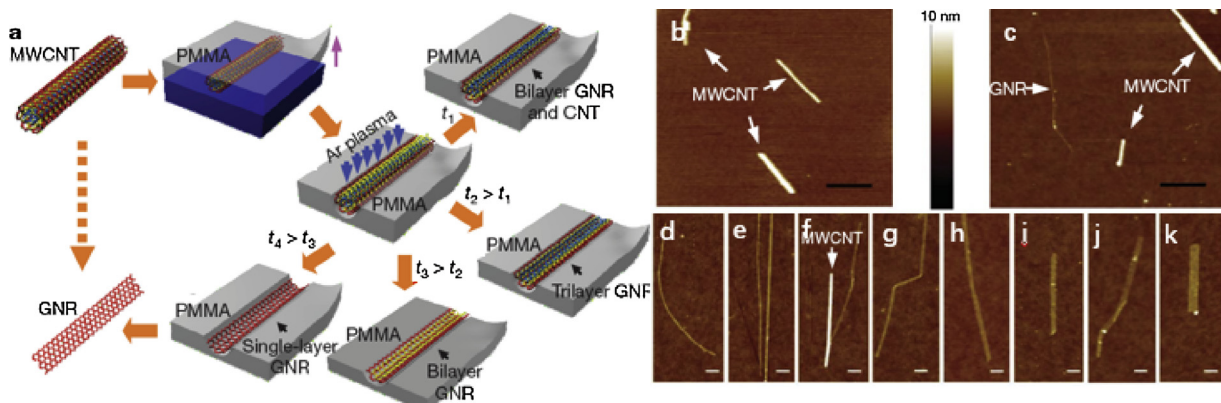


**Fig. 17.** (a) A pristine MWCNT was used as the starting raw material. Then MWCNT was deposited on a Si substrate and then coated with a polymethyl methacrylate (PMMA) film. The PMMA–MWCNT film was peeled from the Si substrate, turned over and then exposed to an Ar plasma. Several possible products were generated after etching for different times: GNRs with CNT cores were obtained after etching for a short time  $t_1$ ; tri-, bi- and single-layer GNRs were produced after etching for times  $t_2$ ,  $t_3$  and  $t_4$ , respectively ( $t_4 > t_3 > t_2 > t_1$ ). The PMMA was removed to release the GNR. (b) An AFM image of raw MWCNTs dispersed on a Si substrate. (c) An image of the substrate after the GNR conversion process, showing coexistence of MWCNTs and GNRs. Scale bars, 1 mm. (d–k) Single- or few-layer GNRs of different widths and heights. Reproduced from [135] Copyright 2009, Nature Publishing Group.

### 3. Sp<sup>2</sup>-C dominant carbon materials for energy storage applications

Sp<sup>2</sup>-C dominant carbon materials are considered to be promising electrode materials for energy storage applications due to their chemical tunability, conjugated network, and topological structure. In addition, the excellent mechanical strength and electrochemical properties, as well as high SSA can meet the general requirements for electrochemical energy storage. In this section, recent progress involving sp<sup>2</sup>-C dominant carbon materials in energy storage applications is discussed, including LIBs and supercapacitors.

#### 3.1. Applications for lithium ion batteries

Rechargeable LIBs consist of negative electrode, positive electrode and electrolyte-wetted separator, in which Li-ions shuttle between the negative electrode (commonly graphite) and the positive electrode (commonly a layered lithium metal oxide), while the charge can be compensated by transfer of electrons via the external circuit, which can afford adequate energy to power an application system. Because of their superior conductivity, high surface area, and/or abundant porosity, sp<sup>2</sup>-C dominant carbon materials can serve as component materials (anode materials) or functional additives (buffer media or conductive networks). Commercialized LIBs have stimulated a surge in many fields such as portable electronic devices, electric vehicles, smart grids, and renewable energy utilizations, due to their predominant advantages

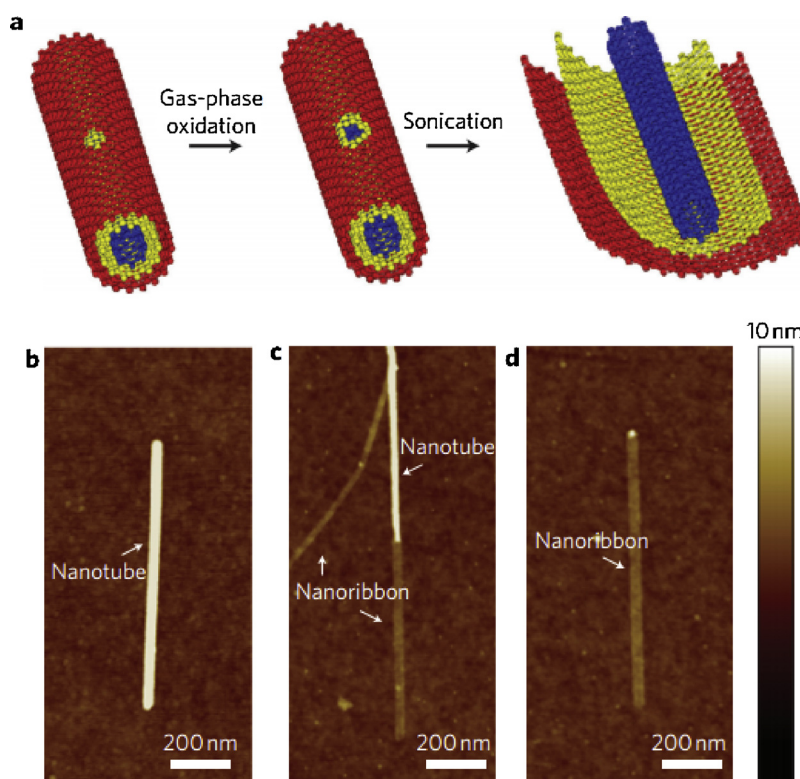


**Fig. 18.** (a) Schematic of the unzipping processes. In the mild gas-phase oxidation step, oxygen reacts with pre-existing defects on nanotubes to form etch pits on the sidewalls. In the solution-phase sonication step, sonochemistry and hot gas bubbles enlarge the pits and unzip the tubes. (b–d) AFM images of pristine, partially and fully unzipped nanotubes, respectively. The heights of the nanoribbons in c and d are 1.4 and 1.6 nm, respectively, much lower than the pristine nanotube shown in b (height ~9 nm). Reproduced from [136] Copyright 2010, Nature Publishing Group.

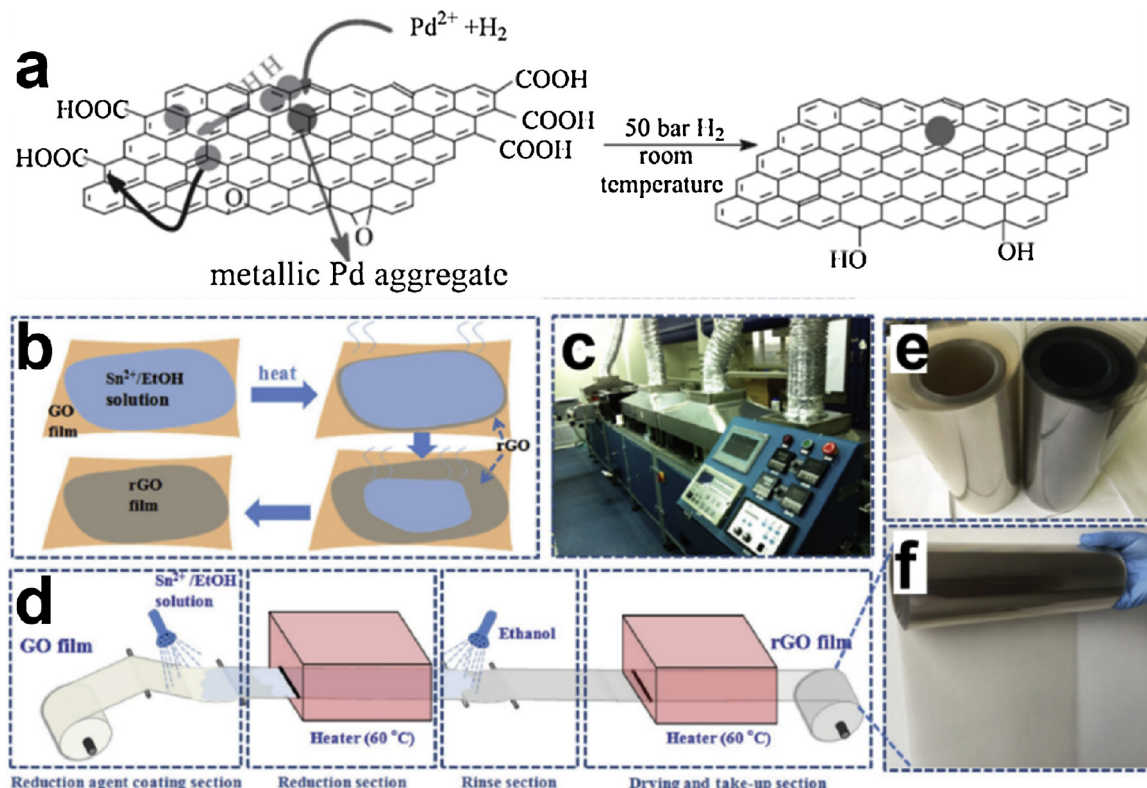


**Fig. 19.** (a) Proposed mechanism of Pd catalytic reduction of GO. (b) Schematic of GO film reduction process based on  $Sn^{2+}/EtOH$  solution. (c) Simulated production line for the process. (d) Digital photos of GO and rGO films in rolls after the production line. (e) Detailed photo of rGO film roll. (f) Details of the roll-to-roll technique production line. Reproduced from [138] Copyright 2017, Wiley-VCH.

**Table 1**  
Methodologies for  $sp^2$ -C dominant carbonaceous materials and related examples.

Strategies	Methods	Examples
Bottom-up strategy	Monomer-controlled synthesis	polycyclic aromatic hydrocarbons (PAHs) [34,35,36] hexaphenylbenzenes [37] fully $sp^2$ -carbon frameworks [46] longitudinally well-extended (200 nm) GNRs [55] thermalized triazine-based networks [60]
	Biopolymer transformation	importance of physiologic function of plant in the porosity and microstructure of yielding carbonaceous materials [67] sheet-like porous carbon derived from eggplant [78] pyrolyzed bacterial cellulose (PBC) [80]
	Chemical vapor deposition	growth of graphene on copper substrate [93] single layer graphene on liquid metal gallium [94] 3D foam-like graphene foams [98] $sp^2$ -C dominant carbonaceous sheaths grown on the silicon nanowires [100,101]
Top down strategy	Chemical exfoliation	Single layer graphite oxide [118] GO produced with high yield in a more environment-friendly way [121] quenching and purification of GO [122] single layer and few-layers GO [124]
	Electrochemical exfoliation	simultaneous functionalization and exfoliation of graphene [131] electrochemical intercalation and oxidation for GO [132] water electrolysis oxidation of GO [133]
	Unzipping	restrain in generation of defects for GNRs [134]; section of carbon nanotubes via etching technique [135] gas phase oxidation and liquid phase ultrasonication for GNRs [136]

such as high energy density, high voltage, no memory effect, long cycle life, and environmental friendliness. To satisfy the stringent requirements of high energy storage system, a large amount of electrode (anode and cathode) materials with high specific capacities have thus far been widely exploited in recent years [139]. However, the pronounced volume change of high-capacity electrode materials upon cycling can weaken or even disintegrate the electron/Li-ion transport network. The nanosizing has thus far been shown to be a transformative way to improve the structural stability of these high capacity electrode

materials, where the strain in such nanostructured materials can be easily relaxed benefiting from their small size and available surrounding free space. Unfortunately, the nanostructured materials intrinsically suffer from high interparticle resistance and low tap density, which severely impede the electrical and ionic pathways during cycling. In this context,  $sp^2$ -C dominant carbon materials with conjugated network, mechanical strength and smooth electron passway, have been rationally introduced onto nanostructured active materials, which substantially help improve electronic and ionic conductivity, optimize

spatially dispersibility, and eventually enhance the performances of electrodes.

### 3.1.1. Anodes materials

In principle,  $sp^2$ -C dominant carbon materials can be utilized directly as anode materials in LIB, benefiting from their intrinsic structural stability and superior conductivity [62,140–142]. For example, Xu et al. found N-doped holey graphene (N-hG) anode for LIB prepared by simply heating hG in ammonia gas [140]. The thus-obtained anode materials exhibited a high volumetric capacity of  $384 \text{ mA h cm}^{-3}$  at  $0.1 \text{ A g}^{-1}$ , a maximum volumetric energy density of  $171.2 \text{ Wh L}^{-1}$ , and a maximum volumetric capacitance of  $201.6 \text{ F cm}^{-3}$  at  $5 \text{ A g}^{-1}$  during the 6000 cycles tested. The excellent electrochemical performance of N-hG was attributed to a synergistic effect of nitrogen doping and holes to provide high electrical conductivity, reduced effective diffusion distance, and numerous active sites for  $\text{Li}^+$  storage. Furthermore, it is envisioned that the malleable amorphous structures can readily accommodate the local volume change during the lithiation-delithiation process. Besides, N-hG with a high packing density and excellent ion transport/storage endowed high energy densities (both gravimetric and volumetric) and ultralong cycling life when used as anode materials for LIBs. In the work reported by Xiao et al., the developed novel N-enriched carbon/carbon nanotube composite (NEC/CNT) was successfully synthesized through a chemically induced precursor-controlled pyrolysis approach. This Schiff-based network (SNW-1), instead of using conventional N-containing sources or precursors, enables the desirable combination of a 3D polymer with intrinsic microporosity and ultrahigh N-content (21% in the resultant NEC/CNT). The as-obtained anode material exhibited a super-high capacity ( $1050 \text{ mA h g}^{-1}$ ) after 1000 cycles and excellent rate performance ( $500 \text{ mAh g}^{-1}$  at a current density of  $5 \text{ A g}^{-1}$ ) for LIBs, which mainly results from the fast transport of both  $\text{Li}^+$  and electron in the highly porous and N-doped carbon network [62]. Besides, Jiao et al. successfully prepared high-quality graphitized graphene by solid-exfoliation of graphite and a subsequent wet chemical process. In the thus-obtained designed materials, the excellent structural stability during repetitive cycling, the highly conductive nature facilitating the conduction of electrons and the diffusion of lithium ions as well, and the large surface-to-volume ratio which is beneficial to the infiltration of the electrolyte resulting in a large contact area between the electrolyte and the electrode, all resulted excellent electrochemical performance. Recently, Xie et al. prepared a sandwich-like, graphene-based porous nitrogen-doped carbon (PNCs@Gr) through facile pyrolysis of zeolitic imidazolate framework (ZIF) nanoparticles in situ grown on graphene oxide (GO) (ZIF-8@GO) [142]. When used as anode materials for LIBs, this well-designed carbonaceous materials delivered remarkable capacities, excellent rate and cycling performance, which belongs to one of the best results among carbonaceous electrode materials and even exceeds most metal oxide-based anode materials derived from metal organic frameworks (MOFs). This impressive electrochemical performance can be attributed to an ideal combination of hierarchically porous structure, a highly conductive graphene platform, and high-level nitrogen doping in the sandwich-like PNCs@Gr electrode obtained.

### 3.1.2. Buffer media & conductive network

Building electron and ion transport pathways for active electrode materials are critically important toward the development of high-power, high-energy, and stable electrochemical energy storage systems such as the typical lithium-ion batteries. A wide range of active anode and cathode materials have thus been incorporated into  $sp^2$ -C dominant carbonaceous materials toward the direct construction of self-supporting binder-free anodes and cathodes for high-performance LIBs.

By engineering the arrangement of graphene sheets, Zhou et al. recently developed an rationally designed graphene-based self-supporting binder-free electrode configuration (denoted as TCG-Si), where silicon nanoparticles were embedded within the assemblies of

templated carbon-bridged oriented graphene via a modified vacuum filtration process followed by a thermal annealing (Fig. 20) [143]. The thus-obtained engineered graphene bulk assemblies afforded high gravimetric capacity ( $1390 \text{ mA h g}^{-1}$  at  $2 \text{ A g}^{-1}$  with respect to the total electrode weight), high volumetric capacity ( $1807 \text{ mA h cm}^{-3}$  that is more than three times higher than that of commercial graphite), superior rate capability ( $900 \text{ mA h g}^{-1}$  at  $8 \text{ A g}^{-1}$ ), excellent cycling stability (0.025% decay per cycle over 200 cycles), and competing areal capacity (as high as 4 and  $6 \text{ mA h cm}^{-2}$  at 15 and  $3 \text{ mA cm}^{-2}$ , respectively). The robust bi-continuous network in such structure endowed rapid transport of both electrons and lithium ions from/to impregnated silicon nanoparticles across the whole electrode even with a high mass loading.

Furthermore, Zhang et al. demonstrated a scallop-inspired shell engineering strategy to confine high-volume-change silicon micro-particles toward the construction of binder-free yet stable lithium battery anodes with high volumetric capacity, in which, as for each silicon microparticle, the methodology involves an inner sealed but adaptably overlapped graphene shell, and an outer open hollow shell consisting of interconnected reduced graphene oxide, mimicking the scallop structure (Fig. 21) [144]. The inner closed shell enables simultaneous stabilization of the interfaces of silicon with both carbon and electrolyte, and substantially facilitates efficient and rapid transport of both electrons and lithium ions from/to silicon. Additionally, the outer open hollow shell creates stable and robust transport paths of both electrons and lithium ions throughout the electrode without any sophisticated additives. The resultant self-supported electrode exhibited stable cycling with rapidly increasing Coulombic efficiency in the early stage, superior rate capability, and remarkably high volumetric capacity upon a simple pressing process. Very recently, Sun et al. fabricated a monolithic three-dimensional, hierarchically-porous, free-standing network electrode (denoted as  $\text{Nb}_2\text{O}_5/\text{HGF}$ ) via a two-step approach (Fig. 22). The  $\text{Nb}_2\text{O}_5/\text{HGF}$  hybrid electrode delivered high areal capacity and high-rate capability at high mass loading [145]. Typically, it exhibited much less capacity degradation induced by the increase of mass loading at high C-rates. As a result a capacity of  $139 \text{ mA h g}^{-1}$  was maintained with  $11 \text{ mg cm}^{-2}$  loading at a high rate of 10 C, demonstrating the potential of collaborative engineering of  $sp^2$ -C dominant carbon hybrids at both the material scale and the electrode scale to promote the development of viable high-performance LIB electrodes. The highly interconnected three-dimensional graphene/holey graphene achieves a synergistic combination of network architecture offering excellent electron transport properties, and hierarchical porous structure facilitating rapid ion transport even with a high mass loading of  $\text{Nb}_2\text{O}_5$  nanoparticles, and thus results in the outstanding electrochemical performances. In addition, Miao et al. formed a sandwich-like binder-free electrode (denoted as RHG-Si) by the highly dispersible functional moiety (hydroxyl and epoxy groups)-specific functionalized graphene (denoted as HG) was mixed with commercial silicon nanoparticles, filtrated, and reduced by HI reduction processing. The thus-obtained hybrids achieved a significant enhancement of rate performances, which are mainly attributed to the introduced RHG matrix into binder-free sandwich-like electrode architecture possessing greatly improved structural integrity and interfacial cleanliness compared to the rGO.

Significantly, the intrinsic structure change of nanostructured active materials and electrode during cycling can be considerably buffered by the strong  $sp^2$ -C dominant carbon materials, resulting in a smooth electron/lithium ion transport network and stable interface between active materials and electrolyte. For instance, Hassan et al. developed a synergistic physicochemical alteration of electrode structures (Fig. 23), in which strong covalent interactions occurring between silicon nanoparticles and sulfur doped graphene (SG) as well as cyclized polyacrylonitrile (c-PAN) provide a robust nanoarchitecture [146]. This hierarchical structure not only effectively prevented the agglomeration of Si to maintain the material stability, but also facilitated the charge

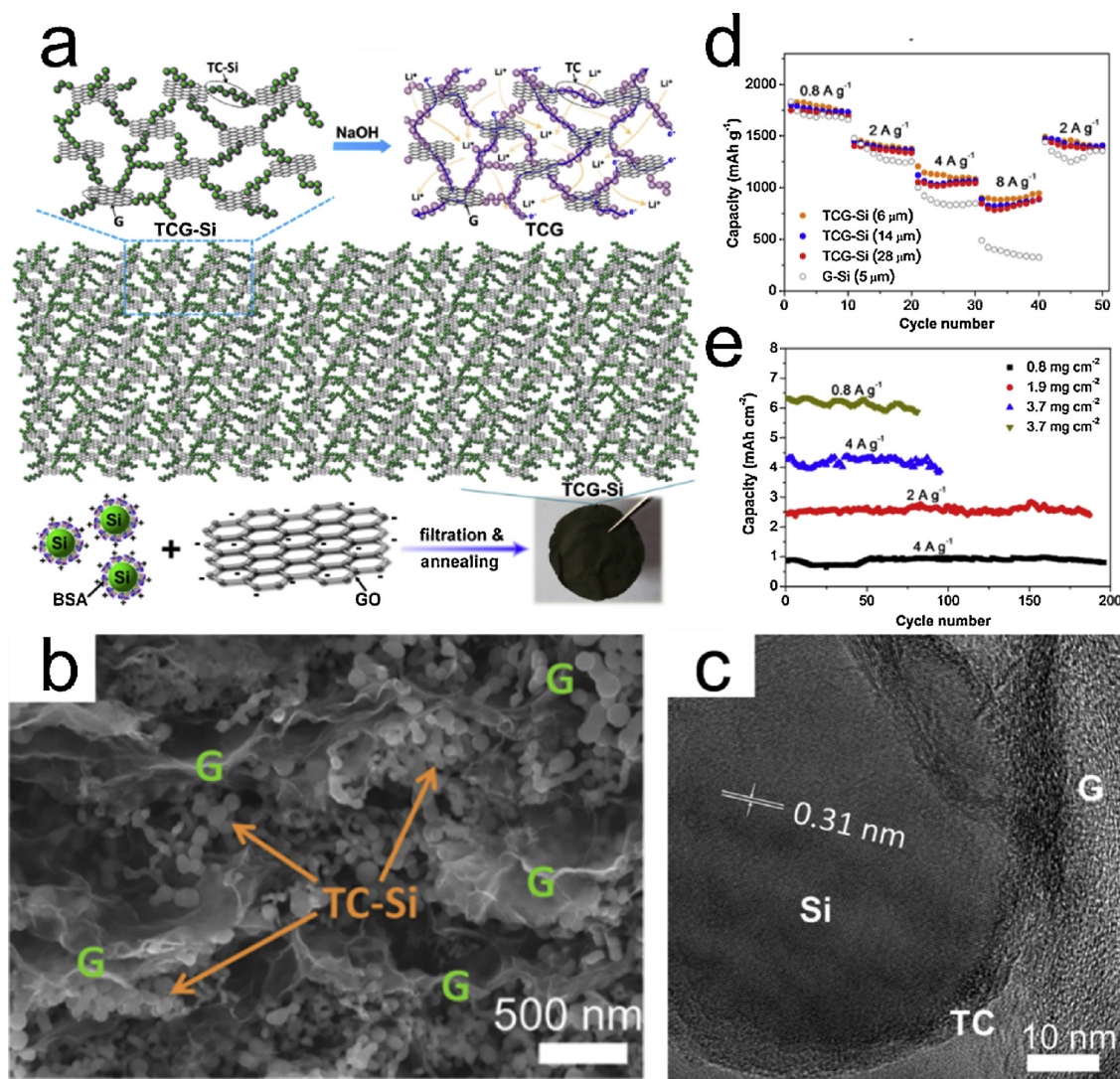


**Fig. 20.** (a) Fabrication and electrode design. (b) SEM image. (c) TEM image. (d) Rate capabilities. (e) Areal capacities with different mass loadings of the TCG-Si. Reproduced from [143] Copyright 2015, American Chemical Society.

transfer across the whole electrode. Meanwhile, the design on the nanoscale reduced the contact of the electrolyte with the electrode and thus stabilized the solid electrolyte interphase (SEI), yielding superior reversible capacity, high Coulombic efficiency of 99.9% and high stability even with a high electrode loading associated with  $3.4 \text{ mA h cm}^{-2}$ .

In addition, Wang et al. developed a wire-in-tube structure (namely, SiNW-d-GT), in which silicon nanowires were enveloped within hollow tube-like  $\text{sp}^2$ -C dominant carbon materials by a CVD process (Fig. 24) [147]. The thus-resulted hybrids delivered good rate capability ( $1200 \text{ mA h g}^{-1}$  at  $12\,600 \text{ mA g}^{-1}$ ) and remarkable cycling stability ( $1100 \text{ mA h g}^{-1}$  at  $4200 \text{ mA g}^{-1}$  over 1000 cycles) when used as anode materials of LIBs. The excellent cycling performance was believed to originate from the rational structure design. The incorporated void space from  $\text{sp}^2$ -C dominant carbon materials not only accommodated the volume change of inner active materials, but also maintained a robust line-to-line contact between the components while the backbone, which effectively avoided the direct exposure of silicon to the electrolyte, improved the stability of the SEI layer and alleviate electrolyte decomposition. Following this design concept, Wang et al. developed a kind of adaptable, self-supporting, flexible, and binder-free paper-like silicon-based anode (namely, SiNW@G@rGO) [148]. In this anode, overlapped graphene sheets were on the one hand grown on the

silicon nanowires to form SiNW@G core-sheath nanocables, and on the other hand sandwiched inside reduced graphene oxide sheets. The SiNW@G@rGO anode exhibited greatly enhanced lithium storage performance when compared with their counterparts, delivering reversible specific capacity of  $1600 \text{ mA h g}^{-1}$  at  $2.1 \text{ A g}^{-1}$ , 80% capacity retention after 100 cycles, and superior rate capability ( $500 \text{ mA h g}^{-1}$  at  $8.4 \text{ A g}^{-1}$ ) based on the total electrode weight. This can be probably attributed to the following aspects: Firstly, the overlapped graphene sheets functioned as adaptable but sealed sheaths or mediators to synergistically transform with the volume change of embedded silicon nanowires, thus preventing the direct contact of silicon with the electrolyte and enabling the structural and interfacial stabilization of encapsulated silicon nanowire materials during repeated cycling. Secondly, the flexible and conductive reduced graphene oxide overcoats acted as a mechanically robust bulk matrix or framework to accommodate the volume change of embedded SiNW@G core-sheath nanocables, thus maintaining the structural and electrical integrity of the bulk electrode.

Furthermore, Wu et al. constructed an interconnected network of graphene wrapped porous silicon nanoparticles from silicon precursors (silica particles) through the layer-by-layer assembly and magnethothermic reduction process [149]. The as-synthesized hybrids exhibited remarkably enhanced specific capacity, cycling stability, and rate capability, which can be attributed to the structural features

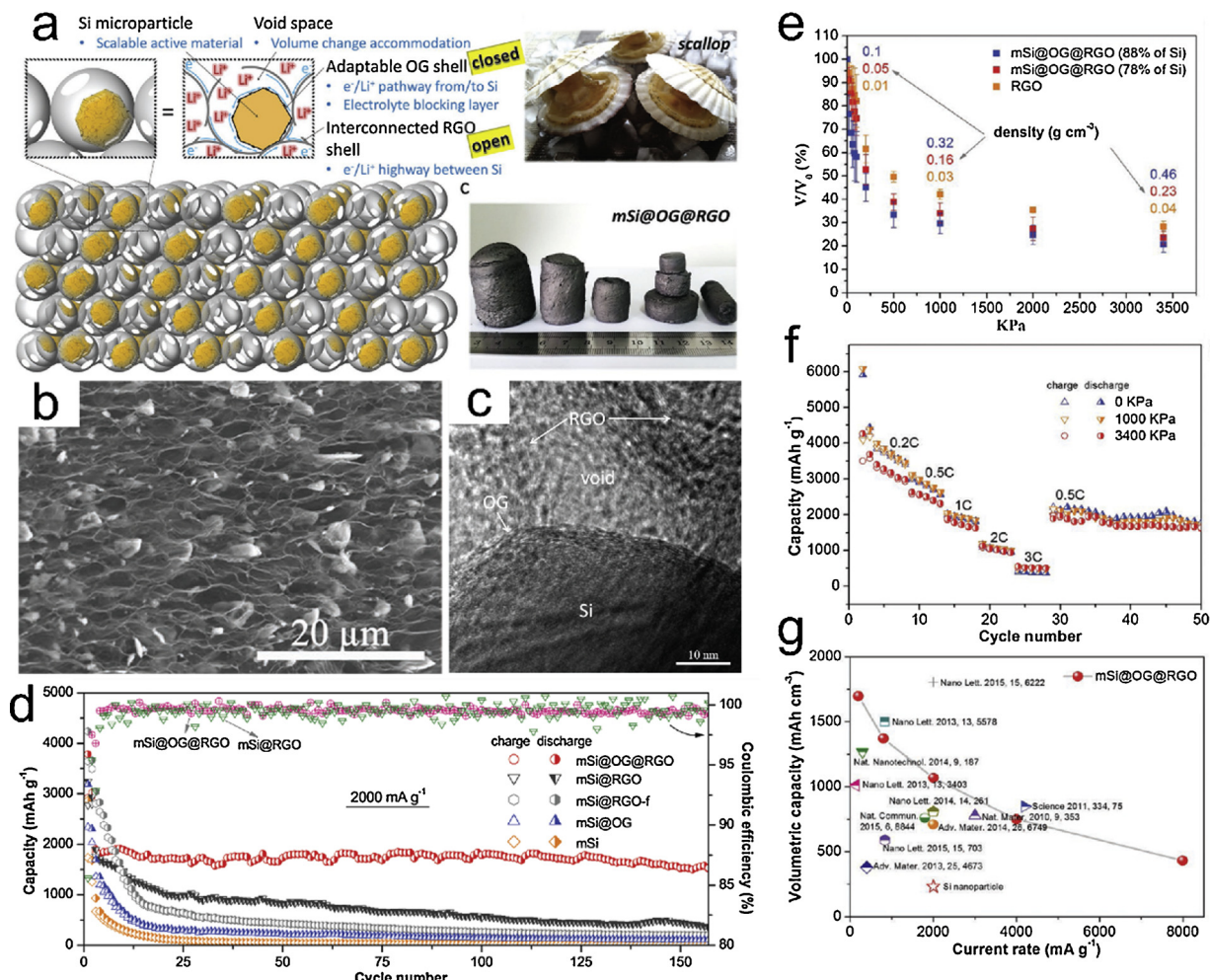


**Fig. 21.** (a) Fabrication and electrode design. (b) SEM image. (c) TEM image. (d) Cycling performance. (e) Electrode density versus pressing pressure plots for mSi@OG@rGO with different silicon contents as annotated. (f) Rate capabilities. (g) Volumetric capacity comparing with representative reported Si anodes. Reproduced from [144] Copyright 2018, Wiley-VCH.

containing porous silicon spheres and graphene shells. Ma et al. also demonstrated novel mesoporous Si@C microspheres with similar concept as anode materials for LIBs [150]. The mesopores could effectively buffer the volume expansion/shrinkage of Si nanoparticles during Li ion insertion/extraction, which achieved excellent electrochemical performance and cycle stability when used as an anode material for LIBs. Besides, Liu et al. described the construction of three-dimensional (3D) porous silicon-based anode materials from natural reed leaves by calcination and magnesiothermic reduction [151]. The thus-obtained 3D hierarchical architecture anode materials showed a remarkable Li-ion storage performance in terms of specific capacity, cycling stability, and rate capability, which was attributed to the interconnected porosity and the reductive treatment to an inside carbon coating.

Recently, Luo et al. prepared the tin-core/carbon-sheath coaxial nanocables on graphene sheets via a simple CVD process by using rGO-SnO<sub>2</sub> hybrid material as an efficient scaffold (Fig. 25) [152]. In the thus-obtained scaffold with uniform diameter and high aspect ratio, the constructed interconnectivity of these discrete nanocables through the underlying graphene matrices greatly facilitated electron transfer during charge/discharge cycling process, resulting in high reversible specific capacity and remarkable high-rate capability. Besides, Luo et al. prepared a sandwich structure of graphene-confined tin nanosheets (namely, G/Sn/G) [153], in which, the sheet-like nanostructuring of tin phase helped alleviate the material pulverization originated from the volume change of Sn during Li-Sn alloying-dealloying

reactions. Meanwhile, graphene covers at both sides of Sn nanosheets prevented the adjacent Sn nanosheets from coalescing together and more importantly, created efficient dual channels for fast transport of both electrons and lithium ions in view of their surface-to-surface contact with both sides of Sn nanosheets. Consequently, such sp<sup>2</sup>-C dominant carbon materials effectively help improve the tin-based anode with higher reversible capacity as well as superior cycling performance (4590 mA h g<sup>-1</sup> after the 60th cycle).

Furthermore, our group also described a novel contact mode between MoS<sub>2</sub> and graphene, where graphene rolls up into a hollow nanotube form and thin MoS<sub>2</sub> nanosheets are uniformly standing on the inner surface of nanotubes (Fig. 26) [154]. In such an electrode architecture design, the interconnection of graphene-based hollow tubes formed a strong self-supporting skeleton framework and provided efficient transport pathways for both electrons and lithium ions throughout the whole electrode and the nanosized and uniform dispersion of the MoS<sub>2</sub> nanosheets further accelerated lithium ion diffusion due to the shortened diffusion lengths. In the meantime, the unique side-to-surface contact mode between MoS<sub>2</sub> nanosheets and graphene sheets avoided the aggregation of the active materials and allowed for a dominance of 3–5 layers of MoS<sub>2</sub> nanosheets even when the content of MoS<sub>2</sub> was up to 90%. Consequently, the mechanically robust, free-standing network established by this sp<sup>2</sup>-C dominant carbon material exhibited a remarkably high specific capacity up to 1150 mA h g<sup>-1</sup> at 0.5 A g<sup>-1</sup>, superior rate capability (a capacity of 700 mA h g<sup>-1</sup> even at

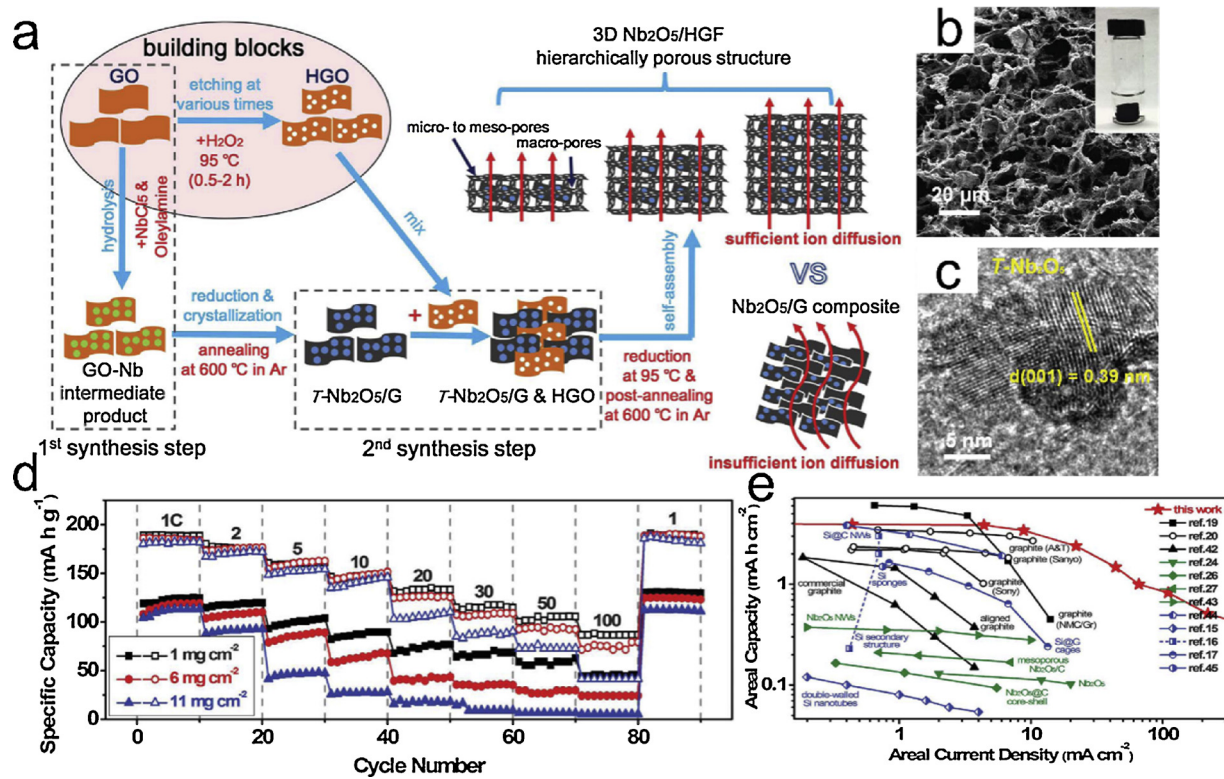


**Fig. 22.** (a) Fabrication process and electrode design. (b) SEM image. (c) TEM image. (d) Rate capabilities at different mass loadings of the Nb<sub>2</sub>O<sub>5</sub>/HGF. (e) Areal capacities of Nb<sub>2</sub>O<sub>5</sub>/HGF-2.0 electrode comparing with various commercial and research anodes. Reproduced from [145] Copyright 2017, American Association for the Advancement of Science.

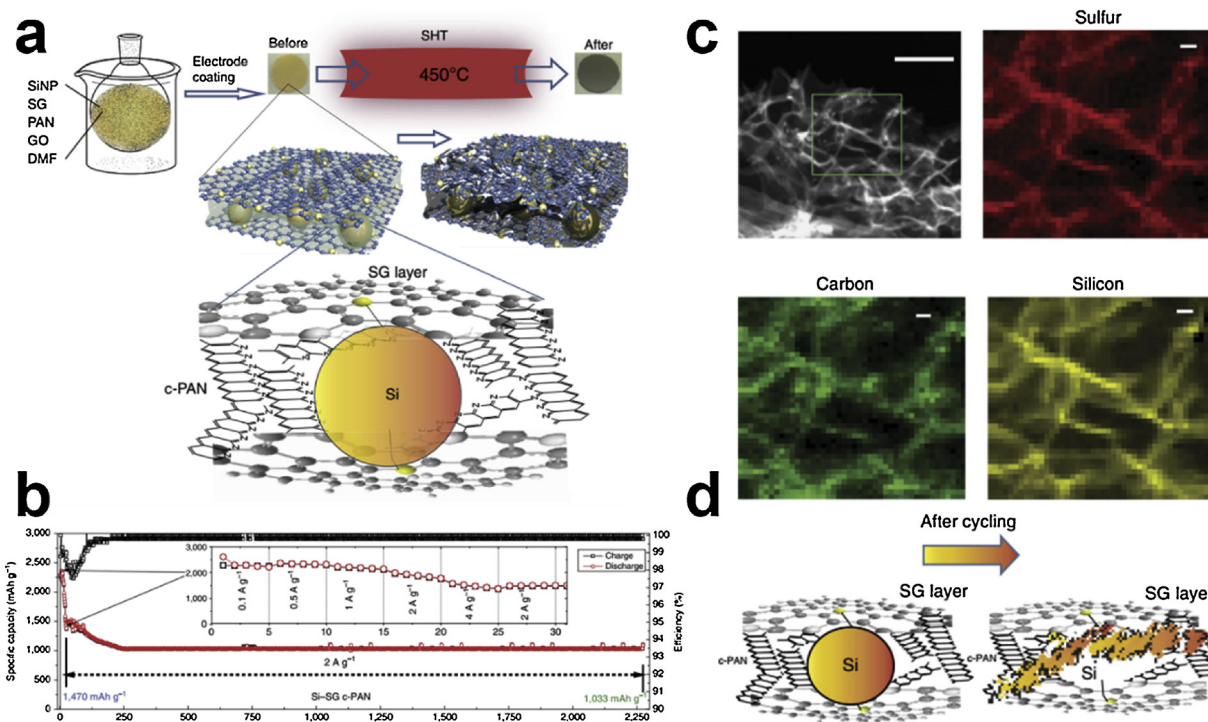


**Fig. 23.** (a) Synthetic process. (b) Cycling performance of SG-Si anode. (c) Characterization of SG-Si electrode material after cycling. (d) Schematic plot of the structure change in the electrode before and after cycling. Reproduced from [146] Copyright 2015, Nature Publishing Group.

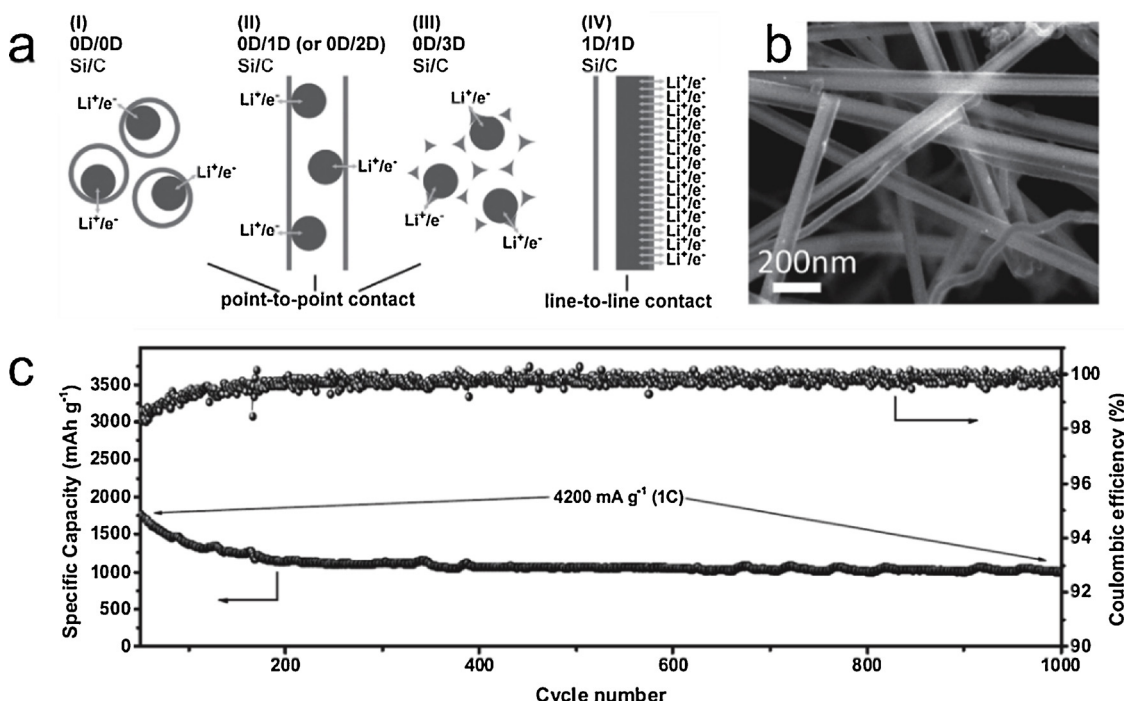


**Fig. 24.** (a) Scheme showing electron and ion transport channels, (I) 0D/0D, (II) 0D/1D (or 0D/2D), and (III) 0D/3D combinations. (b) SEM image. (c) Cycling performance of the SiNW-d-GT. Reproduced from [147] Copyright 2013, Wiley-VCH.

10 A g<sup>-1</sup>), and long cycle life (700 cycles with almost 100% capacity retention).

### 3.2. Applications for supercapacitors

Supercapacitors (also known as electrochemical capacitors or ultracapacitors), as a unique type of electrical energy storage devices, have recently attracted more and more attentions in the world because of

their super-fast charge discharge rate, high power capacity and low maintenance [155–157]. Several factors can significantly affect the performance of supercapacitors, including pore structure (SSA and pore size distribution (PSD)), morphology and electrical conductivity of electrode materials, intrinsic properties of electrolyte, the interface between electrode and electrolyte. In addition, operating voltage, matching condition of two electrodes and other parameters also strongly affect the performance of supercapacitors. Electrode materials

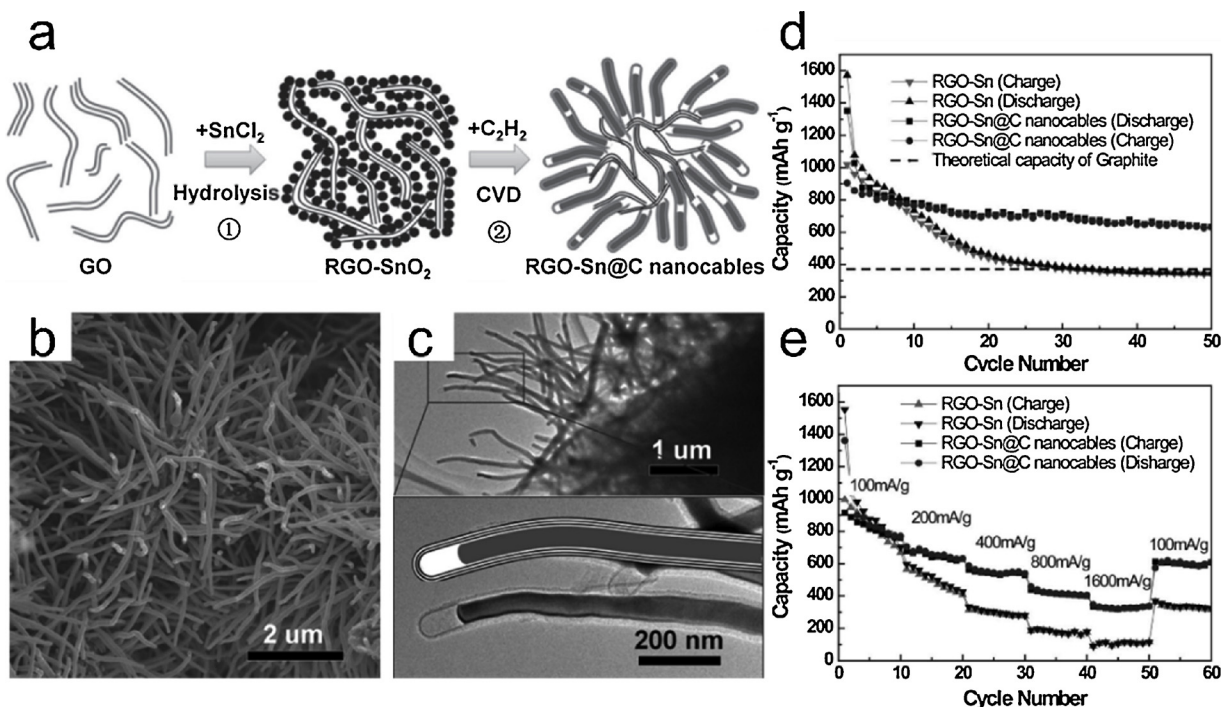


**Fig. 25.** (a) Synthetic process. (b) SEM image. (c) TEM image. (d) Cycling performance of rGO-Sn@C nanocables and contrast samples. (e) Rate performance of rGO-Sn@C nanocables and contrast samples. Reproduced from [152] Copyright 2012, Wiley-VCH.

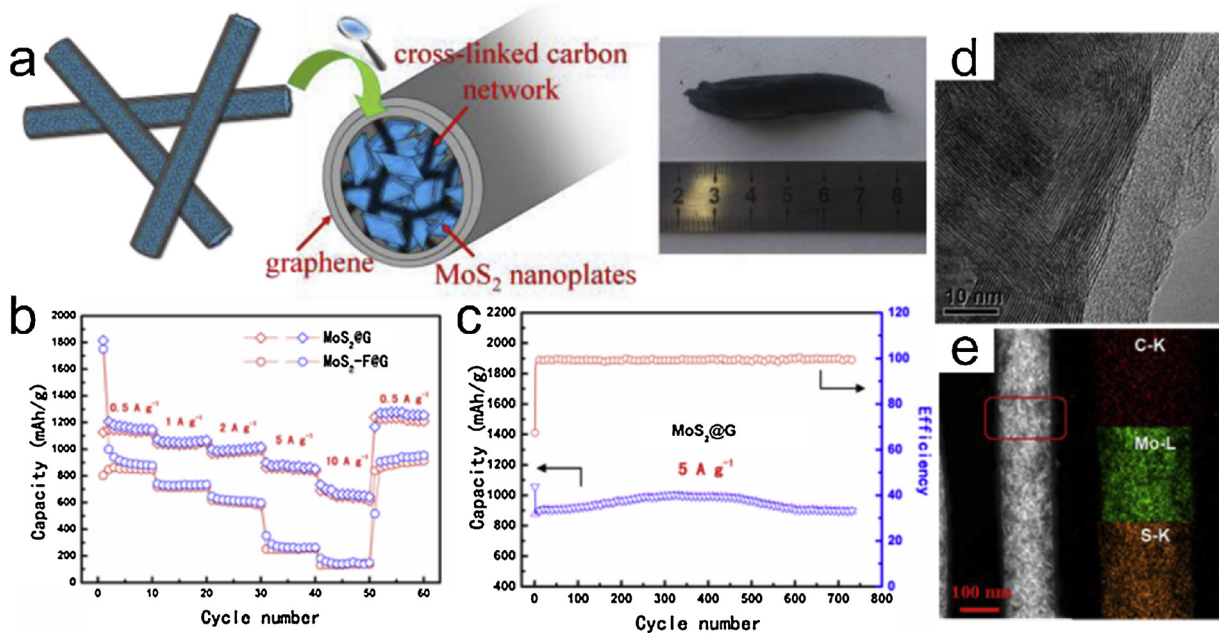


**Fig. 26.** (a) Schematic and photograph. (b) Rate performance of MoS<sub>2</sub>@G and contrast samples. (c) Cycling performance of MoS<sub>2</sub>@G. (d) TEM image. (e) The elements mapping for the area marked in image. Reproduced from [154] Copyright 2014, Royal Society of Chemistry.

are usually considered to play the most important role in supercapacitors. Among all kinds of electrode materials, carbonaceous materials are the most widely used materials. On this basis, over 80% of commercial supercapacitors have been prepared [158–160]. In general, supercapacitors with pure carbon electrode materials are called electric double layer (EDL) capacitors [161,162]. The mechanism is based on pure electrostatic attraction between the charged surfaces of ions and electrodes. However, the capacitance (or energy density) of the EDL capacitor is still far from satisfactory, which is also a disadvantage of all commercially available supercapacitors, especially in comparison with the frequently used two batteries with higher energy density [163–166]. In this respect, many methods have been put forward to overcome this problem, and remarkable progress has been made in improving the energy density of the device by optimizing the structure of carbon electrode [167–173], introducing the pseudopotential (rapid redox reaction) [174–176], and designing advanced device [177,178].

Benefiting from its unique topological structure and extraordinary chemical and physical properties, sp<sup>2</sup>-C dominant carbonaceous materials have provided exciting solutions to the limitations and challenges related to these electrode materials for SCs. In principle, sp<sup>2</sup>-C dominant carbonaceous materials allow for fundamentally enhanced performance over serving as electrode materials with optimized structure from the viewpoint of the material structure design, as a material support to introduce pseudocapacitive materials from the viewpoint of the electrode design, and/or as an electrode framework to construct advanced device from the viewpoint of the device design. We thus overview the recent experimental advances reported on supercapacitors that are indexed by the key role of sp<sup>2</sup>-C dominant carbonaceous materials.

### 3.2.1. Electrode materials

Heteroatom effect (HAE) and micropore effect (MPE) have attracted more attention in the past few years to improve the capacitance of supercapacitors. For instance, the presence of quaternary nitrogen are demonstrated to be advantageous to the conductivity of the materials, which acts an important role in the supercapacitor performance [179–186]. Furthermore, the introduction of nitrogen into carbonaceous electrode can tune the electron distribution of the materials, which can further improve the wettability between electrolytes and electrode

materials, resulting in the significant increase of active surface area accessible to the electrolyte. It is worth noting that in addition to nitrogen doping, other heteroatoms, such as oxygen (O), boron (B), phosphorus (P), are illustrated as well to be significantly advantageous to the enhancement of the supercapacitor performance. However, the underlying mechanism of the heteroatom-enhanced supercapacitance still seems to be elucidated. A reasonable strategy to more deeply study these effects is to construct model structures consisting of defined heteroatoms and/or PSD, which will be beneficial for a better understanding of the HAE and/or MPE, and consequently to enhance the performance of the supercapacitors [187,188]. The development of microporous polymer networks (MPNs) provides a great opportunity for chemically constructing such a material [189–191].

Our group have successfully developed a series of nitrogen-contained micropore-dominant structures, PTFs through the structural evolution of a 2D microporous covalent triazine-based framework (m-CTF) [60]. The PTFs feature predictable and controllable nitrogen doping and pore structures, serving as a great model-like system to more deeply understand the heteroatom effect (HAE) and micropore effect (MPE) in high-voltage ionic liquid-based supercapacitors, which is extremely important for developing high-performance supercapacitors. As shown in Fig. 27, experimental investigations disclose that the HAE is extremely significant to the supercapacitors, which reflects the changes of chemical composition and surface functionality during the structural evolution of m-CTF, and it has great influence to the relative permittivity ( $\epsilon$ ) of the electrode materials. Although the MPE is not that obvious as the HAE in this model-like system, the excellent electrochemical performance of the micropore-dominant electrode, PTF-700, suggests that the micropore-dominant materials indeed have great potential in ionic liquid-based supercapacitors. Considering that the energy density of a supercapacitor is also limited by the nominal voltage and based on recent reports, the electrolyte used here can also be applied over 3 V. Consequently, a supercapacitor based on PTF-700 was further tested with a voltage increased to 3.5 V, and showed the excellent supercapacitor performances, where the highest energy density and power density were 62.7 Wh kg<sup>-1</sup> and 8750 W kg<sup>-1</sup>, respectively. In addition, the rational design of electrode structures via bottom-up strategies developed in this work opens up a new avenue to deeply understand the electrochemical mechanisms in energy storage

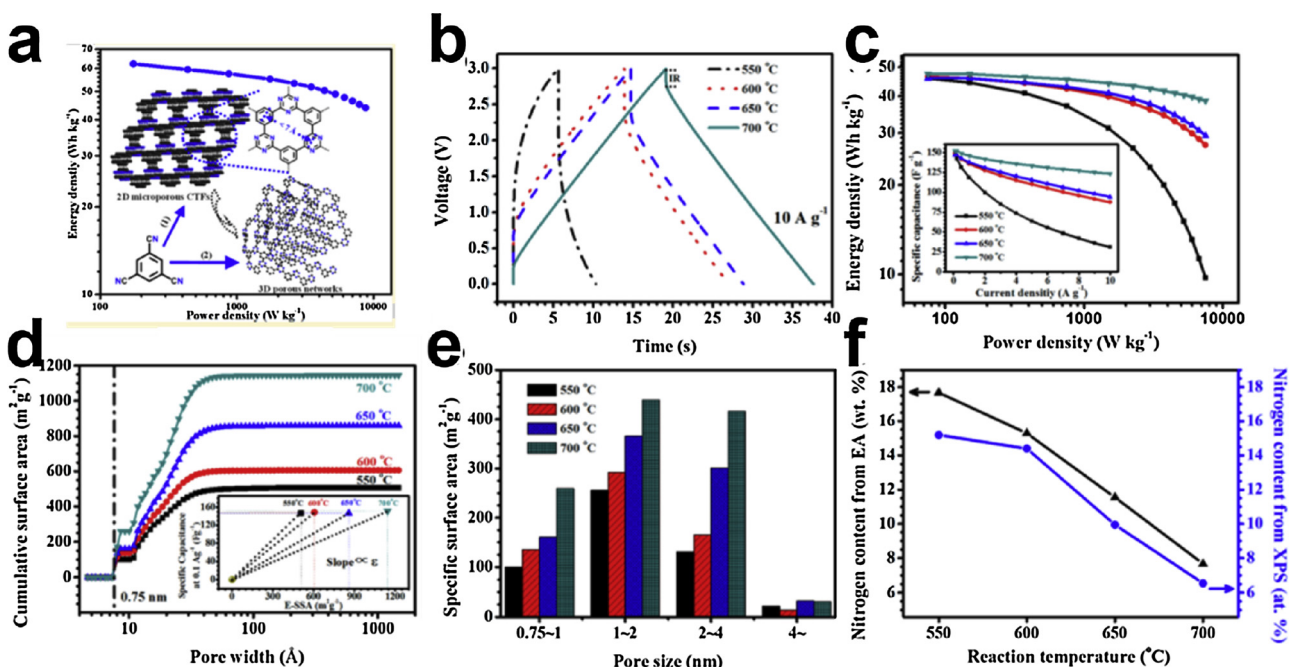


**Fig. 27.** Structural evolution of 2D microporous covalent triazine-based framework toward the study of high-performance supercapacitors. Reproduced from [60]. Copyright 2015, American Chemical Society.

devices as well as better design high performance electrode materials for practical applications.

Engineering the morphology of carbon materials and their pore channel structures is another vital factor to improve the performance by providing better electrolyte permeability, ion transport/diffusion, electron-transfer path, and higher charge-induced ion-adsorbing surface area. A new type of carbon nanofiber with multi-layer nanotube structure was successfully prepared by the effective combination of microemulsion, electrospinning and thermochemical treatment technology [192]. The changes in the amount of PMMA in the precursor are important for regulating the structure of the multi-layer nanotube structure of the final carbon nanofibers, improving the specific surface of the fiber, optimizing the content of the official energy group in the fiber, and improving the order degree of the microcrystals in the fiber. The new carbon nanofibers with multi-layer nanotube structures exhibit high specific capacity, good multiplier performance and excellent cyclic stability (specific performance data) as the electrode materials of supercapacitors. Under the optimal conditions, the capacity retention rate of the supercapacitor is 80% at 0.1 A g<sup>-1</sup> to 10 A g<sup>-1</sup>, and is circulated 10,000 times at the current density of 10 A g<sup>-1</sup>, and the specific capacity can be maintained at 357 F g<sup>-1</sup>. The results show that the excellent electrochemical properties of carbon nanofibers are closely related to their chemical and physical structures. In addition to the multi-layer, large area, and interconnected channel structures on the nanoscale, the presence of chemical functionalities caused by multiple components also has an important effect on the electrochemical performance of the final carbon nanofibers. Very recently, based on this hollow fiber structure, He et al. developed a continuous and efficient method for scalably preparing carbon nanofiber beam electrode materials [193]. The fiber-shaped flexible supercapacitor constructed with this electrode material not only has high specific capacitance and high ratio, but also possesses excellent flexibility, and has no capacitance loss in bending to 180°.

Another concern remains challenging that the volumetric performance is far from satisfactory due to the low intrinsic and packing densities of nanomaterials and nanostructured materials. This raises the materials design challenge towards high volumetric energy electrodes where a few criteria are required: high volumetric capacitance

materials, high electron conductivity and unimpeded ion transport channels for performance scalability. Tao et al. reported that capillary compression of a networked graphene sheets leads to a high-density solid (e.g., 1.58 g cm<sup>-3</sup>), in which the evaporation of water exerted "tension" on the graphene sheet and resulted in the contraction of the 3D network [194]. Ions between water and graphene sheets were found to be highly dense but porous graphene monolith (HPGM) using tightly interconnected graphene sheets. Two products after capillary drying and freeze drying process, respectively, have similar specific surface area and thus supercapacitor mass-based capacitance, but their volume-based capacitance is in a huge gap due to the completely different density. This dense yet porous graphene monolith is modable and has a good electron and ion conductivity, thus provides a high capacity capacitance of 376 F cm<sup>-3</sup> for supercapacitors with water electrolyte [195,196]. This study demonstrated that the spatial interconnection with the proper elimination of solvents can lead to highly porous carbon with finely tuning density, and more importantly, it provides a new insight into graphene-based materials and their real opportunities for the practical applications in energy storage [197,198].

Battery configuration is also important for the volume performance of electrochemical energy storage (EES) devices, but few breakthroughs have been made. In recent years, advanced technologies made by micro EES devices make it possible to achieve high capacity performance due to high volume performance in micro/nanoscale systems. For example, miniature supercapacitors with short ion diffusion paths are considered to be highly competitive candidates for the integration of various microelectromechanical systems (MEMS) because of their high performance and particularly small size [199–202]. In order to fabricate high performance miniature supercapacitors, great efforts have been made in developing carbon electrodes for micro super capacitors [203–207]. Mullen et al. reported an efficient layer by layer assembly (LBL) assembly and intercalation protocol for ultrathin, ultrathin, heteroatom-doped graphene films. The micro supercapacitor using the Co-doped graphene film can provide high capacity capacitance of 488 F cm<sup>-3</sup>, and has excellent multiplying performance, reaching 2000 V s<sup>-1</sup>. Monolithic carbon films produced by well controlled etching can also be used as electrodes for micro supercapacitors [193]. Wu and his team recently have reported a series of important work on the carbonaceous

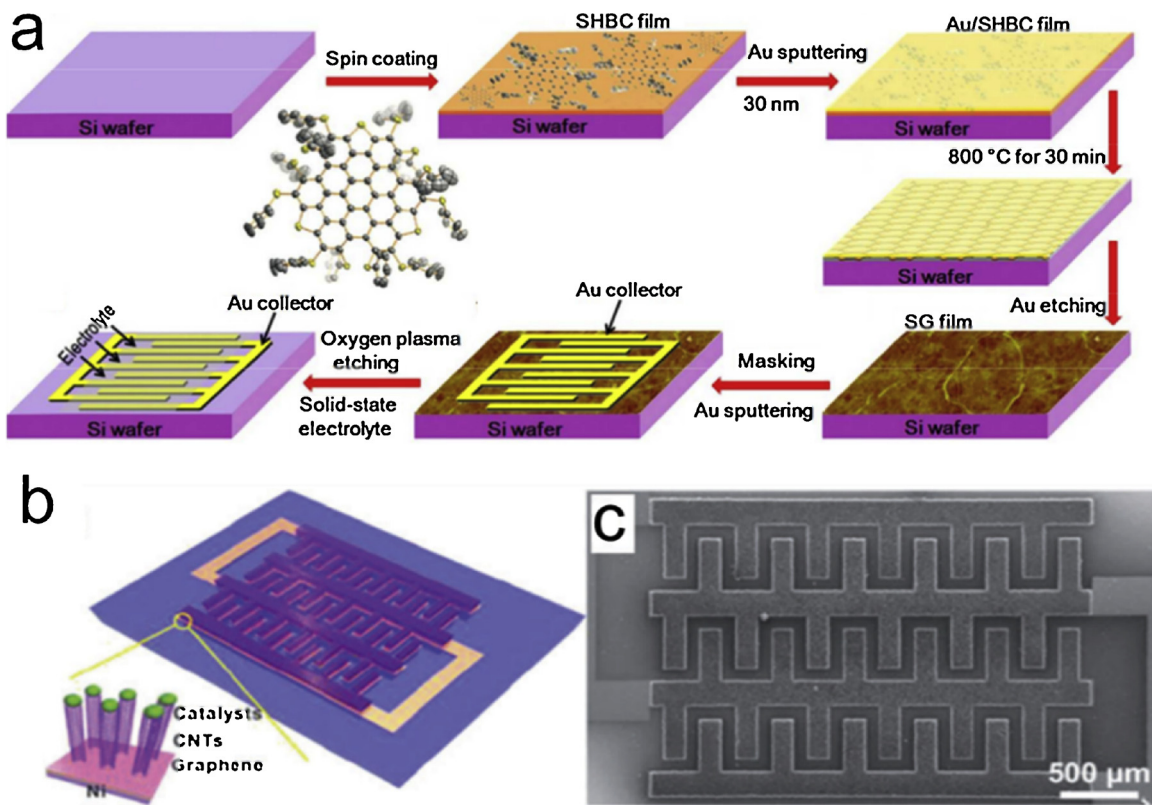


**Fig. 28.** (a) Schematic illustration of SHBC-derived SG films for planar MSCs on a Si/SiO<sub>2</sub> wafer. (b and c) Schematic and SEM images of the G/CNTCs based microsupercapacitor. Reproduced from [209] Copyright 2013, American Chemical Society.

based micro-device [177,178,208]. For instance, a structurally-defined nanographene-derived SG film was successfully designed and fabricated, as shown in Fig. 28a [208]. Unlike the previously reported works of heteroatom (*N*)-doped graphene films, mainly by doping graphene or graphene oxide, the resulting MSCs showed unprecedented performance, including ultrahigh volumetric capacitance of 582 F cm<sup>-3</sup>, ultrafast frequency response with a time constant of only 0.26 ms, and ultrahigh power density of ~1191 W cm<sup>-3</sup>.

Gogotsi group prepared a carbide-derived carbon membrane with a volumetric capacitance of 160 F cm<sup>-3</sup> in 1 M H<sub>2</sub>SO<sub>4</sub> [188]. This strategy provides a framework for integrating high-performance micro EES devices into a range of devices. Great progress has also been made in the preparation of high performance carbon-based micro super capacitors by Lin group [209,210]. 3D based graphene/carbon nanotube carpet (G/CNTs) hybrid materials were used to prepare supercapacitors and exhibited good electrochemical properties. The unique seamless transition structure and water erosion significantly increase the conductivity and capacity, leading to the high volumetric energy density of the 2.42 mW h cm<sup>-3</sup> with the ionic liquid electrolyte, and a high power capacity at 400 V s<sup>-1</sup>, and a high power density of 115 W cm<sup>-3</sup>. They also developed a single step and extensible porous graphene (Fig. 28 b and c) from a commercial polymer through a laser irradiation, which allows the volume of an electronic and energy storage device to be rolled into a volume to make polymer be written. The related research of micro EES devices shows that the volume performance is the most important standard, so it is very challenging to make the electrode materials used in these microdevices or flexible devices because of the high standard of these electrodes. More advanced technology is needed to promote the practical application of microdevices with high volume performance.

### 3.2.2. Conductive network

The structure of the SC electrode, which is different from the

traditional electrode, is highly dependent on the insulating binder and the conductive additive. It is a powerful strategy for the development of high performance supercapacitor electrodes and devices to construct a series of self-supporting sp<sup>2</sup>-C dominant carbonaceous materials and a variety of electrochemical active electrode materials [211]. This hybrid method can form a 3D continuous conductive network, which is conducive to the utilization of embedded active materials. The general method of hybridization is to filter graphene oxide sheets and nanostructured active materials by vacuum filtration and then reduced to mixed films, in which the active nanostructures are sandwiched between reduced graphene oxide plates [212–216]. For example, Wu and others prepared a mixed film of rGO sheet and polyaniline (PANI) nanofibers by vacuum filtration, in which polyaniline nanofibers were well sandwiched between reduced graphene oxide slices (Fig. 29a) [217]. The rGO/PANI hybrid membrane prepared by this method has good mechanical stability, and maintains high flexibility. It can bend into large angles or form all kinds of required structures. When directly used as an electrode, the hybrid membrane can also provide a large capacitance (210 F g<sup>-1</sup>) in the case of a discharge density of 0.3 g<sup>-1</sup>, even in the absence of an insulating binder and a low capacitance conductive additive, which greatly improves the electrochemical stability and multiplicability. The impressive performance is mainly attributed to the conductivity of graphene enhanced electrodes, which is favorable to the redox reaction of sandwich PANI nanofibers. In another study, Yan et al. put forward an improved hybridization strategy to prepare a flexible and conductive MXene/graphene hybrid film electrode (MXene/rGO) by combining the filtration process with the electrostatic self-assembly (Fig. 29b) [218]. RGO nanosheets were inserted into the MXene layer based on electrostatic assembly. This inserted rGO sheet is considered to act as a conductive spacer, effectively preventing the self-weight accumulation of MXene at nanoscale, resulting in an increased interlayer spacing, accelerated ion transport, and more accessible electroactive sites. This resultant free-standing hybrid-film

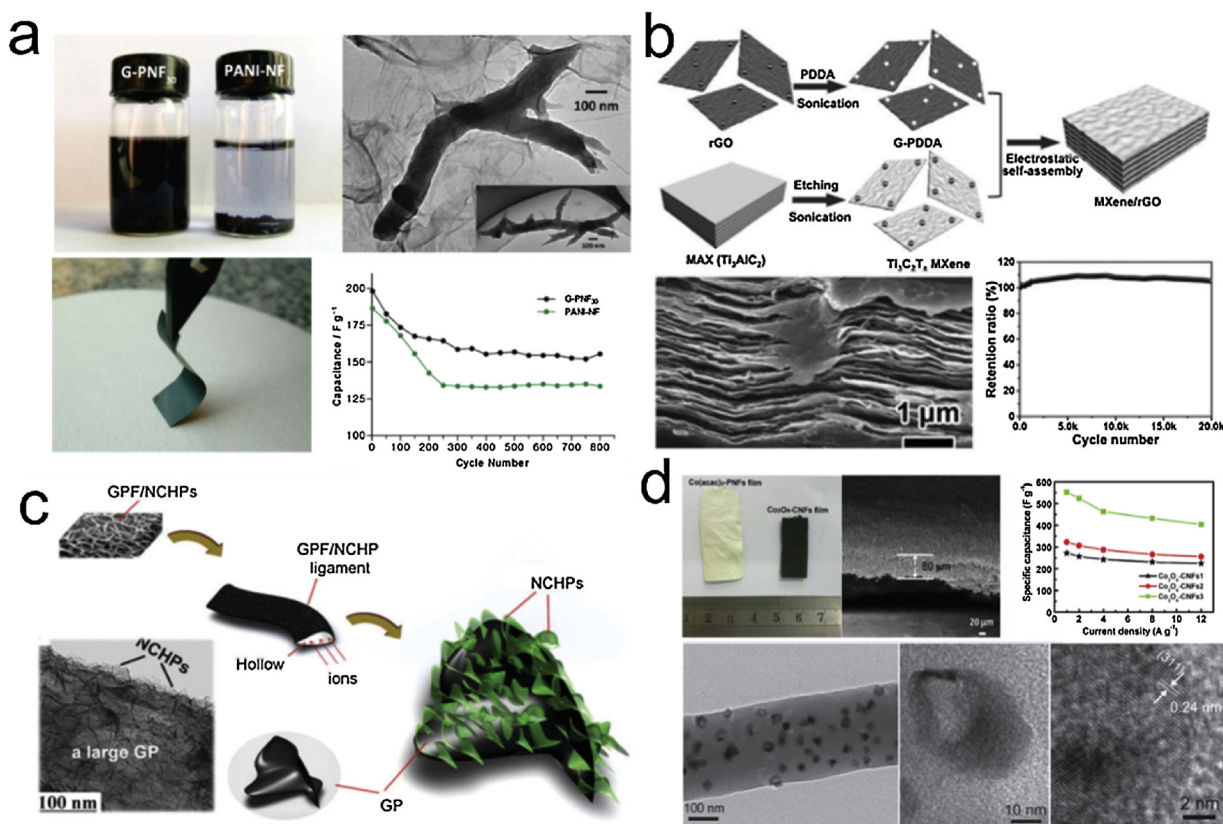


**Fig. 29.** (a) Digital photograph, TEM image, and cyclic performance of G-PNF. Reproduced from [217] Copyright 2010, American Chemical Society. (b) Fabrication process, cross-sectional SEM image, and cyclic performance of the MXene/rGO. Reproduced from [218] Copyright 2017, Wiley-VCH. (c) Fabrication process and TEM image of the GPF/NCHP. Reproduced from [225] Copyright 2016, Wiley-VCH. (d) Photo graphs, cross-sectional SEM image, TEM image and rate performance of Co<sub>3</sub>O<sub>4</sub>-CNFs. Reproduced from [231] Copyright 2016, Royal Society of Chemistry.

**Table 2**

Energy storage applications for sp<sup>2</sup> C-dominant carbon materials and related examples.

Applications	Critical technique	Examples
Lithium ion batteries	Anode materials	N-Doped holey graphene (N-hG) anode [140] N-enriched carbon/carbon nanotube composite (NEC/CNT) [62]
	Buffer media & conductive network	graphene-based porous nitrogen-doped carbon (PNCs@Gr) [142] graphene-based self-supporting binder-free electrode configuration [143] scalloped-inspired mSi@OG@RGO [144] three-dimensional, hierarchically-porous, free-standing network electrode (Nb <sub>2</sub> O <sub>5</sub> /HGF) [145] graphene-confined tin nanosheets [153]
Supercapacitors	Electrode materials	chemically constructing of electrode materials from microporous polymer networks [189,191] microporous covalent triazine-based framework (m-CTF) [60]
	Conductive network	carbon nanofiber beam electrode materials [193] mixed film of RGO sheet and polyaniline nanofibers [217] MXene/graphene hybrid film [218] carbon nanofibers (CNFs) embedded with Co <sub>3</sub> O <sub>4</sub> hollow nanoparticles (NPs) [231]

electrode showed a high capacity capacitance of 1040  $\mu\text{F cm}^{-2}$  at a scanning rate of 2 mV s<sup>-1</sup>, an impressive rate capability under 1 V s<sup>-1</sup>, a 61% capacitance retention, and a long cycle life with almost no capacitive attenuation after 20,000 cycles. In addition, the fabricated binder's symmetric supercapacitors show an ultra-high volumetric energy density of 32.6 W h L<sup>-1</sup>. As a substitute, the self-supported porous graphene frame can be firstly constructed by vacuum filtration in the presence of an ideal template or spacer, in which the nanosized active material is mixed or deposited *in situ*.

The flexible and capacitive properties of the binders in the flexible supercapacitor applications have been realized [219–224]. In recent years, as shown in Fig. 29c, Xiong et al. has designed and manufactured a practical pseudololed electroluminescent device by two steps, and designed an attractive self-supporting layered electrode structure

composed of Ni-Co hydroxide petals (NCHPS) [225]. In the mixed electrode structure, the vertically-standing graphene petals interconnected in GPF not only provide a mechanically-solid and conductive network on the entire electrode, which are used for

the pseudo-capacitive metal hydroxide, but also significantly increase the ion-accessibility of the surface area, thereby promoting fast Faraday charging and discharging capability and cyclic stability of NFCHP. As a result, the volumetric capacitance of the GPF/NCHP hybrid electrode is as high as 765 F cm<sup>-3</sup>, the area capacitance and high magnification ability of 15.3 F cm<sup>-2</sup>. In addition, the asymmetric solid-state supercapacitor, prepared with GPF/NCHP as the positive pole, shows excellent energy and power density, the maximum average energy density is about 10 mW h cm<sup>-3</sup>, the maximum power density is about 3 W cm<sup>-3</sup>, and the high rate capacity (capacitance RE). At

100 mA cm<sup>-2</sup>, the tension is about 60%, and the excellent long-term cycle stability (full capacitance remains over 15 000 cycles) demonstrates the potential of graphene hybrid electrodes for high-performance SCs.

Since the first exploration by Formhals, electrospinning, as an industry-viable and versatile technique, has gained substantial attention in both academic research and industrial applications [226–231]. Flexible and porous films are prepared from electrospun carbon nanofibers (CNFs) embedded with Co<sub>3</sub>O<sub>4</sub> hollow nanoparticles (NPs) and are directly applied as self-supported electrodes for high-performance electrochemical capacitors (Fig. 29d). Uniform Co<sub>3</sub>O<sub>4</sub> hollow NPs are well dispersed and/or embedded into each CNF with desirable electrical conductivity. These Co<sub>3</sub>O<sub>4</sub>-CNFs intercross each other and form 3D hierarchical porous hybrid films. Benefiting from intriguing structural features, the unique binder-free Co<sub>3</sub>O<sub>4</sub> hollow NPs/CNF hybrid film electrodes exhibit high specific capacitance (SC), excellent rate capability and cycling stability. As a typical example, a flexible hybrid film with loading of 35.9 wt% Co<sub>3</sub>O<sub>4</sub> delivers a specific capacitance of 556 F g<sup>-1</sup> at a current density of 1 A g<sup>-1</sup>, and 403 F g<sup>-1</sup> even at a very high current density of 12 A g<sup>-1</sup>. Remarkably, there is almost no capacitance decay after the continuous charge/discharge cycling for 2000 cycles at 4 A g<sup>-1</sup>.

Table 2 summarizes the energy storage applications for sp<sup>2</sup>-C dominant carbon materials and related typical examples that were mentioned above.

#### 4. Sp<sup>2</sup>-C dominant carbon materials for energy conversion applications

Sp<sup>2</sup>-C dominant carbon materials have obtained great attention for a broad range of underlying applications, due to not only their chemical tenability, conjugated network, but also topological structure, abundant electroactive sites and excellent electrochemical properties. In this section, we focus on potential applications of sp<sup>2</sup>-C dominant carbon materials in energy conversion applications, including some important electrochemical reactions and solar cell.

##### 4.1. Applications for electrocatalysis

There are three simple but vital electrochemical reactions, oxygen reduction reaction (ORR), oxygen evolution reaction (OER) and hydrogen evolution reaction (HER), involved in green and renewable energy technologies, such as fuel cells, metal-air batteries and water splitting [23,232,233]. Generally, four proton-electron transfer of the ORR is desirable for fuel cells, while enabling a two proton-electron pathway can be attractive for the production of hydrogen peroxide. During OER process, molecular oxygen will be produced via several proton/electron coupled procedures, which is considered to be the key reaction for all the above systems to carry out their reversible process along with ORR and/or HER. To improve the activity of an electrocatalyst system in these electrochemical reactions, two general strategies can be adopted: (i) increasing the number of active sites and (ii) improving the intrinsic activity of each active site. Recently, sp<sup>2</sup>-C dominant carbon materials also present excellent electrocatalytic performance for CO<sub>2</sub> reduction [234,235]. Among these advanced technologies, sp<sup>2</sup>-C dominant carbon materials can act as functional components, such as catalytic active materials and catalyst supports.

###### 4.1.1. Catalytic active materials

The cathodic ORR plays a key role in expediting the energy conversion efficiency of a fuel cell. The commonly used platinum catalyst makes up more than half of the cost of a fuel cell stack yet suffers from poor durability, methanol crossover and CO poisoning, as well as high cost and limited reserve, thus inhibiting the commercial applications of fuel cells [236]. Intensive research efforts have been devoted to developing nonprecious metal catalysts, among which sp<sup>2</sup>-C dominant

carbon materials are powerful alternatives to reduce or replace platinum catalyst [237,238].

In 2009, vertically aligned nitrogen-containing carbon nanotubes (VA-NCNTs) were synthesized by CVD (Fig. 30 a). The VA-NCNTs can act as an excellent metal-free electrocatalyst with higher electrocatalytic performance, long-term operation durability, and tolerance to crossover effect than Pt/C in alkaline fuel cells (Fig. 30 b-d) [239].

Combining experimental data with quantum mechanics calculations based on B3LYP hybrid density functional theory, the enhanced catalytic activity of VA-NCNTs for the ORR is derived from the stronger electronic affinity of nitrogen atom, which imparts a high positive charge density to adjacent carbon atoms (Fig. 30 e). The nitrogen-induced charge delocalization could also change the chemisorption mode of O<sub>2</sub> from the usual end-on adsorption (Pauling model) at the nitrogen-free CNT (CCNT) surface (Fig. 30 f, top) to a side-on adsorption (Yeager model) onto the NCNT electrodes (Fig. 30 f, bottom). The parallel diatomic adsorption could effectively weaken the O–O bonding, improving ORR performance at the VA-NCNTs electrodes. Subsequently, boron-doped CNTs were developed, in which boron-doping breaks the electroneutrality of CNTs and effectively utilizes carbon  $\pi$  electrons [240].

Heteroatom-doped graphene is another important metal-free catalyst for the ORR. Nitrogen-doped graphene synthesized by CVD was demonstrated to be an effective metal-free electrocatalyst for the ORR [241]. Henceforth, various heteroatom-doped graphene were reported. Edge-selectively functionalized graphene nanoplatelets (EFGnP) with different functional groups have been prepared by a simple and large-scale ball milling method (Fig. 31 a) [242]. Depending on the presence of different reactants, hydrogen- (HGNP), carboxylic acid- (CGNP), sulfonic acid- (SGNP), and carboxylic acid/sulfonic acid- (CSGNP) functionalized GnP have been synthesized.

The kinetic contribution related to oxygen diffusion by edge polar nature was demonstrated to play an important role in regulating the ORR efficiency of EFGnP. The ORR performance of EFGnP electrodes follows the order of SGNP > CSGNP > CGNP > HGNP > pristine graphite. Furthermore, edge-sulfurized graphene nanoplatelets were also prepared by ball-milling in the presence of sulfur [243]. The edge-sulfurized graphene nanoplatelets showed improved ORR performance with long-term operational stability, and tolerance to methanol crossover and CO poisoning effects compared to commercial Pt/C catalysts. Theoretical calculations, supported by experimental data, elucidated that improved ORR activity was associated with the contribution from electron spin (Fig. 31 b). Owing to the increased spin and charge densities, the oxidized edge-sulfurized graphene nanoplatelets exhibited improved ORR activity. In addition, edge-selectively halogenated graphene nanoplatelets (XGNP = ClGNP, BrGNP, IGNP) were also prepared simply by ball milling graphite with Cl<sub>2</sub>, Br<sub>2</sub>, and I<sub>2</sub>. The ORR electrocatalytic activities of XGNP follow the order of IGNP > BrGNP > ClGNP. According to density-functional theory (DFT) calculations, the larger atomic size leads to loosely bound valence electrons for enhancing charge polarization and hence facilitates the charge-transfer (Fig. 31 c). Besides, N or S-doped graphene was synthesized via thermal reaction between graphene oxide and guest gases (NH<sub>3</sub> or H<sub>2</sub>S) [244]. Pyridinic- and pyrrolic-nitrogen-doped graphene was synthesized inside the spatial-confined layered montmorillonite (MMT), serving as a quasi-closed flat nanoreactor [245].

Co-doping CNTs or graphene with different heteroatoms is an effective path to further enhance the ORR activity. Since the development of vertically aligned BCN (VA-BCN) nanotubes, boron and nitrogen co-doping have been sufficiently considered [246]. There are several works focusing on synergistic effects of co-doping with boron and nitrogen. VA-BCN nanotubes were prepared by pyrolysis of melamine diborate, a single-compound source of carbon, boron, and nitrogen for BCN nanotube growth. The VA-BCN nanotube electrode showed better electrocatalytic activity for ORR than VA-CNT, VA-BCNT and VA-NCNT, indicating that the heteroatom co-doping with B and N can

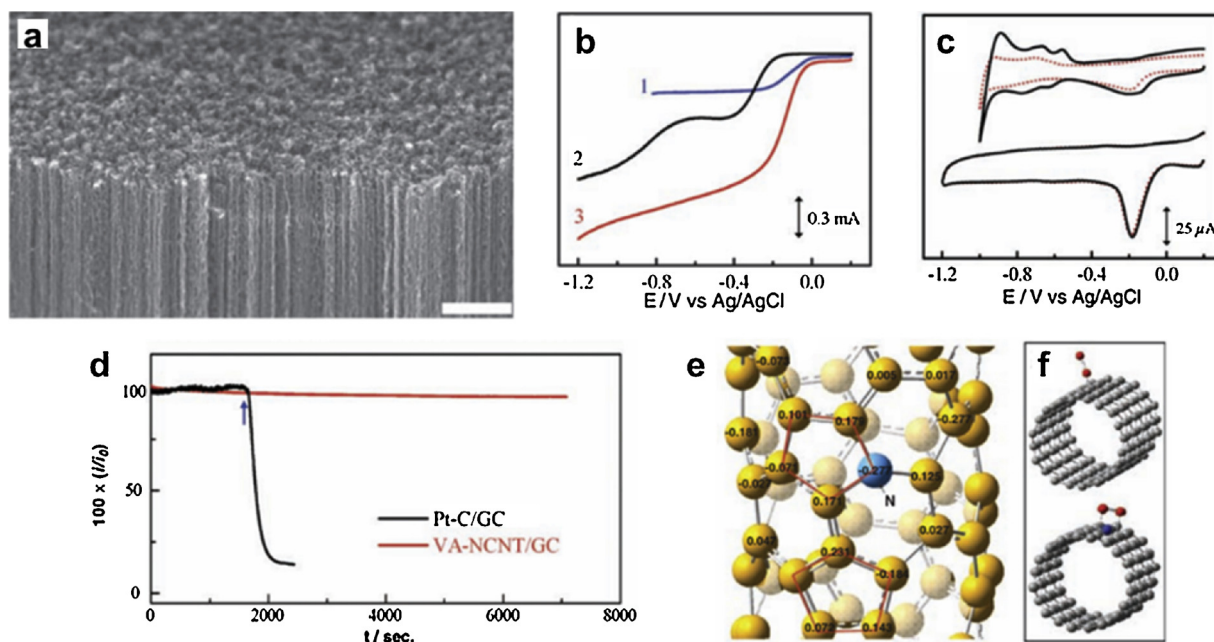


**Fig. 30.** Morphology characterization and catalytic performance of VA-NCNTs. (a) SEM image of the as-synthesized VA-NCNTs on a quartz substrate. Scale bar, 2  $\mu\text{m}$ . (b) Rotating disk electrode (RDE) voltammograms for oxygen reduction in air-saturated 0.1 M KOH at the Pt/C (curve 1), VA-CCNT (curve 2), and VA-NCNT (curve 3) electrodes. (c) Cyclic voltammograms for the ORR at the Pt/C (top) and VA-NCNT (bottom) electrodes before (solid curves) and after (dotted curves) a continuous potentiodynamic sweep for about 100,000 cycles in air-saturated 0.1 M KOH at room temperature ( $25 \pm 1^\circ\text{C}$ ). Scan rate: 100 mV s $^{-1}$ . (d) The CO poisoning effect on the  $i$ - $t$  chronoamperometric response for the Pt/C (black curve) and VA-NCNT (red line) electrodes. (e) Calculated charge density distribution for the NCNTs. (f) Schematic representations of possible adsorption modes of an oxygen molecule at the CCNTs (top) and NCNTs (bottom). Reproduced from [239] Copyright 2009, American Association for the Advancement of Science (For interpretation of the references to colour in this figure legend, the reader is referred to the web version of this article).

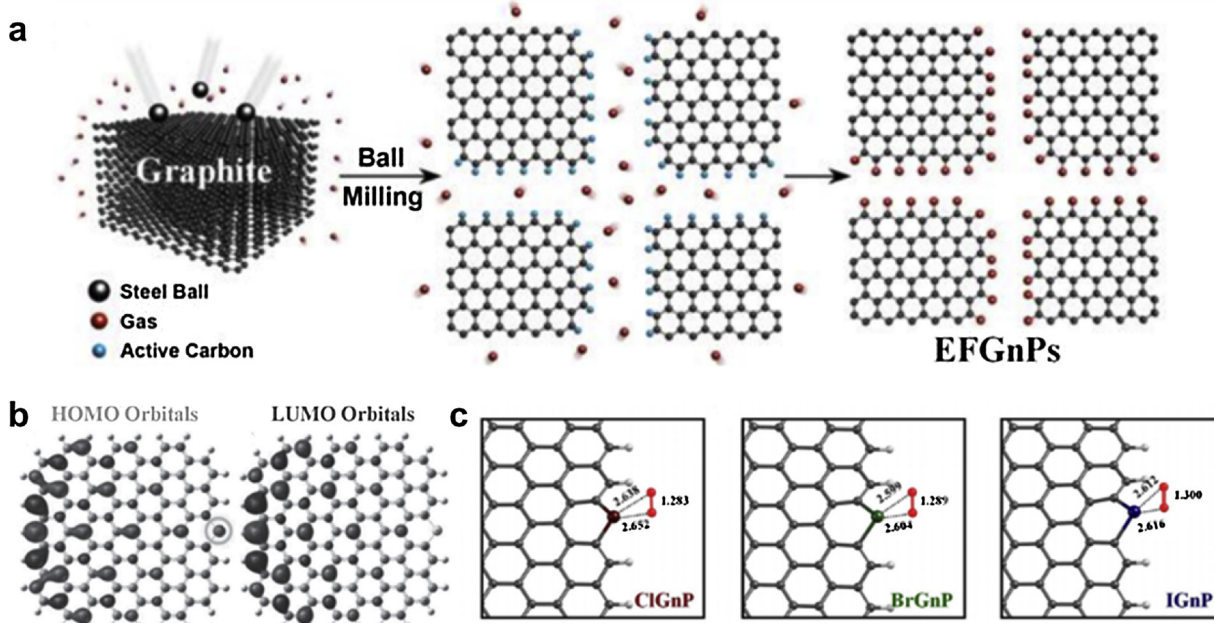


**Fig. 31.** Schematic representation of the preparation of EFGnPs through the ball milling method for ORR. (a) Schematic illustration of the mechanochemical reaction between in situ generated active carbon species and reactant gases in a sealed ball-mill crusher. The cracking of graphite by ball milling in the presence of corresponding gases and subsequent exposure to air moisture resulted in the formation of EFGnPs. The red balls stand for reactant gases such as hydrogen, carbon dioxide, sulfur trioxide, and air moisture (oxygen and moisture). Reproduced from [242] Copyright 2013, American Chemical Society. (b) Highest occupied molecular orbital (HOMO) and lowest unoccupied molecular orbital (LUMO) distributions of edge-sulfurized graphene nanoplatelets. (c) The optimized  $\text{O}_2$  adsorption geometries onto XGnP, in which halogen covalently linked to two  $\text{sp}^2$  carbons. Reproduced from [243] Copyright 2013, Wiley-VCH (For interpretation of the references to colour in this figure legend, the reader is referred to the web version of this article).

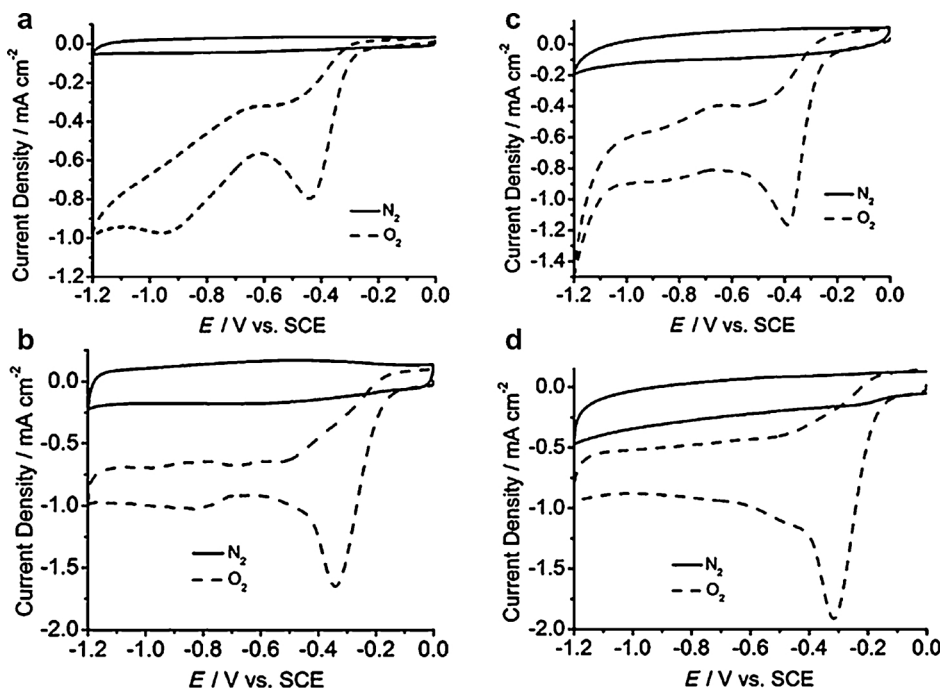


**Fig. 32.** Cyclic voltammetry curves of (a) VA-CNT, (b) VA-BCNT, (c) VA-NCNT, and (d) VA-BCN electrodes in nitrogen- and oxygen-saturated 0.1 MKOH aqueous electrolyte solutions. The scan rate was 50 mVs<sup>-1</sup>. Reproduced from [247] Copyright 2013, American Chemical Society.

effectively improve the ORR performance (Fig. 32). To systematically understanding the effect of B- and N-codoping microstructure, Zhao et al. prepared two different B and N co-doped CNTs, of which one was dominant by separated B and N and the other by bonded B and N [247]. The combination of experimental and theoretical results demonstrated that the separated case can transform CNTs into excellent ORR electrocatalysts, while the bonded one can hardly break the inertness of CNTs. When B and N atoms bonded together, the neutralization between the electron donor (N) and acceptor (B) occurred, resulting in poor ORR activity. Furthermore, BCN graphene was also reported, which was simply prepared by thermal annealing graphite oxide in the presence of boric acid and ammonia [248]. The resultant BCN graphene exhibited superior electrocatalytic activities to commercial Pt/C

electrocatalyst. The first-principles calculations revealed that energy bandgap, spin density, and charge density are dependent on the doping-level. Therefore, BCN graphene with a modest N- and B-doping level showed the best ORR electrocatalytic activity, fuel selectivity, and long-term durability. Following the case in CNTs, B- and N-co-doped graphene was prepared by a two-step doping method, which could realize the incorporation of heteroatoms at selected sites of the graphene framework [249]. Moreover, phosphorus and nitrogen co-doped vertically aligned CNT arrays [250], and nitrogen and sulfur dual-doped mesoporous graphene nanosheets [251] were also prepared and presented excellent catalytic activities.

Except for the above-mentioned heteroatom doped CNTs and graphene, monomer, polymer, or covalent organic polymers (COPs) derived sp<sup>2</sup>-C dominant carbon materials with hierarchical porous structure, good chemical stability, large surface area, and high graphitization degree also exhibit excellent electrocatalytic activities. Nitrogen-doped ordered mesoporous graphitic arrays (NOMGAs) have been prepared by the use of ordered mesoporous silica SBA-15 as a template and a nitrogen-containing aromatic dyestuff as the carbon precursor [252]. The unique characters of the resultant NOMGAs led to great electrocatalytic activity, excellent long-term stability, and tolerance to crossover effects for the ORR, even superior to the commercially available Pt/C catalyst. Due to the metal-free preparation procedure, the electrocatalytic activity can be ascribed exclusively to the incorporation of nitrogen in NOMGAs. Liu et al. have reported P-doped

graphite layers prepared by pyrolysis of toluene and triphenylphosphine (TPP), which showed high electrocatalytic activity, long-term stability, and excellent resistance to crossover effects of methanol in an alkaline medium for ORR [253]. Mesoporous nitrogen-doped carbon (meso-PoPD), possessing high SSA, hierarchically porous structure, and optimized surface functionality with the desired nitrogen doping, has been fabricated by using nitrogen-enriched aromatic polymers such as poly(o-phenylenediamine) (PoPD) and colloidal silica as precursor and template, respectively, followed by ammonia activation [254]. Benefiting from the unique structural features, meso-PoPD showed one of the best ORR activity with a half-wave potential of 0.85 V with a low loading of 0.1 mg cm<sup>-2</sup>. Furthermore, mesoporous nitrogen-doped carbon materials could also be synthesized by the carbonization of nucleobases dissolved in an all-organic ionic liquid (1-ethyl-3-methylimidazolium dicyanamide) [255].

COPs with well-defined structures, conjugated networks, various heteroatom-containing monomers, and tunable functionality, have attracted much attention in many fields [256–258]. Using N-containing molecular precursors as building blocks, COPs with different N distributions and hole sizes have been synthesized (Fig. 33a) [259]. After subsequent carbonization, well-controlled N-doped holey graphitic carbon materials were obtained and used as electrocatalysts for ORR. Experimental results demonstrated that the electrocatalytic performance of these N-doped holey graphitic carbon materials can be connected with the N locations in their COP molecular precursors, indicating the technical importance of the control of N-location for tailoring the structure and property of N-doped carbon nanomaterials. As shown in Fig. 33b, the electrocatalytic activities followed the order of C-COP-4 > C-COP-2 > C-COP-T > C-COP-P. C-COP-4 showed a similar onset potential as the Pt/C catalyst and half-wave potential of 0.78 V (Fig. 33 c-d). The transferred electron number (*n*) per O<sub>2</sub> molecule for C-COP-4 was calculated from Koutecky-Levich (K-L) plots to be 3.90. In accordance with experimental data, DFT calculations revealed that the N-doped C-COP-4 electrode can efficiently create the metal-free active sites for electrochemical reduction of O<sub>2</sub> through the charge redistribution (Fig. 33 e). The C-COP-4 electrode also exhibited tolerance to methanol crossover effect and a weak CO-poisoning effect (Fig. 33 f-g). Furthermore, 3D thermalized

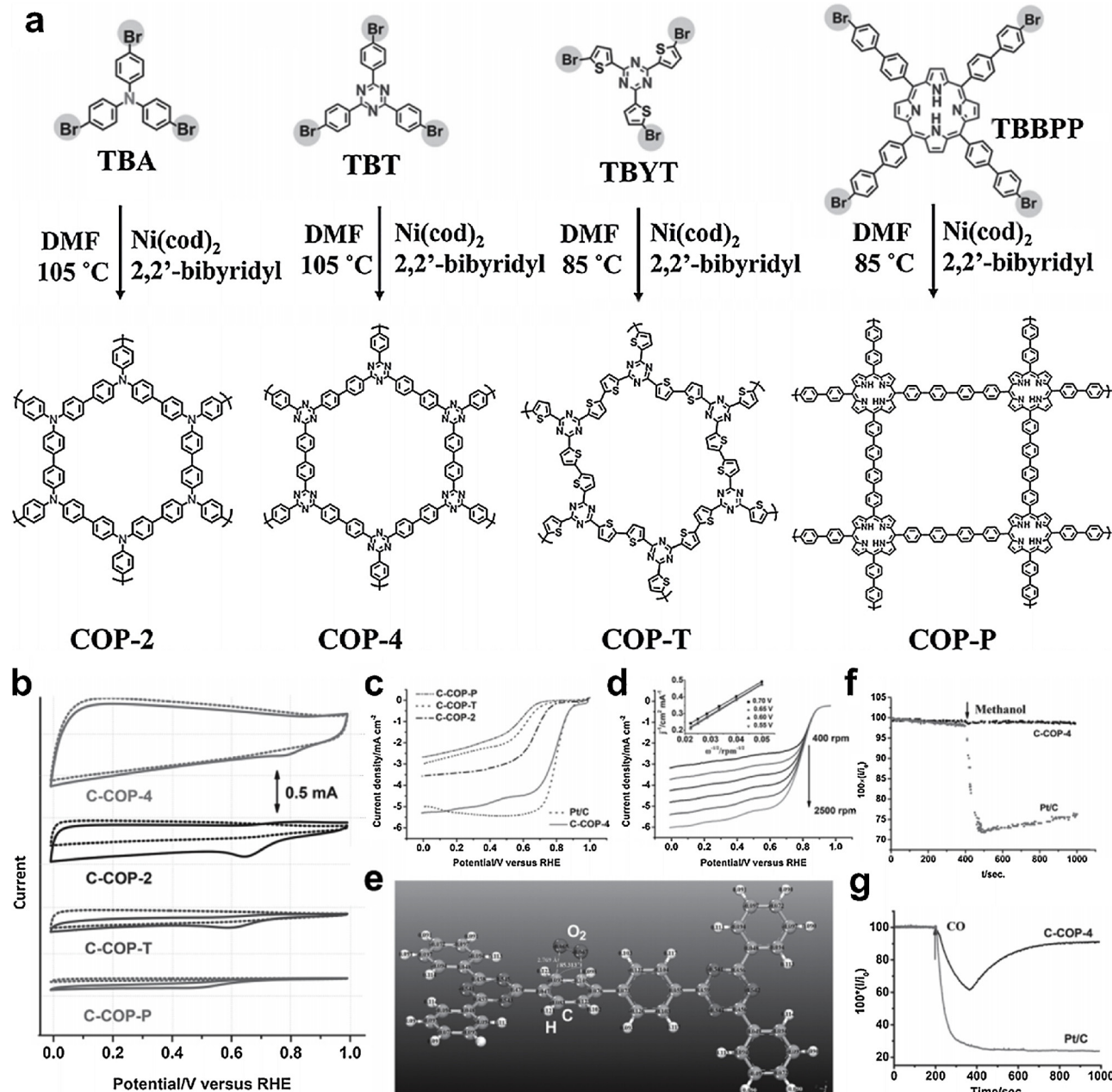


**Fig. 33.** (a) Schematic representation of synthesis of COP-2, COP-4, COP-T and COP-P through monomers tris(4-bromophenyl)amine (TBA), 2,4,6-tris-(4-bromophenyl)-[1,3,5] triazine (TBT), (4'-bromo-biphenyl-4-yl)-porphyrine (TBBPP) and 2,4,6-tris (5-bromo thiophen-2-yl)-1,3,5-triazine (TBYT), respectively, using nickel-catalyzed Yamamoto-type Ullmann cross-coupling reaction. The actual structures of these statistical COPs will be more complex than those represented here. (b) CV curves of COP graphitic electrodes in O<sub>2</sub>-saturated 0.1 M KOH at a sweep rate of 50 mV s<sup>-1</sup>. (c) LSV curves of COP graphitic electrodes in O<sub>2</sub>-saturated 0.1 M KOH at 1600 rpm at a sweep rate of 5 mV s<sup>-1</sup>. (d) RDE curves of C-COP-4 in O<sub>2</sub>-saturated 0.1 M KOH with different speeds at a scan rate of 5 mV s<sup>-1</sup>(the inset showing the K-L plots of the C-COP-4 derived from RDE measurements). (e) Calculated charge distributions for the cluster for optimal O<sub>2</sub> adsorbed on the COP-4 graphitic carbon. The measured distance is presented in angstroms, and the measured angle is presented in degrees. (f and g) Methanol and CO-poisoning effect evaluation on *i-t* chronoamperometric responses, respectively, for ORR at Pt/C (light gray) and C-COP-4 (black) electrodes. Reproduced from [259] Copyright 2014, Wiley-VCH.

triazine-based framework (TTF) was also successfully developed by the use of terephthalonitrile, acting as the basic building block and firstly translated into 2D covalent triazine-based framework (CTF) through trimerization [260]. Of particular interest, this bottom-up strategy imparted not only great opportunity to tune the nitrogen configurations of TTFs but also possibilities to co-dope with boron or fluorine. Recently, 2D conducting nanocarbons were achieved by combining the use of a 2D covalent organic framework (COF) with the development of a suitable template to guide the pyrolysis [261]. The COF produced nano-sized carbon sheets possessed high conductivity, hierarchical porosity,

and abundant heteroatom catalytic edges, achieving superior performance to commercial Pt/C in terms of long-term stability, and methanol tolerance.

Apart from the electrocatalysis of the ORR, sp<sup>2</sup>-C dominant carbon materials are also promising catalysts for the OER and HER to reduce or replace the use of noble metals and metal oxides [262]. Zhao et al. have reported the preparation of the nitrogen-doped carbon (N/C) materials, which were synthesized by the pyrolyzing the hybrid of a melamine/formaldehyde (MF) polymer and nickel nitrate at 700 °C, followed by the treatment of concentrated hydrochloric acid to remove the metal

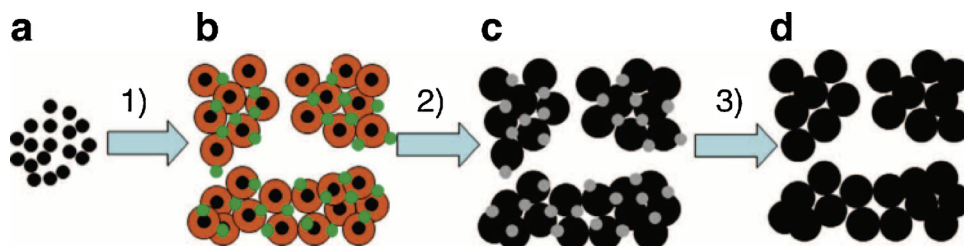


**Fig. 34.** Synthesis procedure of the N/C materials. Steps: (1) synthesis of MF polymer with nickel nitrate and carbon particles; (2) pyrolysing metal-salt/MF-polymer precursor; and (3) acid leaching of the pyrolysed samples. Materials: (a) carbon particles (black dot). (b) carbon particles covered with MF polymer (yellow sphere) and nickel nitrate (green dot). (c) N/C- $\text{NiO}_x$  catalyst (grey dot,  $\text{NiO}_x$ ). (d) N/C catalyst. Reproduced from [263] Copyright 2013, Nature Publishing Group (For interpretation of the references to colour in this figure legend, the reader is referred to the web version of this article).

species (Fig. 34) [263]. The optimized N/C materials showed OER overpotentials as low as 0.38 V at a current density of  $10 \text{ mA cm}^{-2}$  in pH 13 medium. The detailed electrochemical studies revealed that the high OER activity of the N/C materials is from the pyridinic-N- or/and quaternary-N-related active sites. Furthermore, surface-oxidized multiwall carbon nanotubes [264,265], edge-selectively phosphorus-doped few-layer graphene [265], and N,O-dual doped graphene-CNT hydrogel film [266] have been prepared and showed high OER activities. On the other hand, HER is a key reaction for the supply of sustainable hydrogen energy. The hybrid catalyst, coupling graphitic-carbon nitride ( $\text{g-C}_3\text{N}_4$ ) with nitrogen-doped graphene (NG), has been synthesized [267]. The resulting  $\text{C}_3\text{N}_4@\text{NG}$  hybrid exhibited comparable electrocatalytic HER activity with some well-developed metallic catalysts, such as nanostructured  $\text{MoS}_2$  materials. The unusual electrocatalytic properties were attributed to unique molecular structure and electronic properties originating from the synergistic effect of  $\text{g-C}_3\text{N}_4$  and NG, in which  $\text{g-C}_3\text{N}_4$  provides highly active hydrogen adsorption sites, while

NG enhances the electron-transfer process for the proton reduction. Moreover, there are several studies concentrating on dual-doped nanocarbons. For example, Zheng et al., based on theoretical predictions, have designed N and P dual-doped graphene with higher electrocatalytic HER activity than single-doped ones [268]. Yan et al. synthesized N, P co-doped carbon nanofiber networks derived from electrochemically polymerized

PANI with the addition of phytic acid (PA) [269]. The synergistic effect between the primary dopant, nitrogen, and secondary elements such as B, P, and S have been evaluated. Systematic investigation demonstrated the S shows greater promotion in HER activity for N-doped carbon compared with P and B, which on the contrary, decrease the activity of N-doped carbons [270]. More interestingly, a fully  $\text{sp}^2$ -hybridized nitrogenated 3D microporous graphitic framework (3D-MGF) has been reported recently, which was prepared by ionothermal reaction conditions and possessed extended  $\pi$ -electron conjugation and narrow PSD (Fig. 35) [271]. After the  $\text{H}_2\text{SO}_4$  aging, the acid treated 2D-

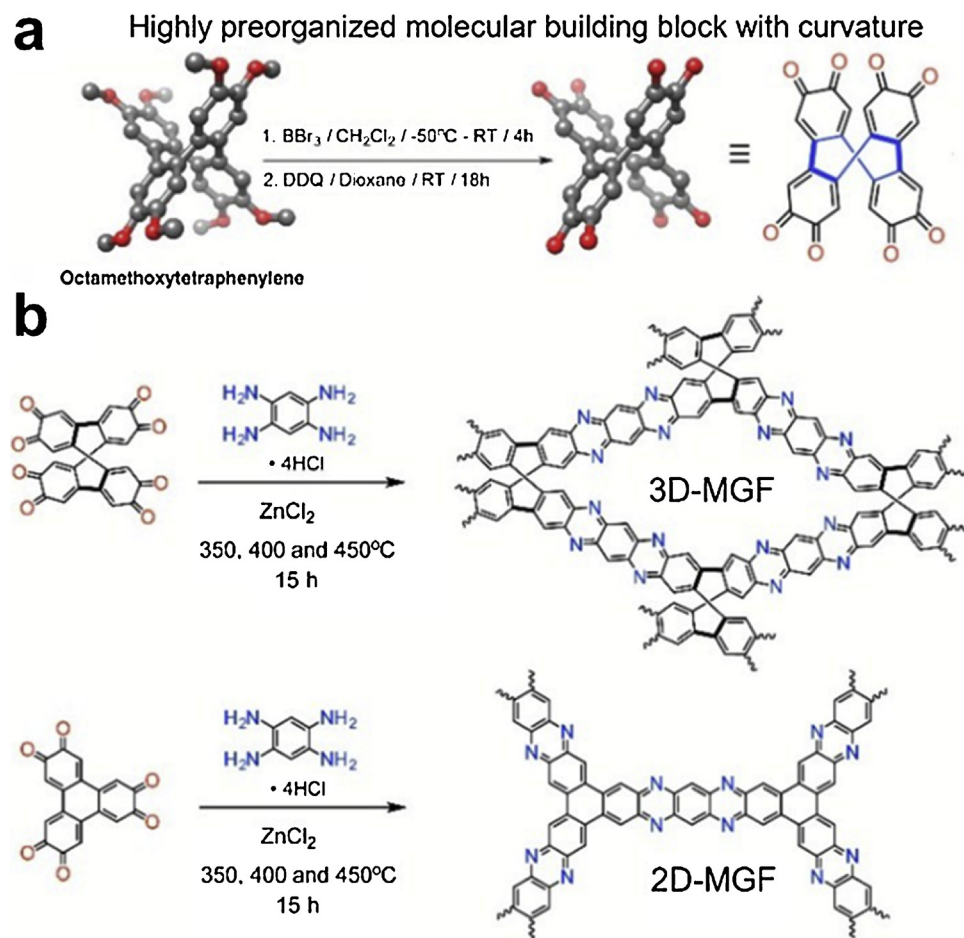


**Fig. 35.** (a) Chemical structure of octaketotetraphenylene as a highly preorganized molecular precursor with negative curvature along with the X-ray crystal structure of octamethoxytetraphenylene. (b) Synthetic strategy for the preparation of  $\pi$ -conjugated 2D- and 3D-MGFs. Reproduced from [271] Copyright 2017, Royal Society of Chemistry.

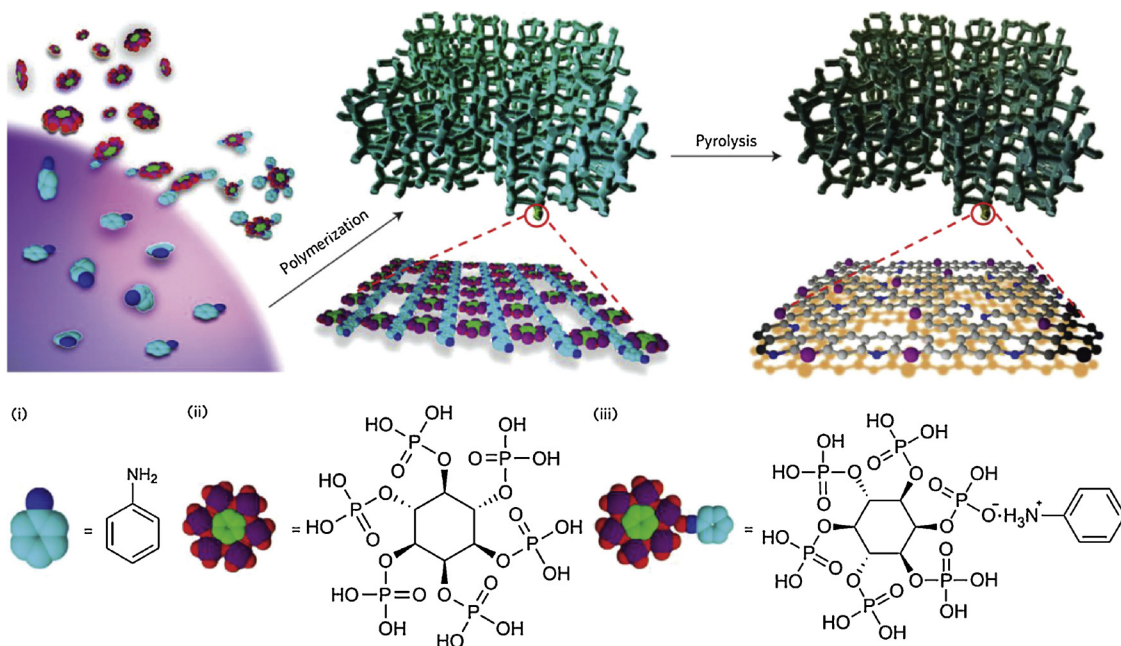


**Fig. 36.** Schematic illustration of the preparation process for the NPMC foams. An aniline (i) phytic acid (ii) complex (iii) is formed (for clarity, only one of the complexed anilines is shown for an individual phytic acid), followed by oxidative polymerization into a three-dimensional PANI hydrogel crosslinked with phytic acids. Reproduced from [272] Copyright 2015, Nature Publishing Group.

MGF ( $\text{H}^+$ -2D-MGF) and 3D-MGF ( $\text{H}^+$ -3D-MGF) showed the overpotentials of 450 and 440 mV at  $-10 \text{ mA cm}^{-2}$ , respectively.

With the development of  $\text{sp}^2\text{-C}$  dominant carbon materials for various electrocatalytic reactions, bi- and trifunctional metal-free catalysts have aroused much attention. N and P co-doped porous carbon (NPMC) electrocatalysts were fabricated using a scalable, one-step process involving the pyrolysis of a PANI aerogel synthesized in the presence of PA (Fig. 36) [272]. Electrochemical evaluation revealed that NPMC displayed good electrocatalytic properties with a half-wave potential of 0.85 V for ORR and lower onset potentials and higher currents than those of the Pt/C electrode for OER. NPMC-1000 acting as the air cathode, a two-electrode rechargeable Zn-air battery could be cycled stably for 180 cycles at  $2 \text{ mA cm}^{-2}$ . To analyze the mechanism of bi-functional NPMCs for ORR and OER, DFT calculations were performed, which revealed that the N,P co-doping and graphene edge effects are essential for the bi-functional electrocatalytic activity. Flexible, large-area 3D porous N-doped carbon microtube (NCMT) sponges have been prepared via a simple and low-cost procedure of pyrolyzing facial cotton [273]. Owing to unique structure with a micron-scale hollow core and well-graphitized and interconnected porous walls, the optimized NCMT sponge showed incomparable electrocatalytic activity for ORR and OER with a small potential difference of 0.63 V between the ORR current density at  $3 \text{ mA cm}^{-2}$  and the OER current density at  $10 \text{ mA cm}^{-2}$ . Additionally, graphene- and CNT-based carbon materials also present bi-functional electrocatalytic activity for ORR/OER [274–278]. Tian et al. have prepared a N-doped graphene/single-walled carbon nanotube hybrid (NGSH) material as an bi-functional electrocatalyst for both ORR and OER [274]. P,N co-doped graphene frameworks (PNGFs) with highly effective bi-functionality have been achieved, where P-N sites is active for OER and N-doped sites for ORR [275]. Furthermore, 3D N,P-codoped carbon networks were developed by pyrolysis of a supermolecular aggregate of self-assembled melamine, phytic acid, and graphene oxide (MPSA/GO) [279]. The pyrolyzed MPSA/GO was the first metal-free bi-functional electrocatalyst with high activities for both ORR and HER. Additionally, Zhang et al. have reported N, P, and F tri-doped graphene exhibited excellent electrocatalytic activities for ORR, OER and HER [280].

Moreover,  $\text{sp}^2\text{-C}$  dominant carbon materials can also act as

electrocatalysts for electroreduction of  $\text{CO}_2$  into higher-energy liquid fuels and chemicals, which is a promising but challenging regenerable energy conversion technology. Polyacrylonitrile-based heteroatomic carbon nanofibres have demonstrated to be effective metal-free electrocatalysts for  $\text{CO}_2$  reduction into CO, in which the electrocatalytic ability is attributed to the reduced carbons rather than to electro-negative nitrogen atoms [234]. The carbon nanofibre catalyst exhibited negligible overpotential (0.17 V) for  $\text{CO}_2$  reduction and more than an order of magnitude higher current density compared with the silver catalyst under similar experimental conditions. Subsequently, nitrogen-doped CNTs [281,282], N-doped 3D graphene foam [283], and N-doped graphene quantum dots [235] have also been confirmed to electrochemically reduce  $\text{CO}_2$  to value-added chemicals.

#### 4.1.2. Catalyst support

Owing to their high surface area, good mechanical and electrical properties, and tunable functionality, a variety of  $\text{sp}^2\text{-C}$  dominant carbon materials such as CNTs, graphene, carbon nanofibers, mesoporous carbon, and graphite have been regarded as ideal catalyst support materials [284,285]. After doping with heteroatoms, the resultant  $\text{sp}^2\text{-C}$  dominant carbon materials could improve electrocatalyst dispersion, modify interaction between carbon support and catalyst and hence enhance the stability and activity of metal catalysts. Sun et al. have reported that Pt nanoparticles could be uniformly distributed on the sidewalls of vertically aligned nitrogen-containing carbon nanotube ( $\text{CN}_x \text{ NT}$ ) [286]. The nanocomposites were prepared by the combination of microwave-plasma-enhanced chemical vapor deposition (MPECVD) and sputtering methods. Furthermore, nitrogen-doped reduced graphene oxide (NRGO) could also act as a catalyst support for Pt nanoparticles [287]. The prepared Pt/NRGO possessed a higher electrocatalytic activity and lower losses of the electrochemically active surface area than those of the Pt/GO and conventional Pt/C catalysts. Moreover,  $\text{sp}^2\text{-C}$  dominant carbon materials supported non-novel metal-based catalysts also show practical significance. Liang et al. have reported a hybrid material consisting of  $\text{Co}_3\text{O}_4$  nanocrystals grown on N-doped reduced mildly oxidized graphene oxide (rmGO) [288]. The  $\text{Co}_3\text{O}_4/\text{N-rmGO}$  hybrid exhibited similar catalytic activity but superior stability to Pt for ORR and high activity for OER in alkaline solutions.

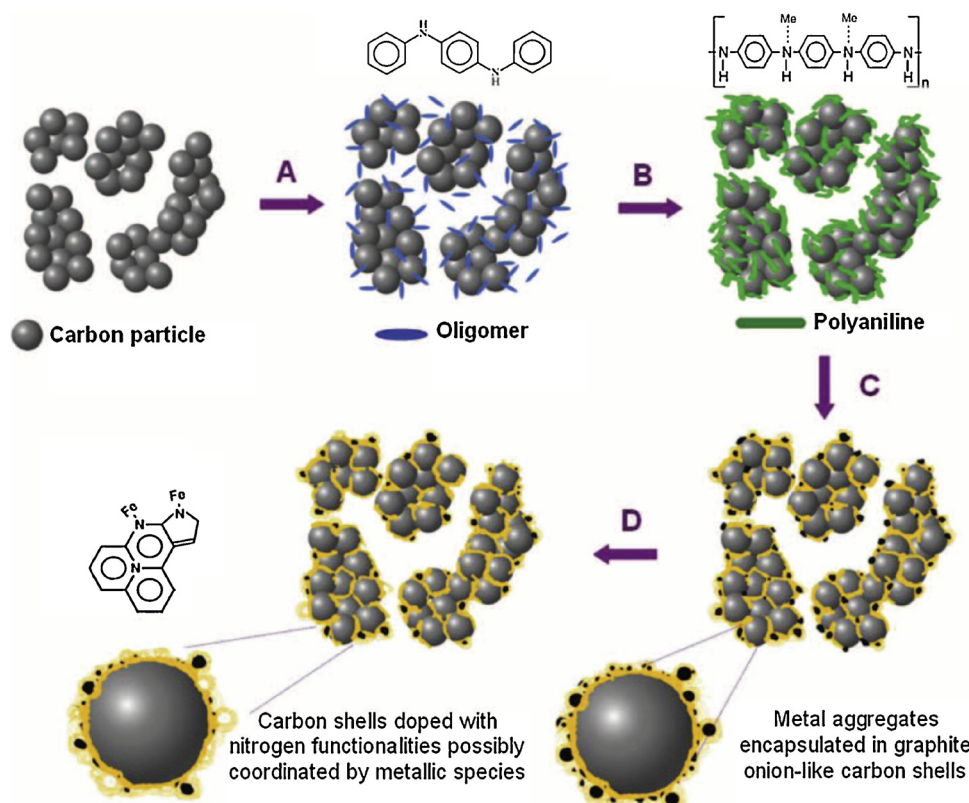


**Fig. 37.** Schematic diagram of the synthesis of PANI-M-C catalysts. (A) Mixing of high-surface area carbon with aniline oligomers and transition-metal precursor (M: Fe and/or Co). (B) Oxidative polymerization of aniline by addition of ammonium persulfate (APS). (C) First heat treatment in  $N_2$  atmosphere. (D) Acid leaching. The second heat treatment after acid leach is not shown. Reproduced from [293] Copyright 2011, American Association for the Advancement of Science.

The unusual catalytic activity results from synergistic chemical coupling effects between  $Co_3O_4$  and graphene. On the other hand, Liang et al. also synthesized CoO/nitrogen-doped CNT strongly coupled hybrid, which presented high ORR current density that outperformed  $Co_3O_4$ /graphene hybrid and commercial Pt/C catalyst at medium overpotential [289]. Importantly, nitrogen-doped graphene as an emerging catalyst support has aroused wide interest recently. For example, 3D N-doped graphene aerogel (N-GA)-supported  $Fe_3O_4$  nanoparticles ( $Fe_3O_4/N$ -GAs) have been demonstrated to be an excellent ORR catalyst with a more positive onset potential, higher cathodic density, lower  $H_2O_2$  yield, and higher electron transfer number in alkaline media than  $Fe_3O_4$  NPs supported on N-doped carbon black ( $Fe_3O_4/N$ -CB) or N-doped graphene sheets ( $Fe_3O_4/N$ -GSs) [290]. Graphene layers-wrapped Fe/ $Fe_5C_2$  nanoparticles supported on N-doped graphene nanosheets (GL-Fe/ $Fe_5C_2$ /NG) have been prepared to be a highly efficient ORR electrocatalyst [291]. Co/ $CoFe_2O_4$  nanoparticles supported on N-doped graphene were synthesized to be an efficient bi-functional electrocatalyst towards ORR and OER [292].

Metal-nitrogen-carbon (M-N-C) catalysts, as a class of promising nonprecious metal catalysts, have received much attention recently. In particular, PANI-M-C catalysts have been synthesized by heat treatment of precursors comprising nitrogen, carbon, and transition metals (such as Fe and/or Co) (Fig. 37) [293]. The half-wave potential of the most active PANI-Fe-C catalyst was only 59 mV lower than that of Pt/C in acid media. The PANI-FeCo-C catalyst showed remarkable performance stability via a 700-hour fuel-cell performance test at a constant cell voltage of 0.4 V. Subsequently, a variety of M-N-C catalysts have been reported. For instance, Liang et al. prepared cobalt-nitrogen-doped carbon (C-N-Co) and iron-nitrogen-doped carbon (C-N-Fe) from vitamin B12 (VB12) and the polyaniline-Fe (PANI-Fe) complex, respectively [294]. Lin et al. synthesized heterometalloporphyrinic carbons by carbonizing a series of metallic-constituent-controllable metallo-multi-porphyrin porous conjugated networks, which exhibited excellent ORR activity [295]. Chen et al. prepared porous carbons with highly dispersed N and abundant  $CoN_x$  active species via pyrolysis of a series of

bimetallic metal-organic frameworks [296]. More recently, single atomic catalyst is a rapidly developing hot research topic in electrocatalysis, where N-coordinated transition metal centers ( $M-N_x$ ) act as dominant active sites. Li et al. have reported several different single-atom catalysts, such as Co single atoms supported on nitrogen-doped porous carbon [297], isolated single-atom Fe anchored on N-doped porous carbon [298], and Fe-Co dual sites embedded on N-doped porous carbon [299]. These single-atom catalysts showed superior ORR activity and long-term durability.

#### 4.2. Applications for solar cells

Solar cells are considerable technologies to produce electricity through photoelectric effect. With the unique properties, such as highly electrical conductivity, mechanical flexibility, and high catalytic activity,  $sp^2$ -C dominant carbon materials, especially graphene-based materials, have been widely investigated in the field of solar cells, where these materials can act as transparent conductive electrodes and catalytic counter electrodes [300,301].

##### 4.2.1. Catalytic counter electrodes

Apart from being transparent conductive electrodes,  $sp^2$ -C dominant carbon materials can also be used to replace expensive platinum as the catalytic counter electrodes in DSSCs with comparable performance to that of platinum electrode [302]. Aksay et al. have used functionalized graphene sheets (FGS) with oxygen-containing sites as the catalytic counter electrode material in a fully fabricated DSSC with a performance similar to that of platinum [303]. The FGS-based DSSC devices reached a high efficiency ( $\eta$ ) of 4.99%, which is more than 90% that of platinum-based cells ( $\eta = 5.48\%$ ). The excellent catalytic activity of FGS toward the reduction of  $I_3^-$  [304]. The ECGnP counter electrodes showed enhanced electrochemical stability for the  $Co(bpy)_3^{2+/3+}$  ( $bpy = 2,2'$ -bipyridine) redox couple compared to the platinum, and the ECGnP-based DSSC devices exhibited a higher power conversion efficiency (PCE) (9.31%) than that of the Pt electrode (8.67%).

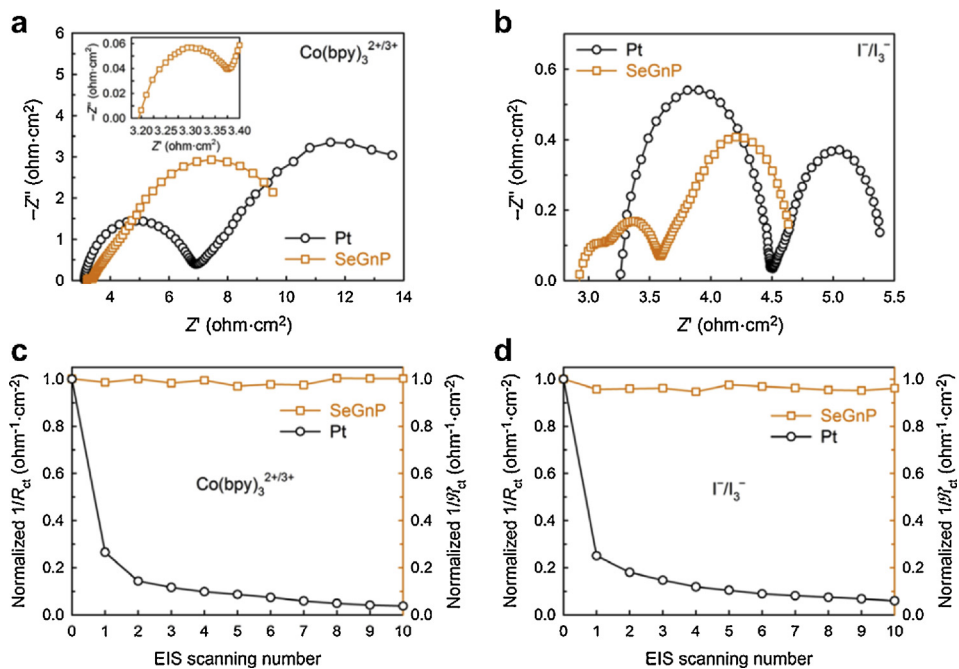


**Fig. 38.** Comparison between conventional Pt and SeGnP electrodes. Nyquist plots of the Pt-CEs and SeGnP-CEs:  $\text{Co}(\text{bpy})_3^{2+/3+}$  (a) and  $\text{I}_3^-$  ct and  $R_{ct}$  changes versus the EIS scan number:  $\text{Co}(\text{bpy})_3^{2+/3+}$  (c) and  $\text{I}_3^-$  [305] Copyright 2016, American Association for the Advancement of Science.

Similarly, edge-selenated graphene nanoplatelets (SeGnP) from ball milling could act as the counter electrodes for DSSCs in both  $\text{I}_3^-$ <sup>2+/3+</sup> electrolytes [305]. The electrochemical impedance spectroscopy (EIS) results demonstrated that the SeGnP counter electrodes exhibited superb electrocatalytic performance and ultimately high stability in both electrolytes (Fig. 38). Furthermore, N-doped graphene [306,307], N-doped graphene foams [308], and N-doped graphene nanoribbons [309,310] have also been reported to exhibit improved catalytic activity towards  $\text{I}_3^-$  [311]. The DSSC devices assembled with an N-doped CNT counter electrode displayed a PCE of 7.04%, comparable to that of Pt electrode (7.34%).

#### 4.2.2. Transparent conductive electrodes

The sheet resistance and transparency of transparent conductive electrodes are two key factors that affect the performance of carbon-based solar cells. Therefore, CNT- and graphene-based materials have been extensively investigated as promising transparent conductive electrodes. Parekh et al. have reported that exposure to nitric acid ( $\text{HNO}_3$ ) and thionyl chloride ( $\text{SOCl}_2$ ) could effectively improve the conductivity of transparent and conducting single-wall carbon nanotube (SWCNT) thin films [311,312]. The  $\text{SOCl}_2$  functionalized SWCNT films exhibited sheet resistances of 40–50  $\Omega\text{sq}^{-1}$  albeit at lower transmittance (~50%). A graphene thin film was prepared by dip

coating of a hot, aqueous GO dispersion and subsequent thermal treatment, which exhibited a high conductivity of 550  $\text{Scm}^{-1}$  and a transparency of more than 70% over 1000–3000 nm [313]. A dye-sensitized solar cell (DSSC) with configuration of graphene/TiO<sub>2</sub>/dye/spiro-OMeTAD/Au has been assembled using the graphene film as anode and Au as cathode. The energy level diagram of the fabricated device revealed that the work function of the graphene film (4.42 eV) was close to that of fluorine-doped tin oxide (FTO) electrode (4.4 eV), while the conversion efficiency (PCE) of graphene-based cell (0.26%) was still lower compared to FTO-based cell (0.84%) as reflected by the current-voltage (*I*-*V*) characteristics. Furthermore, Yin et al. have used chemically reduced graphene oxide (rGO) as the transparent conductive electrodes for flexible organic photovoltaic (OPV) devices [314]. The performance of the OPV devices mainly depends on the charge transport efficiency and the light transmission efficiency of rGO films, when the optical transmittance of rGO is above and below 65%, respectively. Of particular interest, the prepared OPV devices could sustain a thousand cycles of bending at 2.9% tensile strain.

Table 3 summarizes the energy conversion applications for sp<sup>2</sup> C-dominant carbon materials and related typical examples that were mentioned above.

**Table 3**  
Energy conversion applications for sp<sup>2</sup> C-dominant carbon materials and related examples.

Applications	Critical technique	Examples
Electrocatalysis	Catalytic active materials	vertically aligned nitrogen-containing carbon nanotubes (VA-NCNTs) [239] Edge-selectively functionalized graphene nanoplatelets (EFGnP) [242]
	Catalyst support	vertically aligned BCN (VA-BCN) nanotubes [246] vertically aligned nitrogen-containing carbon nanotube (CN <sub>x</sub> NT) as support for Pt nanoparticles [286] N-doped reduced mildly oxidized graphene oxide as support for Co <sub>3</sub> O <sub>4</sub> nanocrystals [288]
Solar cells	Catalytic counter electrodes	Metal-nitrogen-carbon (M-N-C) catalysts [293,294,295,296,297,298,299] functionalized graphene sheets (FGS) with oxygen-containing sites [303]
	Transparent conductive electrodes	Edge-carboxylated graphene nanoplatelets (ECGnP) [304] single-wall carbon nanotube (SWCNT) thin films [312] graphene thin film [313] chemically reduced graphene oxide (rGO) [314]

## 5. Summary and outlook

In this review, we have reviewed a class of  $sp^2$ -C dominant carbonaceous materials lying between the ideally no-defect hexagonally-arranged  $sp^2$ -bonded carbon (e.g. graphene, carbon nanotube) and traditional polymer. The latest remarkable progress has been summarized in the preparation of  $sp^2$ -C dominant carbonaceous materials following two main categories: (1) the bottom-up synthesis approaches with diverse monomers and/or naturally occurring biomaterials as precursors, and (2) the top-down preparation means, in terms of the chemical composition, pore structure, geometric morphology, and interface contact. The existing advances in synthesis strategies and construction methodologies of these  $sp^2$ -C dominant carbonaceous materials have in turn promoted their energy related applications. In this regard, the deep understanding of both underlying mechanism and structure-property correlation in each energy conversion and storage process is highlighted, playing guiding significance roles in the target exquisite structural design of  $sp^2$ -C dominant carbonaceous materials. Despite these advances, the synthesis and application of  $sp^2$ -C dominant carbonaceous materials are still in their early stages. There are still quite challenging aspects that imperatively need to be further focused and overcome in the future.

From the synthetic viewpoint, precise control and manipulation of  $sp^2$ -C dominant carbonaceous materials, especially toward the large-scale production, remain challenging. Generally speaking, the bottom-up synthesis strategies represent a highly controllable tactic to elaborately tailor the molecular configurations of  $sp^2$ -C dominant carbonaceous materials, including the size and number of  $sp^2$  covalent sub-units, chemical functionalities, the interconnecting manners, and also the resulting pore patterns at atomic precision. However, this strategy generally experiences complex reaction processes and low yields, making it difficult to synthesize on a large scale. In comparison, the top-down preparation strategies hold up-scalability for constructing  $sp^2$ -C dominant carbonaceous products and would be more promising but usually yielding accurate regulation. In addition, in the industry-level production of  $sp^2$ -C dominant carbonaceous materials for practical energy related applications, greater attempts must be made to render them to be economically viable and environmentally benign toward a more sustainable development that is indeed a global concern.

For energy-related applications, the contribution of different structural effects to enhanced performance has not yet been comprehensively and thoroughly investigated. Moreover, the situations of these structural information in various energy-related applications would be quite different. Taking sodium-ion batteries as an example, the improvement in the initial Coulombic efficiency and rate capability is still quite challenging. For its commercialized application, initial Coulombic efficiency of  $> 90\%$  is required. Yet, the typically reported carbonaceous materials exhibit an initial Coulombic efficiency of  $< 70\%$ . In this regard, the bottom-up strategy towards customized design of unique structures with sufficient reversible  $\text{Na}^+$  storage active sites and smoothed  $\text{Na}^+$  diffusion path would play a more important role in understanding the structure-property relationship of  $sp^2$ -C dominant carbonaceous materials. In particular, theoretical modelling and calculation on the interfacial interactions, dynamic evolution of the structure, interface, volume, charge transport and energy related influencing mechanisms are indispensable for better understanding the structure-property relationships and consequently rationally optimizing the design, construction, and charge storage process of such  $sp^2$ -C dominant carbonaceous materials. With the great achievements and continuous efforts in this important field, it is strongly believed that  $sp^2$ -C dominant carbonaceous material will occupy an extensively large stage and play important roles in different energy technologies in the future.

## Conflicts of interest

There are no conflicts to declare.

## Acknowledgements

Debin Kong and Zhichang Xiao contributed equally to this work. The authors acknowledge the financial support from the National Natural Science Foundation of China (Grant No. 51425302, 51702062), the Beijing Municipal Science and Technology Commission (Z121100006812003), and Youth Innovation Promotion Association (CAS).

## References

- [1] G. Wang, L. Zhang, J. Zhang, Chem. Soc. Rev. 43 (2012) 797–828.
- [2] F. Bonaccorso, L. Colombo, G. Yu, M. Stoller, V. Tozzini, A.C. Ferrari, R.S. Ruoff, V. Pellegrini, Science 347 (2015) 1246501.
- [3] P. Simon, Y. Gogotsi, Acc. Chem. Res. 46 (2013) 1094–1103.
- [4] L.L. Zhang, X.S. Zhao, Chem. Soc. Rev. 38 (2009) 2520–2531.
- [5] S. Xin, Y.-G. Guo, L.-J. Wan, Acc. Chem. Res. 45 (2012) 1759–1769.
- [6] Z.L. Wang, D. Xu, J.J. Xu, X.B. Zhang, Chem. Soc. Rev. 43 (2014) 7746–7786.
- [7] M.M. Liu, R.Z. Zhang, W. Chen, Chem. Rev. 114 (2014) 5117–5160.
- [8] N. Yabuuchi, K. Kubota, M. Dahbi, S. Komaba, Chem. Rev. 114 (2014) 11636–11682.
- [9] C.M. Park, J.H. Kim, H. Kim, H.J. Sohn, Chem. Soc. Rev. 39 (2010) 3115–3141.
- [10] P.G. Bruce, S.A. Freunberger, L.J. Hardwick, J.M. Tarascon, Nat. Mater. 11 (2012) 19–29.
- [11] M. Chhowalla, H.S. Shin, G. Eda, L.J. Li, K.P. Loh, H. Zhang, Nat. Chem. 5 (2013) 263–275.
- [12] C.K. Chan, H.L. Peng, G. Liu, K. McIlwraith, X.F. Zhang, R.A. Huggins, Y. Cui, Nat. Nanotech. 3 (2008) 31–35.
- [13] Z. Wei Seh, W. Li, J.J. Cha, G. Zheng, Y. Yang, M.T. McDowell, P.C. Hsu, Y. Cui, Nat. Commun. 4 (2013) 1331.
- [14] C.P. Yang, Y.X. Yin, S.F. Zhang, N.W. Li, Y.G. Guo, Nat. Commun. 6 (2015) 8058.
- [15] P. Simon, Y. Gogotsi, Nat. Mater. 7 (2008) 845.
- [16] K. Kim, T. Lee, Y. Kwon, Y. Seo, J. Song, J.K. Park, H. Lee, J.Y. Park, H. Ihée, S.J. Cho, R. Ryoo, Nature 535 (2016) 131.
- [17] H. Cui, Z. Zhou, D. Jia, Mater. Horiz. 4 (2017) 7–19.
- [18] H.-G. Jung, J. Hassoun, J.-B. Park, Y.-K. Sun, B. Scrosati, Nat. Chem. 4 (2012) 579–585.
- [19] Q. Zhao, W. Huang, Z. Luo, L. Liu, Y. Lu, Y. Li, L. Li, J. Hu, H. Ma, J. Chen, Sci. Adv. 4 (2018) 1761.
- [20] F. Beguin, V. Presser, A. Balducci, E. Frackowiak, Adv. Mater. 26 (2014) 2219–2251 2283.
- [21] H. Jiang, P.S. Lee, C.Z. Li, Energy Environ. Sci. 6 (2013) 41–53.
- [22] G. Wu, Y. Hu, Y. Liu, J. Zhao, X. Chen, V. Whoehling, C. Plesse, G.T. Nguyen, F. Vidal, W. Chen, Nat. Commun. 6 (2015) 7258.
- [23] X. Liu, L. Dai, Nat. Rev. Mater. 1 (2016) 16064.
- [24] S. Ahmad, D. Copic, C. George, M. De Volder, Adv. Mater. 28 (2016) 6704.
- [25] Y. Zhu, S. Murali, M.D. Stoller, K.J. Ganesh, R.S. Ruoff, Science 332 (2011) 1537.
- [26] J. Zhu, C. Tang, Z. Zhuang, C. Shi, N. Li, L. Zhou, L. Mai, ACS Appl. Mater. Interfaces 9 (2017) 24584–24590.
- [27] Y. Wu, J. Meng, Q. Li, C. Niu, X. Wang, W. Yang, W. Li, L. Mai, Nano Res. 10 (2017) 2364–2376.
- [28] J.T. Zhang, Z.H. Zhao, Z.H. Xia, L.M. Dai, Nat. Nanotech. 10 (2015) 444–452.
- [29] B. Wang, J. Ryu, S. Choi, G. Song, D. Hong, C. Hwang, X. Chen, B. Wang, W. Li, H.-K. Song, S. Park, R.S. Ruoff, ACS Nano 12 (2018) 1739–1746.
- [30] S. Chen, L. Shen, P.A. Van Aken, J. Maier, Y. Yu, Adv. Mater. 29 (2017) 1605650.
- [31] X. Cao, B. Zheng, W. Shi, J. Yang, Z. Fan, Z. Luo, X. Rui, B. Chen, Q. Yan, H. Zhang, Adv. Mater. 27 (2015) 4695–4701.
- [32] J. Dong, Y. Xue, C. Zhang, Q. Weng, P. Dai, Y. Yang, M. Zhou, C. Li, Q. Cui, X. Kang, C. Tang, Y. Bando, D. Golberg, X. Wang, Adv. Mater. 29 (2016) 1603692.
- [33] P. Chen, T.Y. Xiao, Y.H. Qian, S.S. Li, S.H. Yu, Adv. Mater. 25 (2013) 3192–3196.
- [34] L. Zhi, K. Müllen, J. Mater. Chem. 18 (2008) 1472–1484.
- [35] B. Schuler, S. Collazos, L. Gross, G. Meyer, D. Perez, E. Guitian, D. Pena, Angew. Chem. Int. Ed. 53 (2014) 9004–9006.
- [36] L. Chen, S.R. Puniredd, Y.Z. Tan, M. Baumgarten, U. Zschieschang, V. Enkelmann, W. Pisula, X. Feng, H. Klauk, K. Müllen, J. Am. Chem. Soc. 134 (2012) 17869–17872.
- [37] Y. Geng, A. Fechtenkötter, K. Müllen, J. Mater. Chem. 11 (2001) 1634–1641.
- [38] V.S. Iyer, M. Wehmeier, J.D. Brand, M.A. Keegstra, K. Müllen, Angew. Chem. Int. Ed. 36 (1997) 1604–1607.
- [39] S. Ito, M. Wehmeier, J.D. Brand, C. Kübel, R. Epsch, J.P. Rabe, K. Müllen, Chem. Eur. J. 6 (2000) 4327–4342.
- [40] Z. Tomovic, M.D. Watson, K. Müllen, Angew. Chem. Int. Ed. 43 (2004) 755.
- [41] F. Morgenroth, K. Müllen, Tetrahedron 53 (1997) 15349–15366.
- [42] C. Kübel, K. Eckhardt, V. Enkelmann, G. Wegner, K. Müllen, J. Mater. Chem. 10 (2000) 879–886.
- [43] P. Herwig, C.W. Kayser, K. Müllen, H.W. Spiess, Adv. Mater. 8 (1996) 510–513.
- [44] C.D. Simpson, G. Mattersteig, M. Kai, L. Gherghel, R.E. Bauer, H.J. Rader,

- K. Müllen, J. Am. Chem. Soc. 126 (2004) 3139–3147.
- [45] C.D. Simpson, J.D. Brand, A.J. Berresheim, L. Przybilla, H.J. Rader, K. Müllen, Chem. Eur. J. 8 (2002) 1424–1429.
- [46] S. Bi, Z.-A. Lan, S. Paasch, W. Zhang, Y. He, C. Zhang, F. Liu, D. Wu, X. Zhuang, E. Brunner, X. Wang, F. Zhang, Adv. Funct. Mater. (2017) 1703146.
- [47] X. Li, X. Wang, L. Zhang, S. Lee, H. Dai, Science 319 (2008) 1229–1232.
- [48] M.Y. Han, B. Ozyilmaz, Y. Zhang, P. Kim, Phys. Rev. Lett. 98 (2007) 206805.
- [49] Y.W. Son, M.L. Cohen, S.G. Louie, Phys. Rev. Lett. 97 (2006) 216803.
- [50] Z. Chen, Y.M. Lin, M.J. Rooks, P. Avouris, Phys. E 40 (2007) 228–232.
- [51] D.V. Kosynkin, A.L. Higginbotham, A. Sinitskii, J.R. Lomeda, A. Dimiev, B.K. Price, J.M. Tour, Nature 458 (2009) 872–876.
- [52] X. Yang, X. Dou, A. Rouhanipour, L. Zhi, H.J. Räder, K. Müllen, J. Am. Chem. Soc. 130 (2008) 4216–4217.
- [53] M.G. Schwab, A. Narita, Y. Hernandez, T. Balandina, K.S. Mali, F.S. De, X. Feng, K. Müllen, J. Am. Chem. Soc. 134 (2012) 18169–18172.
- [54] L. Dössel, L. Gherghel, X. Feng, K. Müllen, Angew. Chem. Int. Ed. 50 (2011) 2540–2543.
- [55] A. Narita, X. Feng, Y. Hernandez, S.A. Jensen, M. Bonn, H. Yang, I.A. Verzhbitskiy, C. Casiraghi, M.R. Hansen, A.H.R. Koch, G. Fytas, O. Ivasenko, B. Li, K.S. Mali, T. Balandina, S. Mahesh, S. De Feyter, K. Müllen, Nat. Chem. 6 (2014) 126–132.
- [56] X. Feng, Y. Liang, L. Zhi, A. Thomas, D. Wu, I. Lieberwirth, U. Kolb, K. Müllen, Adv. Funct. Mater. 19 (2009) 2125–2129.
- [57] L.J. Zhi, J.S. Wu, J.X. Li, M. Stepputat, U. Kolb, K. Müllen, Adv. Mater. 17 (2005) 1492–1496.
- [58] Y. Liang, X. Feng, L. Zhi, U. Kolb, K. Müllen, Chem. Commun. (Camb.) 7 (2009) 809–811.
- [59] C. Moreno, M. Vilas-Varela, B. Kretz, A. Garcia-Lekue, M.V. Costache, M. Paradinas, M. Panighel, G. Ceballos, S.O. Valenzuela, D. Pena, Science 360 (2018) 199–203.
- [60] L. Hao, J. Ning, B. Luo, B. Wang, Y. Zhang, Z. Tang, J. Yang, A. Thomas, L. Zhi, J. Am. Chem. Soc. 137 (2015) 219–225.
- [61] Z. Xiao, D. Kong, J. Liang, B. Wang, R. Iqbal, Q.-H. Yang, L. Zhi, Carbon 116 (2017) 633–639.
- [62] Z. Xiao, Q. Song, R. Guo, D. Kong, S. Zhou, X. Huang, R. Iqbal, L. Zhi, Small 14 (2018) e1703569.
- [63] Z. Xiao, D. Kong, Q. Song, S. Zhou, Y. Zhang, A. Badshah, J. Liang, L. Zhi, Nano Energy 46 (2018) 365–371.
- [64] Z. Xiao, J. Han, J. Xiao, Q. Song, X. Zhang, D. Kong, Q.H. Yang, L. Zhi, Nanoscale 10 (2018) 10351–10356.
- [65] Z. Li, L. Zhang, B.S. Amirkhiz, X. Tan, Z. Xu, H. Wang, B.C. Olsen, C.M.B. Holt, D. Mitlin, Adv. Energy Mater. 2 (2012) 431–437.
- [66] E. Raymundo-Piñero, M. Cadek, F. Béguin, Adv. Funct. Mater. 19 (2009) 1032–1039.
- [67] Z. Li, Z. Xu, X. Tan, H. Wang, C.M.B. Holt, T. Stephenson, B.C. Olsen, D. Mitlin, Energy Environ. Sci. 6 (2013) 871–878.
- [68] S. Gao, K. Geng, H. Liu, X. Wei, M. Zhang, P. Wang, J. Wang, Energy Environ. Sci. 8 (2014) 221–229.
- [69] J. Hou, C. Cao, F. Idrees, X. Ma, ACS Nano 9 (2015) 2556.
- [70] C. Guo, W. Liao, Z. Li, C. Chen, Carbon 85 (2015) 279–288.
- [71] P. Kleszik, P. Ratajczak, P. Skowron, J. Jagiello, Q. Abbas, E. Frąckowiak, F. Béguin, Carbon 81 (2015) 148–157.
- [72] L. Sun, C. Tian, M. Li, X. Meng, L. Wang, R. Wang, J. Yin, H. Fu, J. Mater. Chem. A Mater. Energy Sustain. 1 (2013) 6462–6470.
- [73] H. Wang, Z. Xu, A. Kohandehghan, Z. Li, K. Cui, X. Tan, T.J. Stephenson, C.K. King'Ondu, C.M. Holt, B.C. Olsen, ACS Nano 7 (2013) 5131–5141.
- [74] J. Xu, Q. Gao, Y. Zhang, Y. Tan, W. Tian, L. Zhu, L. Jiang, Sci. Rep. 4 (2014) 5545.
- [75] T. Ma, H.L. Gao, H.P. Cong, H.B. Yao, L. Wu, Z.Y. Yu, S.M. Chen, S.H. Yu, Adv. Mater. 30 (2018) 1706435.
- [76] H. Song, S. Xu, Y. Li, J. Dai, A. Gong, M. Zhu, C. Zhu, C. Chen, Y. Chen, Y. Yao, Adv. Energy Mater. 8 (2018) 1701203.
- [77] X. Zheng, J. Luo, W. Lv, D.W. Wang, Q.H. Yang, Adv. Mater. 27 (2015) 5388.
- [78] Z. Li, W. Lv, C. Zhang, B. Li, F. Kang, Q.H. Yang, Carbon 92 (2015) 11–14.
- [79] H.W. Liang, Q.F. Guan, Z. Zhu, L.T. Song, H.B. Yao, X. Lei, S.H. Yu, NPG Asia Mater. 4 (2012) e19.
- [80] B. Wang, X. Li, B. Luo, J. Yang, X. Wang, Q. Song, S. Chen, L. Zhi, Small 9 (2013) 2399.
- [81] N. Liu, L. Fu, B. Dai, K. Yan, X. Liu, R. Zhao, Y. Zhang, Z. Liu, Nano Lett. 11 (2011) 297–303.
- [82] A. Reina, X. Jia, J. Ho, D. Nezich, H. Son, V. Bulovic, M.S. Dresselhaus, J. Kong, Nano Lett. 9 (2009) 30–35.
- [83] Y.Z. Xue, B. Wu, Y.L. Gou, L.P. Huang, L. Jiang, J.Y. Chen, D.C. Geng, Y.Q. Liu, W.P. Hu, G. Yu, Nano Res. 4 (12) (2018) 1208–1214.
- [84] B. Dai, L. Fu, Z. Zou, M. Wang, H. Xu, S. Wang, Z. Liu, Nat. Commun. 2 (2011) 522.
- [85] X. Liu, L. Fu, N. Liu, T. Gao, Y. Zhang, L. Liao, Z. Liu, J. Phys. Chem. C 115 (2011) 11976–11982.
- [86] H. Wang, X. Xu, J. Li, L. Lin, L. Sun, X. Sun, S. Zhao, C. Tan, C. Chen, W. Dang, Adv. Mater. 28 (2016) 8968–8974.
- [87] R.S. Weatherup, B.C. Bayer, R. Blume, C. Ducati, C. Baehtz, R. Schlägl, S. Hofmann, Nano Lett. 11 (2011) 4154–4160.
- [88] Z. Zou, L. Fu, X. Song, Y. Zhang, Z. Liu, Nano Lett. 14 (2014) 3832.
- [89] L. Gan, Z. Luo, ACS Nano 7 (2013) 9480–9488.
- [90] D. Geng, H. Wang, G. Yu, Adv. Mater. 27 (2015) 2821.
- [91] D. Geng, B. Wu, Y. Guo, L. Huang, Y. Xue, J. Chen, G. Yu, L. Jiang, W. Hu, Y. Liu, P. Natl. Acad. Sci. USA 109 (2012) 7992–7996.
- [92] X. Li, C.W. Magnuson, A. Venugopal, R.M. Tromp, J.B. Hannon, E.M. Vogel, L. Colombo, R.S. Ruoff, J. Am. Chem. Soc. 133 (2011) 2816–2819.
- [93] X. Li, C.W. Magnuson, A. Venugopal, J. An, J.W. Suk, B. Han, M. Borysiak, W. Cai, A. Velamakanni, Y. Zhu, Nano Lett. 10 (2010) 4328–4334.
- [94] J. Wang, M. Zeng, L. Tan, B. Dai, Y. Deng, M. Rümmeli, H. Xu, Z. Li, S. Wang, L. Peng, Sci. Rep. 3 (2013) 2670.
- [95] M. Zeng, L. Tan, J. Wang, L. Chen, M.H. Rümmeli, L. Fu, Chem. Mater. 26 (2014) 3637–3643.
- [96] L. Tan, M. Zeng, T. Zhang, L. Fu, Nanoscale 7 (2015) 9105–9121.
- [97] J. Dong, Y. Xue, C. Zhang, Q. Weng, P. Dai, Y. Yang, M. Zhou, C. Li, Q. Cui, X. Kang, Adv. Mater. 29 (2017) 1603692.
- [98] Z. Chen, W. Ren, L. Gao, B. Liu, S. Pei, H.M. Cheng, Nat. Mater. 10 (2011) 424.
- [99] M.Q. Zhao, Q. Zhang, J.Q. Huang, G.L. Tian, J.Q. Nie, H.J. Peng, F. Wei, Nat. Commun. 5 (2014) 3410.
- [100] B. Wang, X. Li, X. Zhang, B. Luo, M. Jin, M. Liang, S.A. Dayeh, S.T. Picraux, L. Zhi, ACS Nano 7 (2013) 1437–1445.
- [101] H. He, D. Kong, B. Wang, W. Fu, X. Qiu, Q.-H. Yang, L. Zhi, Adv. Energy Mater. 6 (2016) 1502495.
- [102] S. Stankovich, D.A. Dikin, G.H.B. Domke, K.M. Kohlhaas, E.J. Zimney, E.A. Stach, R.D. Piner, S.T. Nguyen, R.S. Ruoff, Nature 442 (2006) 282.
- [103] Y. Hernandez, V. Nicolosi, M. Lotya, F.M. Blighe, Z. Sun, S. De, I.T. McGovern, B. Holland, M. Byrne, Y.K. Gun'Ko, Nat. Nanotech. 3 (2008) 563.
- [104] D. Li, M.B. Müller, S. Gilje, R.B. Kaner, G.G. Wallace, Nat. Nanotech. 3 (2008) 101–105.
- [105] P.W. Sutter, J.I. Flege, E.A. Sutter, Nat. Mater. 7 (2008) 406–411.
- [106] G. Williams, B. Seger, P.V. Kamat, ACS Nano 2 (2008) 1487.
- [107] C. Berger, Science 312 (2006) 1191–1196.
- [108] X. Li, W. Cai, J. An, S. Kim, J. Nah, D. Yang, R. Piner, A. Velamakanni, I. Jung, E. Tutuc, S.K. Banerjee, L. Colombo, R.S. Ruoff, Science 324 (2009) 1312–1314.
- [109] M. Lotya, Y. Hernandez, P.J. King, R.J. Smith, V. Nicolosi, L.S. Karlsson, F.M. Blighe, S. De, Z. Wang, I.T. McGovern, J. Am. Chem. Soc. 131 (2009) 3611–3620.
- [110] S. Park, R.S. Ruoff, Nat. Nanotech. 4 (2009) 217.
- [111] S. Bae, H. Kim, Y. Lee, X. Xu, J.S. Park, Y. Zheng, J. Balakrishnan, T. Lei, H.R. Kim, Y.I. Song, Nat. Nanotech. 5 (2010) 574–578.
- [112] Z. Sun, Z. Yan, J. Yao, E. Beiter, Y. Zhu, J.M. Tour, Nature 468 (2010) 549–552.
- [113] Y. Zhu, M.D. Stoller, W. Cai, A. Velamakanni, R.D. Piner, D. Chen, R.S. Ruoff, ACS Nano 4 (2010) 1227–1233.
- [114] X.T. Zheng, A. Ananthanarayanan, K.Q. Luo, P. Chen, Small 11 (2015) 1620–1636.
- [115] N. Brun, K. Sakaushi, J. Eckert, M.M. Titirici, ACS Sustain. Chem. Eng. 2 (2014) 126–129.
- [116] W.S.H. Jr, R.E. Offeman, J. Am. Chem. Soc. 80 (1958) 1339.
- [117] W. Cai, R.D. Piner, F.J. Stadermann, S. Park, M.A. Shaibat, Y. Ishii, D. Yang, A. Velamakanni, S.J. An, M. Stoller, Science 321 (2008) 1815–1817.
- [118] W. Gao, L.B. Alemany, L. Ci, P.M. Ajayan, Nat. Chem. 1 (2009) 403–408.
- [119] L.B. Casabianca, M.A. Shaibat, W.W. Cai, S. Park, R. Piner, R.S. Ruoff, Y. Ishii, J. Am. Chem. Soc. 132 (2010) 5672–5676.
- [120] S. Eigler, C. Dotzer, F. Hof, W. Bauer, A. Hirsch, Chem-Eur. J 19 (2013) 9490–9496.
- [121] D.C. Marcano, D.V. Kosynkin, J.M. Berlin, A. Sinitskii, Z. Sun, A. Slesarev, L.B. Alemany, W. Lu, J.M. Tour, ACS Nano 4 (2010) 4806.
- [122] A. Dimiev, D.V. Kosynkin, L.B. Alemany, P. Chaguine, J.M. Tour, J. Am. Chem. Soc. 134 (2012) 2815–2822.
- [123] S. Eigler, M. Enzelberger-Heim, S. Grimm, P. Hofmann, W. Kroener, A. Geworski, C. Dotzer, M. Röckert, J. Xiao, C. Papp, Adv. Mater. 25 (2013) 3583–3587.
- [124] L. Zhang, X. Li, Y. Huang, Y. Ma, X. Wan, Y. Chen, Carbon 48 (2010) 2367–2371.
- [125] B. Liu, J. Xie, H. Ma, X. Zhang, Y. Pan, J. Lv, H. Ge, N. Ren, H. Su, X. Xie, Small 13 (2017) 1601001.
- [126] A.M. Abdelkader, I.A. Kinloch, R.A. Dryfe, Chem. Commun. (Camb.) 50 (2014) 8402–8404.
- [127] B. Gurzeda, P. Florczak, M. Kempinski, B. Peplińska, P. Krawczyk, S. Jurga, Carbon 100 (2016) 540–545.
- [128] P. Yu, Z. Tian, S.E. Lowe, J. Song, Z. Ma, X. Wang, Z.J. Han, Q. Bao, G.P. Simon, D. Li, Chem. Mater. 28 (2016) 8429–8438.
- [129] Z. Tian, P. Yu, S.E. Lowe, A.G. Pandolfo, T.R. Gengenbach, K.M. Baird, J. Song, X. Wang, Y.L. Zhong, D. Li, Carbon 112 (2017) 185–191.
- [130] K. Parvez, R. Li, S.R. Puniredd, Y. Hernandez, F. Hinkel, S. Wang, X. Feng, K. Müllen, ACS Nano 7 (2013) 3598–3606.
- [131] A. Ejigu, I.A. Kinloch, R.A.W. Dryfe, ACS Appl. Mater. Interfaces 9 (2017) 710–721.
- [132] J. Cao, P. He, M.A. Mohammed, X. Zhao, R.J. Young, B. Derby, I.A. Kinloch, R.A.W. Dryfe, J. Am. Chem. Soc. 139 (2017) 17446–17456.
- [133] S. Pei, Q. Wei, K. Huang, H.M. Cheng, W. Ren, Nat. Commun. 9 (2018) 145.
- [134] A.L. Higginbotham, D.V. Kosynkin, A. Sinitskii, Z. Sun, J.M. Tour, ACS Nano 4 (2010) 2059–2069.
- [135] L. Jiao, L. Zhang, X. Wang, G. Diankov, H. Dai, Nature 458 (2009) 877.
- [136] L. Jiao, X. Wang, G. Diankov, H. Wang, H. Dai, Nat. Nanotech. 5 (2010) 321–325.
- [137] M. Liang, J. Wang, B. Luo, T. Qiu, L. Zhi, Small 8 (2012) 1180–1184.
- [138] J. Ning, L. Hao, M. Jin, X. Qiu, Y. Shen, J. Liang, X. Zhang, B. Wang, X. Li, L. Zhi, Adv. Mater. 29 (2017) 1605028.
- [139] W. Ai, W. Zhou, Z. Du, C. Sun, J. Yang, Y. Chen, Z. Sun, S. Feng, J. Zhao, X. Dong, Adv. Funct. Mater. 27 (2017) 1603603.
- [140] J. Xu, Y. Lin, J.W. Connell, L. Dai, Small 11 (2015) 6179–6185.
- [141] J. Dong, Y. Xue, C. Zhang, Q. Weng, P. Dai, Y. Yang, M. Zhou, C. Li, Q. Cui, X. Kang, C. Tang, Y. Bando, D. Golberg, X. Wang, Adv. Mater. 29 (2016), <https://doi.org/10.1002/adma.201603692>.
- [142] Z. Xie, Z. He, X. Feng, W. Xu, X. Cui, J. Zhang, C. Yan, M.A. Carreon, Z. Liu, Y. Wang, ACS Appl. Mater. Interfaces 8 (2016) 10324–10333.

- [143] M. Zhou, X. Li, B. Wang, Y. Zhang, J. Ning, Z. Xiao, X. Zhang, Y. Chang, L. Zhi, *Nano Lett.* 15 (2015) 6222–6228.
- [144] X. Zhang, R. Guo, X. Li, L. Zhi, *Small* 14 (2018) 1703569.
- [145] H. Sun, L. Mei, J. Liang, Z. Zhao, C. Lee, H. Fei, M. Ding, J. Lau, M. Li, C. Wang, X. Xu, G. Hao, B. Papandrea, I. Shakir, B. Dunn, Y. Huang, X. Duan, *Science* 356 (2017) 599–604.
- [146] F.M. Hassan, R. Batmaz, J. Li, X. Wang, X. Xiao, A. Yu, Z. Chen, *Nat. Commun.* 6 (2015) 8597.
- [147] B. Wang, X. Li, X. Zhang, B. Luo, Y. Zhang, L. Zhi, *Adv. Mater.* 25 (2013) 3560–3565.
- [148] J. Muldoon, C.B. Bucur, A.G. Oliver, T. Sugimoto, M. Matsui, H.S. Kim, G.D. Allred, J. Zajicek, Y. Kotani, *Energy Environ. Sci.* 5 (2012) 5941–5950.
- [149] P. Wu, H. Wang, Y. Tang, Y. Zhou, T. Lu, *ACS Appl. Mater. Interfaces* 6 (2014) 3546–3552.
- [150] X. Ma, M. Liu, L. Gan, P.K. Tripathi, Y. Zhao, D. Zhu, Z. Xu, L. Chen, *Phys. Chem. Chem. Phys.* 16 (2014) 4135–4142.
- [151] J. Liu, P. Kopolid, P.A. van Aken, J. Maier, Y. Yu, *Angew. Chem. Int. Ed.* 54 (2015) 9632–9636.
- [152] B. Luo, B. Wang, M. Liang, J. Ning, X. Li, L. Zhi, *Adv. Mater.* 24 (2012) 1405–1409.
- [153] B. Luo, B. Wang, X. Li, Y. Jia, M. Liang, L. Zhi, *Adv. Mater.* 24 (2012) 3538–3543.
- [154] D. Kong, H. He, Q. Song, B. Wang, W. Lv, Q.-H. Yang, L. Zhi, *Energy Environ. Sci.* 7 (2014) 3320–3325.
- [155] S.S. Han, J.L. Mendoza-Cortá, *Chem. Soc. Rev.* 38 (2009) 1460–1476.
- [156] L.-F. Chen, Y. Lu, L. Yu, X.W.D. Lou, *Energy Environ. Sci.* 10 (2017) 1777–1783.
- [157] L. Yao, Q. Wu, P. Zhang, J. Zhang, D. Wang, Y. Li, X. Ren, H. Mi, L. Deng, Z. Zheng, *Adv. Mater.* 30 (2018) 1706054.
- [158] Y. Zhai, Y. Dou, D. Zhao, P.F. Fulvio, R.T. Mayes, S. Dai, *Adv. Mater.* 23 (2011) 4828–4850.
- [159] Y. Sun, Q. Wu, G. Shi, *Energy Environ. Sci.* 4 (2011) 1113–1132.
- [160] X. Huang, Z. Zeng, Z. Fan, J. Liu, H. Zhang, *Adv. Mater.* 24 (2012) 5979–6004.
- [161] L. Sheng, L. Jiang, T. Wei, Z. Liu, Z. Fan, *Adv. Energy Mater.* 7 (2017) 1700668.
- [162] C. Largeot, C. Portet, J. Chmiola, P.L. Taberna, Y. Gogotsi, P. Simon, *J. Am. Chem. Soc.* 130 (2015) 2730–2731.
- [163] D. Yuan, W. Lu, D. Zhao, H.C. Zhou, *Adv. Mater.* 23 (2011) 3723–3725.
- [164] D. Kong, X. Qiu, B. Wang, Z. Xiao, X. Zhang, R. Guo, Y. Gao, Q.-H. Yang, L. Zhi, *Sci. China Mater.* 61 (2018) 671–678.
- [165] D. Kong, X. Li, Y. Zhang, X. Hai, B. Wang, X. Qiu, Q. Song, Q.-H. Yang, L. Zhi, *Angew. Chem. Int. Ed.* 9 (2016) 906–911.
- [166] L.F. Chen, Z.H. Huang, H.W. Liang, H.L. Gao, S.H. Yu, *Adv. Funct. Mater.* 24 (2015) 5104–5111.
- [167] E. Raymundo-Piñero, F. Leroux, F. Béguin, *Adv. Mater.* 18 (2006) 1877–1882.
- [168] Z. Fan, J. Yan, L. Zhi, Q. Zhang, T. Wei, J. Feng, M. Zhang, W. Qian, F. Wei, *Adv. Mater.* 22 (2010) 3723–3728.
- [169] D. Hulicova-Jurcakova, M. Kodama, S. Shiraishi, H. Hatori, Z.H. Zhi, G.Q. Lu, *Adv. Funct. Mater.* 19 (2010) 1800–1809.
- [170] D. Hulicova-Jurcakova, M. Seredych, Q.L. Gao, T.J. Bandosz, *Adv. Funct. Mater.* 19 (2010) 438–447.
- [171] G. Lota, K. Fic, E. Frackowiak, *Energy Environ. Sci.* 4 (2011) 1592–1605.
- [172] J. Yang, H. Wu, M. Zhu, W. Ren, Y. Lin, H. Chen, F. Pan, *Nano Energy* 33 (2017) 453–461.
- [173] W. Yang, F. Ding, G. Shao, L. Sang, W. Yang, Z. Ma, *Carbon* 111 (2017) 419–427.
- [174] J. Yan, Z. Fan, S. Wei, G. Ning, W. Tong, Z. Qiang, R. Zhang, L. Zhi, W. Fei, *Adv. Funct. Mater.* 22 (2012) 2632–2641.
- [175] V. Augustyn, P. Simon, B. Dunn, *Energy Environ. Sci.* 7 (2014) 1597–1614.
- [176] V. Presser, M. Heon, Y. Gogotsi, *Adv. Funct. Mater.* 21 (2015) 810–833.
- [177] S. Wang, Z.S. Wu, S. Zheng, F. Zhou, C. Sun, H.M. Cheng, X. Bao, *ACS Nano* 11 (2017) 4283.
- [178] S. Wang, Z.S. Wu, F. Zhou, X. Shi, S. Zheng, J. Qin, H. Xiao, C. Sun, X. Bao, *npj 2D Mater. Appl.* 2 (2018) 7.
- [179] F. Su, C.K. Poh, J.S. Chen, G. Xu, D. Wang, Q. Li, J. Lin, X.W. Lou, *Energy Environ. Sci.* 4 (2011) 717–724.
- [180] G. Lota, K. Lota, E. Frackowiak, *Electrochem. commun.* 9 (2007) 1828–1832.
- [181] Y. Fang, B. Luo, Y. Jia, X. Li, B. Wang, Q. Song, F. Kang, L. Zhi, *Adv. Mater.* 24 (2012) 6348–6355.
- [182] D. Hulicova-Jurcakova, A.M. Puziy, O.I. Poddubnaya, F. Suárez-García, J.M. Tascón, G.Q. Lu, *J. Am. Chem. Soc.* 131 (2009) 5026–5027.
- [183] J. Han, L.L. Zhang, S. Lee, J. Oh, K.-S. Lee, J.R. Potts, J. Ji, X. Zhao, R.S. Ruoff, S. Park, *ACS Nano* 7 (2012) 19–26.
- [184] D.-W. Wang, F. Li, Z.-G. Chen, G.Q. Lu, H.-M. Cheng, *Chem. Mater.* 20 (2008) 7195–7200.
- [185] X. Zhai, Y. Song, J. Liu, P. Li, M. Zhong, C. Ma, H. Wang, Q. Guo, L. Zhi, *J. Electrochem. Soc.* 159 (2012) 177–182.
- [186] D.W. Wang, F. Li, L.C. Yin, X. Lu, Z.G. Chen, I.R. Gentle, G.Q. Lu, H.M. Cheng, *Chem-Eur. J* 18 (2012) 5345–5351.
- [187] L. Hao, B. Luo, X. Li, M. Jin, Y. Fang, Z. Tang, Y. Jia, M. Liang, A. Thomas, J. Yang, L. Zhi, *Energy Environ. Sci.* 5 (2012) 9747.
- [188] L. Hao, X. Li, L. Zhi, *Adv. Mater.* 25 (2013) 3899–3904.
- [189] P. Kuhn, M. Antonietti, A. Thamos, *Angew. Chem., Int. Ed.* 47 (2008) 3450–3453.
- [190] A. Thomas, *Angew. Chem. Int. Ed.* 49 (2010) 8328.
- [191] A.I. Cooper, *Adv. Mater.* 21 (2009) 1291.
- [192] H. He, L. Shi, Y. Fang, X. Li, Q. Song, L. Zhi, *Small* 10 (2014) 4671.
- [193] L. Shi, X. Li, Y. Jia, D. Kong, H. He, M. Wagner, K. Müllen, L. Zhi, *Energy Storage Mater.* 5 (2016) 43–49.
- [194] Y. Tao, X. Xie, W. Lv, D.M. Tang, D. Kong, Z. Huang, H. Nishihara, T. Ishii, B. Li, D. Golberg, *Sci. Rep.* 3 (2013) 2975.
- [195] Y. Xu, Y. Tao, H. Li, C. Zhang, D. Liu, C. Qi, J. Luo, F. Kang, Q.-H. Yang, *Nano Energy* 36 (2017) 349–355.
- [196] Y. Xu, Y. Tao, X. Zheng, H. Ma, J. Luo, F. Kang, Q.H. Yang, *Adv. Mater.* 27 (2015) 7898.
- [197] H. Ma, D. Kong, Y. Xu, X. Xie, Y. Tao, Z. Xiao, W. Lv, H.D. Jang, J. Huang, Q.H. Yang, *Small* 13 (2017) 1701026.
- [198] H. Li, Y. Tao, X. Zheng, J. Luo, F. Kang, H.M. Cheng, Q.H. Yang, *Energy Environ. Sci.* 9 (2016) 3135–3142.
- [199] J.H. Sung, S.J. Kim, S.H. Jeong, E.H. Kim, K.H. Lee, *J. Power Sources* 162 (2006) 1467–1470.
- [200] S.K. Cheah, E. Perre, M. Rooth, M. Fondell, A. Harsta, L. Nyholm, M. Boman, T. Gustafsson, J. Lu, P. Simon, *Nano Lett.* 9 (2009) 3230–3233.
- [201] M. Beidaghi, Y. Gogotsi, *Energy Environ. Sci.* 7 (2014) 867–884.
- [202] K. Jost, G. Dion, Y. Gogotsi, J. Mater. Chem. A Mater. Energy Sustain. 2 (2014) 10776–10787.
- [203] J. Chmiola, C. Largeot, P.L. Taberna, P. Simon, Y. Gogotsi, *Science* 328 (2010) 480–483.
- [204] W. Si, C. Yan, Y. Chen, S. Oswald, L. Han, O.G. Schmidt, *Energy Environ. Sci.* 6 (2013) 3218–3223.
- [205] J. Lin, Z. Peng, Y. Liu, F. Ruiz-Zepeda, R. Ye, E.L. Samuel, M.J. Yacaman, B.I. Yakobson, J.M. Tour, *Nat. Commun.* 5 (2014) 5714.
- [206] Z.S. Wu, K. Parvez, A. Winter, H. Vieker, X. Liu, S. Han, A. Turchanin, X. Feng, K. Müllen, *Adv. Mater.* 26 (2014) 4552–4558.
- [207] Y.G. Zhu, Y. Wang, Y. Shi, J.I. Wong, H.Y. Yang, *Nano Energy* 3 (2014) 46–54.
- [208] Z.S. Wu, Y.Z. Tan, S. Zheng, S. Wang, K. Parvez, J. Qin, X. Shi, C. Sun, X. Bao, X. Feng, *J. Am. Chem. Soc.* 139 (2017) 4506–4512.
- [209] J. Lin, C. Zhang, Z. Yan, Y. Zhu, Z. Peng, R.H. Hauge, D. Natelson, J.M. Tour, *Nano Lett.* 13 (2013) 72–78.
- [210] K.S. Min, B. Lee, H.K. Shi, J.A. Lee, G.M. Spinks, S. Gambhir, G.G. Wallace, M.E. Kozlov, R.H. Baughman, S.J. Kim, *Nat. Commun.* 3 (2012) 650.
- [211] X. Li, L. Zhi, *Chem. Soc. Rev.* 47 (2018) 3189–3216.
- [212] P. Kulkarni, S.K. Nataraj, R.G. Balakrishna, D.H. Nagaraju, M.V. Reddy, J. Mater. Chem. A Mater. Energy Sustain. 5 (2017) 22040–22094.
- [213] H. Wang, H.S. Casalongue, Y. Liang, H. Dai, *J. Am. Chem. Soc.* 132 (2010) 7472–7477.
- [214] Y. Chen, W.K. Pang, H. Bai, T. Zhou, Y. Liu, S. Li, Z. Guo, *Nano Lett.* 17 (2016) 429–436.
- [215] G. Yu, L. Hu, M. Vosgueritchian, H. Wang, X. Xie, J.R. McDonough, X. Cui, Y. Cui, Z. Bao, *Nano Lett.* 11 (2011) 2905–2911.
- [216] X. Cao, Y. Shi, W. Shi, G. Lu, X. Huang, Q. Yan, Q. Zhang, H. Zhang, *Small* 7 (2011) 3163–3168.
- [217] Q. Wu, Y. Xu, Z. Yao, A. Liu, G. Shi, *ACS Nano* 4 (2010) 1963–1970.
- [218] J. Yan, C.E. Ren, K. Maleski, C.B. Hatter, B. Anasori, P. Urbankowski, A. Sarycheva, Y. Gogotsi, *Adv. Funct. Mater.* 27 (2017) 1701264.
- [219] L. Wang, D. Wang, F. Zhang, J. Jin, *Nano Lett.* 13 (2013) 4206–4211.
- [220] Z.S. Wu, W. Ren, D.W. Wang, F. Li, B. Liu, H.M. Cheng, *ACS Nano* 4 (2010) 5835–5842.
- [221] X. Zhao, L. Zhang, S. Murali, M.D. Stoller, Q. Zhang, Y. Zhu, R.S. Ruoff, *ACS Nano* 6 (2012) 5404–5412.
- [222] Z. Fan, J. Yan, T. Wei, L. Zhi, G. Ning, T. Li, F. Wei, *Adv. Funct. Mater.* 21 (2011) 2366–2375.
- [223] E. Lim, C. Jo, M.S. Kim, M.H. Kim, J. Chun, H. Kim, J. Park, K.C. Roh, K. Kang, S. Yoon, *Adv. Funct. Mater.* 26 (2016) 3711–3719.
- [224] Z.H. Wu, D.E. Wang, W. Ren, J. Zhao, G. Zhou, F. Li, H.I. Cheng, *Adv. Funct. Mater.* 20 (2010) 3595–3602.
- [225] G. Xiong, P. He, D. Wang, Q. Zhang, T. Chen, T.S. Fisher, *Adv. Funct. Mater.* 26 (2016) 5460–5470.
- [226] H. Xia, C. Hong, B. Li, B. Zhao, Z. Lin, M. Zheng, S.V. Savilov, S.M. Aldoshin, *Adv. Funct. Mater.* 25 (2015) 627–635.
- [227] X. Cao, B. Zheng, W. Shi, J. Yang, Z. Fan, Z. Luo, X. Rui, B. Chen, Q. Yan, H. Zhang, *Adv. Mater.* 27 (2015) 4695–4701.
- [228] J. Zheng, M. Gu, H. Chen, P. Meduri, M.H. Engelhard, J.-G. Zhang, J. Liu, J. Xiao, J. Mater. Chem. A Mater. Energy Sustain. 1 (2013) 8464–8470.
- [229] Q. Qu, S. Yang, X. Feng, *Adv. Mater.* 23 (2011) 5574–5580.
- [230] C. Xu, Z. Li, C. Yang, P. Zou, B. Xie, Z. Lin, Z. Zhang, B. Li, F. Kang, C.P. Wong, *Adv. Mater.* 28 (2016) 4105–4110.
- [231] J. Yang, C. Yu, X. Fan, S. Liang, S. Li, H. Huang, Z. Ling, C. Hao, J. Qiu, *Energy Environ. Sci.* 9 (2016) 1299–1307.
- [232] J. Zhang, Z. Xia, L. Dai, *Sci. Adv.* 1 (2015) e1500564–e1500583.
- [233] L. Dai, Y. Xue, L. Qu, H.J. Choi, J.B. Baek, *Chem. Rev.* 115 (2015) 4823–4892.
- [234] B. Kumar, M. Asadi, D. Pisasale, S. Sinha-Ray, B.A. Rosen, R. Haasch, J. Abiade, A.L. Yarin, A. Salehi-Khojin, *Nat. Commun.* 4 (2013) 2819.
- [235] J. Wu, S. Ma, J. Sun, J.I. Gold, C. Tiwary, B. Kim, L. Zhu, N. Chopra, I.N. Odeh, R. Vajtai, A.Z. Yu, R. Luo, J. Lou, G. Ding, P.J. Kenis, P.M. Ajayan, *Nat. Commun.* 7 (2016) 13869.
- [236] S. Guo, S. Zhang, S. Sun, *Angew. Chem. Int. Ed.* 52 (2013) 8526–8544.
- [237] D.-W. Wang, D. Su, *Energy Environ. Sci.* 7 (2014) 576–591.
- [238] L. Yang, X. Zeng, W. Wang, D. Cao, *Adv. Funct. Mater.* (2017) 1704537.
- [239] K. Gong, F. Du, Z. Xia, M. Durstock, L. Dai, *Science* 323 (2009) 760–764.
- [240] L. Yang, S. Jiang, Y. Zhao, L. Zhu, S. Chen, X. Wang, Q. Wu, J. Ma, Y. Ma, Z. Hu, *Angew. Chem. Int. Ed.* 50 (2011) 7132–7135.
- [241] L. Qu, Y. Liu, J.-B. Baek, L. Dai, *ACS Nano* 4 (2010) 1321–1326.
- [242] I.Y. Jeon, H.J. Choi, S.M. Jung, J.M. Seo, M.J. Kim, L. Dai, J.B. Baek, *J. Am. Chem. Soc.* 135 (2013) 1386–1393.
- [243] I.Y. Jeon, S. Zhang, L. Zhang, H.J. Choi, J.M. Seo, Z. Xia, L. Dai, J.B. Baek, *Adv. Mater.* 25 (2013) 6138–6145.
- [244] S. Yang, L. Zhi, K. Tang, X. Feng, J. Maier, K. Müllen, *Adv. Funct. Mater.* 22 (2012) 1–37.

- 3634–3640.
- [245] W. Ding, Z. Wei, S. Chen, X. Qi, T. Yang, J. Hu, D. Wang, L.J. Wan, S.F. Alvi, L. Li, *Angew. Chem. Int. Ed.* 52 (2013) 11755–11759.
- [246] S. Wang, E. Iyyamperumal, A. Roy, Y. Xue, D. Yu, L. Dai, *Angew. Chem. Int. Ed.* 50 (2011) 11756–11760.
- [247] Y. Zhao, L. Yang, S. Chen, X. Wang, Y. Ma, Q. Wu, Y. Jiang, W. Qian, Z. Hu, *J. Am. Chem. Soc.* 135 (2013) 1201–1204.
- [248] S. Wang, L. Zhang, Z. Xia, A. Roy, D.W. Chang, J.B. Baek, L. Dai, *Angew. Chem. Int. Ed.* 51 (2012) 4209–4212.
- [249] Y. Zheng, Y. Jiao, L. Ge, M. Jaroniec, S.Z. Qiao, *Angew. Chem. Int. Ed.* 52 (2013) 3110–3116.
- [250] D. Yu, Y. Xue, L. Dai, *J. Phys. Chem. Lett.* 3 (2012) 2863–2870.
- [251] J. Liang, Y. Jiao, M. Jaroniec, S.Z. Qiao, *Angew. Chem. Int. Ed.* 51 (2012) 11496–11500.
- [252] R. Liu, D. Wu, X. Feng, K. Müllen, *Angew. Chem. Int. Ed.* 49 (2010) 2565–2569.
- [253] Z.W. Liu, F. Peng, H.J. Wang, H. Yu, W.X. Zheng, J. Yang, *Angew. Chem. Int. Ed.* 50 (2011) 3257–3261.
- [254] H.W. Liang, X. Zhuang, S. Bruller, X. Feng, K. Müllen, *Nat. Commun.* 5 (2014) 4973.
- [255] W. Yang, T.-P. Fellinger, M. Antonietti, *J. Am. Chem. Soc.* 133 (2011) 206–209.
- [256] K. Sakaushi, M. Antonietti, *Acc. Chem. Res.* 48 (2015) 1591–1600.
- [257] N. Huang, P. Wang, D. Jiang, *Nat. Rev. Mater.* 1 (2016) 16068.
- [258] C.S. Diercks, O.M. Yaghi, *Science* 355 (2017) eaal1585.
- [259] Z. Xiang, D. Cao, L. Huang, J. Shui, M. Wang, L. Dai, *Adv. Mater.* 26 (2014) 3315–3320.
- [260] L. Hao, S. Zhang, R. Liu, J. Ning, G. Zhang, L. Zhi, *Adv. Mater.* 27 (2015) 3190–3195.
- [261] Q. Xu, Y. Tang, X. Zhang, Y. Oshima, Q. Chen, D. Jiang, *Adv. Mater.* 30 (2018) 1706330.
- [262] Y. Xu, M. Kraft, R. Xu, *Chem. Soc. Rev.* 45 (2016) 3039–3052.
- [263] Y. Zhao, R. Nakamura, K. Kamiya, S. Nakanishi, K. Hashimoto, *Nat. Commun.* 4 (2013) 2390.
- [264] X. Lu, W.L. Yim, B.H. Suryanto, C. Zhao, *J. Am. Chem. Soc.* 137 (2015) 2901–2907.
- [265] Z. Xiao, X. Huang, L. Xu, D. Yan, J. Huo, S. Wang, *Chem. Commun. (Camb.)* 52 (2016) 13008–13011.
- [266] S. Chen, J. Duan, M. Jaroniec, S.Z. Qiao, *Adv. Mater.* 26 (2014) 2925–2930.
- [267] Y. Zheng, Y. Jiao, Y. Zhu, L.H. Li, Y. Han, Y. Chen, A. Du, M. Jaroniec, S.Z. Qiao, *Nat. Commun.* 5 (2014) 3783.
- [268] Y. Zheng, Y. Jiao, L.H. Li, T. Xing, Y. Chen, M. Jaroniec, S.Z. Qiao, *ACS Nano* 8 (2014) 5290–5296.
- [269] D. Yan, S. Dou, L. Tao, Z. Liu, Z. Liu, J. Huo, S. Wang, *J. Mater. Chem. A Mater. Energy Sustain.* 4 (2016) 13726–13730.
- [270] K. Qu, Y. Zheng, X. Zhang, K. Davey, S. Dai, S.Z. Qiao, *ACS Nano* 11 (2017) 7293–7300.
- [271] S.N. Talapaneni, J. Kim, S.-H. Je, O. Buyukcakir, J. Oh, A. Coskun, *J. Mater. Chem. A Mater. Energy Sustain.* 5 (2017) 12080–12085.
- [272] J. Zhang, Z. Zhao, Z. Xia, L. Dai, *Nat. Nanotech.* 10 (2015) 444–452.
- [273] J.-C. Li, P.-X. Hou, S.-Y. Zhao, C. Liu, D.-M. Tang, M. Cheng, F. Zhang, H.-M. Cheng, *Energy Environ. Sci.* 9 (2016) 3079–3084.
- [274] G.L. Tian, M.Q. Zhao, D. Yu, X.Y. Kong, J.Q. Huang, Q. Zhang, F. Wei, *Small* 10 (2014) 2251–2259.
- [275] G.-L. Chai, K. Qiu, M. Qiao, M.-M. Titirici, C. Shang, Z. Guo, *Energy Environ. Sci.* 10 (2017) 1186–1195.
- [276] G.-L. Tian, Q. Zhang, B. Zhang, Y.-G. Jin, J.-Q. Huang, D.S. Su, F. Wei, *Adv. Funct. Mater.* 24 (2014) 5956–5961.
- [277] R. Li, Z. Wei, X. Gou, *ACS Catal.* 5 (2015) 4133–4142.
- [278] Z. Liu, Z. Zhao, Y. Wang, S. Dou, D. Yan, D. Liu, Z. Xia, S. Wang, *Adv. Mater.* 29 (2017) 1606207.
- [279] J. Zhang, L. Qu, G. Shi, J. Liu, J. Chen, L. Dai, *Angew. Chem. Int. Ed.* 55 (2016) 2230–2234.
- [280] J. Zhang, L. Dai, *Angew. Chem. Int. Ed.* 55 (2016) 13296–13300.
- [281] J. Wu, R.M. Yadav, M. Liu, P.P. Sharma, C.S. Tiwary, L. Ma, X. Zou, X.-D. Zhou, B.I. Yakobson, J. Lou, P.M. Ajayan, *ACS Nano* 9 (2015) 5364–5371.
- [282] X. Cui, Z. Pan, L. Zhang, H. Peng, G. Zheng, *Adv. Energy Mater.* (2017) 1701456.
- [283] J. Wu, M. Liu, P.P. Sharma, R.M. Yadav, L. Ma, Y. Yang, X. Zou, X.-D. Zhou, R. Vajtai, B.I. Yakobson, J. Lou, P.M. Ajayan, *Nano Lett.* 16 (2016) 466–470.
- [284] S. Sharma, B.G. Pollet, *J. Power Sources* 208 (2012) 96–119.
- [285] Y.-J. Wang, B. Fang, H. Li, X.T. Bi, H. Wang, *Prog. Mater. Sci.* 82 (2016) 445–498.
- [286] C.-L. Sun, L.-C. Chen, M.-C. Su, L.-S. Hong, O. Chyan, C.-Y. Hsu, K.-H. Chen, T.-F. Chang, L. Chang, *Chem. Mater.* 17 (2005) 3749–3753.
- [287] D. He, Y. Jiang, H. Lv, M. Pan, S. Mu, *Appl. Catal. B* 132–133 (2013) 379–388.
- [288] Y. Liang, Y. Li, H. Wang, J. Zhou, J. Wang, T. Regier, H. Dai, *Nat. Mater.* 10 (2011) 780–786.
- [289] Y. Liang, H. Wang, P. Diao, W. Chang, G. Hong, Y. Li, M. Gong, L. Xie, J. Zhou, J. Wang, *J. Am. Chem. Soc.* 134 (2012) 15849–15857.
- [290] Z.S. Wu, S. Yang, Y. Sun, K. Parvez, X. Feng, K. Müllen, *J. Am. Chem. Soc.* 134 (2012) 9082–9085.
- [291] E. Hu, X.-Y. Yu, F. Chen, Y. Wu, Y. Hu, X.W.D. Lou, *Adv. Energy Mater.* (2017) 1702476.
- [292] Y. Niu, X. Huang, L. Zhao, W. Hu, C.M. Li, *ACS Sustain. Chem. Eng.* 6 (2018) 3556–3564.
- [293] G. Wu, K.L. More, C.M. Johnston, P. Zelenay, *Science* 332 (2011) 443–447.
- [294] H.-W. Liang, W. Wei, Z.-S. Wu, X. Feng, K. Müllen, *J. Am. Chem. Soc.* 135 (2013) 16002–16005.
- [295] Q. Lin, X. Bu, A. Kong, C. Mao, F. Bu, P. Feng, *Adv. Mater.* 27 (2015) 3431–3436.
- [296] Y.Z. Chen, C. Wang, Z.Y. Wu, Y. Xiong, Q. Xu, S.H. Yu, H.L. Jiang, *Adv. Mater.* 27 (2015) 5010–5016.
- [297] P. Yin, T. Yao, Y. Wu, L. Zheng, Y. Lin, W. Liu, H. Ju, J. Zhu, X. Hong, Z. Deng, G. Zhou, S. Wei, Y. Li, *Angew. Chem. Int. Ed.* 55 (2016) 10800–10805.
- [298] Y. Chen, S. Ji, Y. Wang, J. Dong, W. Chen, Z. Li, R. Shen, L. Zheng, Z. Zhuang, D. Wang, Y. Li, *Angew. Chem. Int. Ed.* 56 (2017) 6937–6941.
- [299] J. Wang, Z. Huang, W. Liu, C. Chang, H. Tang, Z. Li, W. Chen, C. Jia, T. Yao, S. Wei, Y. Wu, Y. Li, *J. Am. Chem. Soc.* 139 (2017) 17281–17284.
- [300] L.J. Brennan, M.T. Byrne, M. Bari, Y.K. Gun'ko, *Adv. Energy Mater.* 1 (2011) 472–485.
- [301] Z. Yin, J. Zhu, Q. He, X. Cao, C. Tan, H. Chen, Q. Yan, H. Zhang, *Adv. Energy Mater.* 4 (2013) 1300547.
- [302] H.J. Yen, H. Tsai, M. Zhou, E.F. Holby, S. Choudhury, A. Chen, L. Adamska, S. Tretiak, T. Sanchez, S. Iyer, H. Zhang, L. Zhu, H. Lin, L. Dai, G. Wu, H.L. Wang, *Adv. Mater.* 28 (2016) 10250–10256.
- [303] J.D. Roy-Mayhew, D.J. Bozym, C. Puncpt, I.A. Aksay, *ACS Nano* 4 (2010) 6203–6211.
- [304] M.J. Ju, I.-Y. Jeon, K. Lim, J.C. Kim, H.-J. Choi, I.T. Choi, Y.K. Eom, Y.J. Kwon, J. Ko, J.-J. Lee, J.-B. Baek, H.K. Kim, *Energy Environ. Sci.* 7 (2014) 1044–1052.
- [305] M.J. Ju, I.-Y. Jeon, H.M. Kim, J.I. Choi, S.-M. Jung, J.-M. Seo, I.T. Choi, S.H. Kang, H.S. Kim, M.J. Noh, J.-J. Lee, H.Y. Jeong, H.K. Kim, Y.-H. Kim, J.-B. Baek, *Sci. Adv.* 2 (2016) e1501459–e1501467.
- [306] S. Hou, X. Cai, H. Wu, X. Yu, M. Peng, K. Yan, D. Zou, *Energy Environ. Sci.* 6 (2013) 3356–3362.
- [307] M.J. Ju, J.C. Kim, H.-J. Choi, I.T. Choi, S.G. Kim, K. Lim, J. Ko, J.-J. Lee, I.-Y. Jeon, J.-B. Baek, H.K. Kim, *ACS Nano* 7 (2013) 5243–5250.
- [308] Y. Xue, J. Liu, H. Chen, R. Wang, D. Li, J. Qu, L. Dai, *Angew. Chem. Int. Ed.* 51 (2012) 12124–12127.
- [309] X. Meng, C. Yu, X. Song, Y. Liu, S. Liang, Z. Liu, C. Hao, J. Qiu, *Adv. Energy Mater.* 5 (2015) 1500180.
- [310] Y. Xue, J.M. Baek, H. Chen, J. Qu, L. Dai, *Nanoscale* 7 (2015) 7078–7083.
- [311] K.S. Lee, W.J. Lee, N.G. Park, S.O. Kim, J.H. Park, *Chem. Commun. (Camb.)* 47 (2011) 4264–4266.
- [312] B.B. Parekh, G. Fanchini, G. Eda, M. Chhowalla, *Appl. Phys. Lett.* 90 (2007) 121913.
- [313] X. Wang, L. Zhi, K. Müllen, *Nano Lett.* 8 (2008) 323–327.
- [314] Z. Yin, S. Sun, T. Salim, S. Wu, X. Huang, Q. He, Y.M. Lam, H. Zhang, *ACS Nano* 4 (2010) 5263–5268.